UNIVERSITY OF OKLAHOMA

GRADUATE COLLEGE

Quantum Effects in Nodal-line Semimetals

A DISSERTATION

SUBMITTED TO THE GRADUATE FACULTY

in partial fulfillment of the requirements for the

Degree of

Doctor of Philosophy

By

SANG WOOK KIM

Norman, Oklahoma

2020

Quantum Effects in Nodal-line Semimetals

A DISSERTATION APPROVED FOR THE

HOMER L. DODGE DEPARTMENT OF PHYSICS AND ASTRONOMY

BY THE COMMITTEE CONSISTING OF

Dr. Bruno Uchoa, Chair

Dr. Tomasz Przebinda

Dr. Michael Santos

Dr. Alberto Marino

Dr. Kieran Mullen

Acknowledgments

I would like to express my sincere gratitude to my advisor Bruno Uchoa. Bruno was a great advisor and friendly guide at University of Oklahoma, and he always spared support. Learning under his guidance was very interesting and allowed me to finish the Ph. D. program. His enthusiasm and knowledge enlightened my sight even when I was in a hard time. I have greatly benefited from the interactions with other faculty, students during my time at OU. I would like to thank Soumya Bhattacharya for making me laugh all the time. And, thanks to Kangjun Seo for his cooperation and advising.

My special thanks go to Geo Jose for his sincerity and kindness. He has sincerely answered and discussed any questions and been my best friend. Thanks also to Kieran Mullen, Alberto Marino, Michael Santos, and Tomasz Przebinda for agreeing to serve on my advisory committee.

Above all, I would like to thank my parents and my brother for their love and unwavering support.

The work presented here was supported in part by NSF CAREER Grant No. DMR- 1352604 and University of Oklahoma.

Abstract

Topological materials such as Dirac and Weyl semimetals have relativistic quasiparticles at a discrete number of points in the Brillouin zone. Those materials are semimetalas in the bulk but host metallic surface states that are protected by either symmetries or topological invariants. This thesis is about a class of quantum materials known as nodal line semimetals (NLSM), which have relativistic quasiparticles forming along lines. In three dimensions (3D), there are three types of crystalline symmetries that protect NLSMs. They can be classified by a combination of those symmetries which are inversion and time reversal symmetry, mirror reflection symmetry, and non-symmorphic symmetry.

In this thesis, we address various 3D Hall effects in a lattice realization of a NLSM known as the hyperhoneycomb lattice. We specifically address the 3D anomalous quantum Hall effect, which occurs through a topological quantum phase transition where the nodal line is gapped out by a Haldane mass. Because of the symmetry of the Haldane mass, the gap closes at a discrete number of points, which form Weyl points connected to each other through topological Fermi arcs. We also examine elastic gauge fields in the hyperhoneycomb lattice that generate nearly flat Landau levels in 3D. We propose a family of strain deformations that can be plausibly implemented with temperature gradients. In the 3D QAH phase, we also calculate dissipationless elastic Hall viscosity tensor.

In the last part, we address the hydrodynamics of relativistic quasiparticles in NLSMs. Hydrodynamics describes the universal behavior of quantum systems when transport is dominated by the collision between particles. It describes the long wavelength deviation of a quantum fluid from local thermal equilibration. We derive electrical conductivity and shear viscosity in the hydrodynamic regime by solving the quantum Boltzmann equation. In general, the lower the ratio between the shear viscosity and the entropy, the more strongly correlated a quantum system is expected to be. We show that the ratio between the shear viscosity and the entropy in NLSMs violates a conjectured lower bound applicable to ultra-correlated quantum systems. We show that both the longitudinal conductivity and the viscosity-entropy ratio η/s scale to zero at low temperature T, in contrast with relativistic systems in general, where the latter saturates to a constant, or Fermi liquids where η/s diverges at low T. We propose that the conjectured lower bound should be revisited to account for unscreened relativistic systems with a Fermi surface.

Contents

1 Introduction **1**

1.1 Introduction . . . 1

1.2 Outline . . . 2

2 From Dirac to Weyl fermions **5**

2.1 Single layer Graphene . . . 5

2.1.1 Tight-binding model . . . 5

2.1.2 Symmetry of graphene . . . 7

2.2 Topology and Chern number . . . 8

2.2.1 Berry phase and Berry curvature . . . 8

2.2.2 Masses in graphene . . . 9

2.3 Node-line semimetals . . . 10

2.3.1 Symmetries in node-line semimetals . . . 13

2.3.2 Material realization . . . 15

2.3.2.1 NLSMs with TR and I symmetry . . . 15

2.3.2.2 NLSMs with Mirror symmetry . . . 16

2.3.2.3 NLSMs with non-symmorphic symmetry . . . 17

2.4 Weyl semimetal . . . 18

2.4.1 Weyl fermion and chirality . . . 19

2.4.2 Topological properties of Weyl semimetals . . . 20

3 Quantum Anomalous Hall effect **23**

3.1 2D Quantum Anomalous Hall effect . . . 24

3.2 3D QAH transition for NLSMs . . . 26

3.2.1 Weyl fermions and topological surface states . . . 31

4 Elastic QHE and Elastic Hall viscosity **35**

4.1 Preview . . . 35

4.2 Elastic gauge field in hyperhoneycomb lattice . . . 36

4.3 Strain engineering . . . 38

4.4 Hall viscosity . . . 40

5 Hydrodynamic transport **46**
5.1 Introduction . . . 46
5.2 Quantum kinetic theory . . . 47
5.2.1 Equations of motion . . . 49
5.2.2 Hartree-Fock approximation & Born Collision approximation . . . 49
5.2.3 Boltzmann equation . . . 53
5.3 Background and graphene . . . 54
5.3.1 Conductivity . . . 55
5.3.2 Shear viscosity . . . 59
5.4 Transport coefficients in NLSMs . . . 63
5.4.1 Boltzmann equation in NLSMs . . . 63
5.4.2 Conductivity . . . 65
5.4.3 Shear viscosity . . . 68
5.4.4 Ratio η/s . . . 70

6 Conclusion **72**

A 2D Hall Conductance **74**

B Mean-field Hamiltonian of HHC lattice **76**

C Linearized Boltzmann Equation **80**

D Derivation of time dependent strain in a generic Hamiltonian **83**

E Collinear Regime Analysis **85**
E.1 Conductivity . . . 85
E.2 Shear Viscosity . . . 88

List of Figures

2.1 Honeycomb lattice 6
2.2 The energy dispersion of graphene 7
2.3 3D topological semimetals (TSM) 11
2.4 The surface state of Mackay-Terrones crystal 12
2.5 Schematic of different topological states 14
2.6 Band folding in one-dimensional polymers 15
2.7 Examples of NLSMs with TR and I symmetry 16
2.8 The three examples of NLSMs with TR and I symmetry 17
2.9 Crystal structure of the HfSiS. 18
2.10 Bulk and surface of Weyl semimetals 20
2.11 Weyl semimetal (WSM) and Dirac semimetal (DSM) 22

3.1 Honeycomb lattice with NN interaction and NNN interaction 24
3.2 Phase diagram of graphene 27
3.3 Hyperhoneycomb lattice with four sublattice and BZ 27
3.4 xz and yz planes of the hyperhoneycomb lattice with current loops 28
3.5 Mean field phase diagram of the hyperhoneycomb lattice. 30
3.6 Mass gap and Weyl point in QAH state of the hyperhoneycomb lattice 32
3.7 Fermi arcs on the (001) surface of BZ 33

4.1 Pseudomagnetic field along the nodal line for two strain field configurations 38
4.2 Energy of the Landau levels (LLs) around the nodal line 40
4.3 Elastic deformation and Temperature gradient 41

5.1 Illustration of the golden rule diagrams for collision integral 57
5.2 Illustration of the Fermi surface of a NLSM. 64

B.1 Four NNN loops 77

List of Tables

5.1 W tensors 68
5.2 Q tensors 68

Chapter 1

Introduction

1.1 Introduction

In 2016, David Thouless, Duncan Haldane, and Michael Kosterlitz won the Nobel Prize for 'theoretical discoveries of topological phase transitions and topological phases of matter'. Topological phase transitions are not ordinary phase transitions, like that between gas, liquid and solid. For instance, when the temperature of matter is close to absolute zero (–273 degrees Celsius), one can find extraordinary phenomena such as superconductors and superfluids. The former occurs when the electrical resistance becomes zero, and the latter is a phenomenon in which the viscosity in a fluid vanishes. Interestingly, 2D superconductors can spontaneously form vortices, which remain bounded to each other in pairs below a certain temperature. Another mysterious phenomenon that David Thouless described theoretically is the quantum Hall effect. It was discovered in 1980 by the German physicist Klaus von Klitzing, who was rewarded with the Nobel Prize in 1985. The electrical conductance in the 2D layer of a material only takes an integer multiple of a certain value. This quantization of the conductance is extremely precise even if temperature, magnetic field or the amount of impurities vary. This phenomenon is known as the integer quantum Hall effect.

The key insight from David Thouless was to realize that these unusual phenomena could be explained by topology. In mathematics, topology describes some invariant number which remains intact when the geometry of space or fields is stretched, twisted or deformed without tearing apart. For example, the number of holes in some geometrical shape can only be changed by an integer number. Shapes with different number of holes belong to different classes because they cannot be continuously deformed into one another. A few years later, Duncan Haldane discovered that topological phases of matter, which are similar to the quantum Hall effect, can be found in simple lattices even when there is no magnetic field (quantum anomalous Hall effect). The Haldane model was validated in an experiment using atoms that were cooled to almost absolute zero [143]. Nowadays, many topological materials have been predicted and discovered. The topic has fascinated physicists and created the expectation that it could lead to technological breakthroughs with new generations of electronics and quantum computers.

In this thesis, we address a special class of topological materials where the low energy electronic

excitations behave as relativistic massless neutrinos. Unlike in graphene, the atomically thick layer of carbon, those excitations exist along lines of the Brillouin zone, the phase space for electrons moving in a periodic crystal. This class of materials is known as nodal-line semimetals (NLSMs), which are the main subject of this thesis. Analogously to the Haldane model, we address topological phase transitions in NLSMs exhibiting the quantum anomalous Hall effect in 3D. We also explore the exotic situation where the quantum Hall effect is driven by strain, which is also achieved without strong external magnetic fields. Elastic deformations in lattices of nodal semimetals can give rise to magnetic fields which can be strong enough to generate a quantum Hall effect, depending on the configuration of deformations, while the total magnetic flux is zero.

Finally, we explore a connection between quantum mechanics and conventional fluid dynamics in a special regime called quantum hydrodynamics. Although relativistic particles which are as fast as the speed of light seem very unlike classical particles in fluids, there is a correspondence that can be made when electrons collide with each other very strongly and very often. In that situation, the collective motion of electrons is governed by basic conservation laws, and their flow can acquire a viscous character, like in the flow of water. The diffusive dynamics of electrons in that regime is governed by the Navier-Sokes equation for classical fluids, and can display exotic properties such as quantum turbulence. From the point of view of quantum statistical mechanics, the long wavelength deviations of the system away from thermal equilibrium is described by the Boltzmann equation. Hence, transport coefficients, such as viscosities and conductivity can be theoretically derived. We describe the novel hydrodynamic behavior of electrons in NLSMs and predict the unique temperature dependence of the conductivity and viscosity-entropy ratio, which indicate unusually strong electronic correlations. We hope that this study will instigate experimentalists to conduct transport experiments in these intriguing systems in the future.

1.2 Outline

Generic metallic states occur in systems that host Fermi surfaces. In one dimensional (1D) systems with effective short-range interactions among the fermions, these metallic states are described by the Tomonaga–Luttinger model [1–5]. Above 1D, Landau's Fermi liquid theory provides theoretical framework for interacting fermions [6]. Metallic phases are also realized in systems where a filled valence band touches a conduction band. Those are called *semi-metallic* states, and they exhibit gapless excitations about a zero-energy manifold in the Brillouin zone (BZ). Although semi-metals had been theoretically predicted in 1970s [7], their properties have garnered attention more recently with the discovery of graphene (see [8] and references therein) and other Dirac materials.

Dirac semi-metallic systems have quasiparticles around gapless points of the Brillouin zone where they show a relativistic dispersion relation. The Fermi surface vanishes at the charge neutral point and may exhibit interesting quantum effects, from quantum phase transitions to unconventional quantum Hall effects. In those systems, one can draw a connection between the Chern-Simon's field theory, which is the theoretical framework for the quantum Hall effect (QHE), and the study of

topological materials. Weyl semimetals (WSMs), whose quasiparticles are described by the massless limit of the three dimensional (3D) Dirac equation, the Weyl equation, are also studied for their connection with the anomalous quantum Hall effect in 3D (see chapter 3).

In recent years, 3D semi-metals with a ring or line of gapless points in the Brillouin zone have been discovered. Nodal-line semimetals (NLSMs) have nodal lines in their bulk which are topologically protected by symmetries and have distinguished surface states, called 'drumhead' surface states [49]. They are also related to many other topological semimetals by either the presence or absence of spin-orbit coupling (SOC) and lattice symmetries, as briefly discussed in chapter 2.3.

This thesis has four main parts. Chapter 2 introduces the systems which could host Dirac and Weyl fermions. We review a simple single layer graphene as an example of Dirac system in Section 2.1. Then, we discuss the theoretical approach based on concepts like *Berry phase* and *Berry curvature* to understand topological materials. We also discuss how to introduce a topological *'mass'* to Dirac fermions in Section 2.2.2. Beyond two-dimensional (2D) systems, we review topological semimetals - Dirac semimetals (DSMs), Weyl semimetals and node-line semimetals (NLSMs), which are the focus of this thesis. In particular, we describe the symmetry groups which protect nodal lines, and their material realization in Section 2.3. We also introduce concept of Weyl fermions and Weyl semimetals, which have a unique topological surface states in Section 2.4 and will be relevant to some of the subsequent chapters.

Chapter 3 is devoted to the quantum anomalous Hall (QAH) effect. As an introduction of QAH with a lattice structure, we introduce the Haldane model for the honeycomb lattice. In the following section, we investigate 3D QAHE for 3D node-line semimetal which has the similar current loops. We provide possible topological instabilities and their phase diagram. We confirmed the topological phase transition to Weyl semimetals with emergence of Weyl points and Fermi arcs in QAH state.

In Chapter 4, we address the role of elasticity in quantum Hall effects. We start with the concept of *elastic gauge fields* which can produce Landau level quantization in systems with relativistic electrons in the absence of external magnetic fields. The chapter continues with the analysis of the hyper-honeycomb lattice, which is shown to host a 3D zero-field quantum Hall effect with a proper physical implementation based on thermal gradients. In Section 4.4, we turn to different transport characteristic under strain, which is called *the Hall viscosity*. This property is a non-dissipative viscous response of quantum fluids that break time reversal symmetry.

Finally, in Chapter 5, we discuss the hydrodynamic properties of relativistic quantum fluids. We start in Section 5.1 with a theoretical background and methods to analyze and calculate transport properties in the hydrodynamic regime. This chapter includes the quantum Boltzmann equation, which determines the collision dominant transport phenomena. In Section 5.3, we review the literature about hydrodynamics of graphene, in particular the electrical conductivity and the shear viscosity. In Section 5.4, By solving the quantum kinetic theory for a nodal-line semimetal in the hydrodynamic regime, calculate the longitudinal conductivity and the shear viscosity. We show that unscreened relativistic systems with a Fermi surface (such as a NLSM) violate a established conjecture for the lower bound of the ratio between the sheer viscosity and the entropy. Note that,

unless otherwise stated, we will use units in which the reduced Planck constant $\hbar = 1$.

Chapter 2

From Dirac to Weyl fermions

2.1 Single layer Graphene

2.1.1 Tight-binding model

Carbon is the 15th most abundant element in the Earth's crust and has vast diversity of organic & inorganic compounds. In condensed matter physics, carbon-based systems show many different physical properties that depend on their structures. Among various allotropes of carbon, graphene is a two dimensional material consisting of carbon atoms ordered in a honeycomb lattice. The honeycomb lattice has two atoms per unit cell, and the primitive lattice vector is

$$\boldsymbol{a_1} = \frac{a}{2}\left(\sqrt{3}, 3\right), \ \boldsymbol{a_2} = \frac{a}{2}\left(-\sqrt{3}, 3\right) \tag{2.1}$$

where a is the interatomic distance (or the lattice constant). The basis vector is given by $\boldsymbol{v_1} = (0, 0)$ and $\boldsymbol{v_2} = (0, -a)$, and the two-atomic basis is depicted by the white and black spheres in Fig 2.1. The tight-binding Hamiltonian model for graphene can be defined as

$$\mathcal{H}_{0,r} = \sum_{\langle \mathbf{r_n}, \mathbf{r_m} \rangle} -t_{nm} \left(\hat{a}^\dagger \left(\mathbf{r_n} \right) \hat{b} \left(\mathbf{r_m} \right) + \hat{a} \left(\mathbf{r_n} \right) \hat{b}^\dagger \left(\mathbf{r_m} \right) \right) \tag{2.2}$$

where the fermionic operator $\hat{a}^\dagger \left(\mathbf{r_n} \right)$ and $\hat{b}^\dagger \left(\mathbf{r_m} \right)$ creates an electron at the site $\mathbf{r_n}$ and $\mathbf{r_m}$ respectively, while $\hat{a} \left(\mathbf{r_n} \right)$ and $\hat{b} \left(\mathbf{r_m} \right)$ annihilate an electron from the respective sites. The location of two different sublattice is represented as $\mathbf{r_n}$ and $\mathbf{r_m}$. The kinetic energy needed to jump between the nearest neighbor site is given by the hopping matrix element t_{nm}. The bracket notation in the summation indicates we avoid double counting and only consider the adjacent sites for the combined space of $\mathbf{r_n}$ and $\mathbf{r_m}$. In other words, we restrict the system to only have nearest neighbor hopping. The Fourier transformation $\hat{c} \left(\mathbf{r_m} \right) = \frac{1}{\sqrt{N}} \sum_{\mathbf{k}} e^{i \mathbf{k} \cdot \mathbf{r}} \hat{c} \left(\mathbf{k} \right)$ with $\hat{c} \in \left\{ \hat{a}, \hat{b} \right\}$ gives the Hamiltonian in

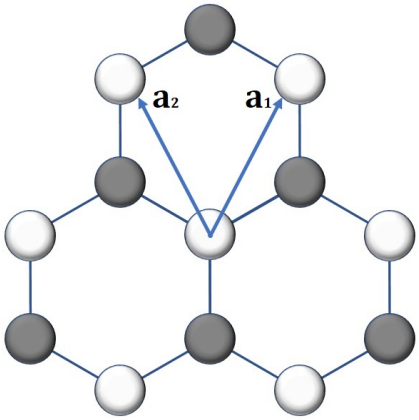

Figure 2.1: The structure of graphene is a honeycomb lattice with the primitive lattice vector $\boldsymbol{a_1}$ and $\boldsymbol{a_2}$. It has two basis atoms in its unit cell depicted by the white and black spheres. The nearest neighbor vectors are $\mathbf{d_n} = \boldsymbol{\delta_n} + \boldsymbol{v_2} - \boldsymbol{v_1}$ where $\boldsymbol{\delta_1} = (0, 0)$, $\boldsymbol{\delta_2} = \boldsymbol{a_1}$, and $\boldsymbol{\delta_3} = \boldsymbol{a_2}$.

momentum space which is

$$\mathcal{H}_0(\mathbf{k}) = -t \sum_{\mathbf{k}} \begin{pmatrix} \hat{a}^\dagger_{\mathbf{k}} & \hat{b}^\dagger_{\mathbf{k}} \end{pmatrix} \begin{pmatrix} 0 & h_{\mathbf{k}} \\ h^*_{\mathbf{k}} & 0 \end{pmatrix} \begin{pmatrix} \hat{a}_{\mathbf{k}} \\ \hat{b}_{\mathbf{k}} \end{pmatrix} \tag{2.3}$$

where $h_{\mathbf{k}} = \sum_n e^{i\mathbf{k}\cdot\boldsymbol{\delta_n}}$. $\boldsymbol{\delta_n}$ is the displacement vector to the nearest sites, and with our choice of the primitive vectors for honeycomb lattice, we find $h_{\mathbf{k}} = e^{ik_y a}\left(1 + 2\cos\left(\frac{\sqrt{3}}{2}k_x a\right) e^{-i\frac{3}{2}k_y a}\right)$. We can find energy eigenvalue of the 2×2 matrix with $h_{\mathbf{k}}$, and it shows the energy dispersion of graphene consists of two energy bands which are given by:

$$\epsilon_k^{(\pm)} = \pm t\,|h_{\mathbf{k}}| = \pm t\sqrt{3 + 2\cos\left(\sqrt{3}k_x a\right) + 4\cos\left(\frac{\sqrt{3}}{2}k_x a\right)\cos\left(\frac{3}{2}k_y a\right)}. \tag{2.4}$$

Interestingly, the two energy bands touch at $\mathbf{k} = \frac{4\pi}{3a}(\pm 1, 0)$ (and 3 copies of them due to three fold symmetry as in Fig 2.2). These two points are known as *Dirac points*, and a linear energy dispersion emerges around these Dirac points. By expanding the function $h_{\mathbf{k}}$ around the two points, we can find the low energy Hamiltonian which is also Dirac Hamiltonian.

$$H_D = v_F \int_{\mathbf{q}} \begin{pmatrix} a^\dagger_{K_+} \\ b^\dagger_{K_+} \\ b^\dagger_{K_-} \\ a^\dagger_{K_-} \end{pmatrix}^T \begin{pmatrix} 0 & q_x - iq_y & 0 & 0 \\ q_x + iq_y & 0 & 0 & 0 \\ 0 & 0 & 0 & -q_x + iq_y \\ 0 & 0 & -q_x - iq_y & 0 \end{pmatrix} \begin{pmatrix} a_{K_+} \\ b_{K_+} \\ b_{K_-} \\ a_{K_-} \end{pmatrix} \tag{2.5}$$

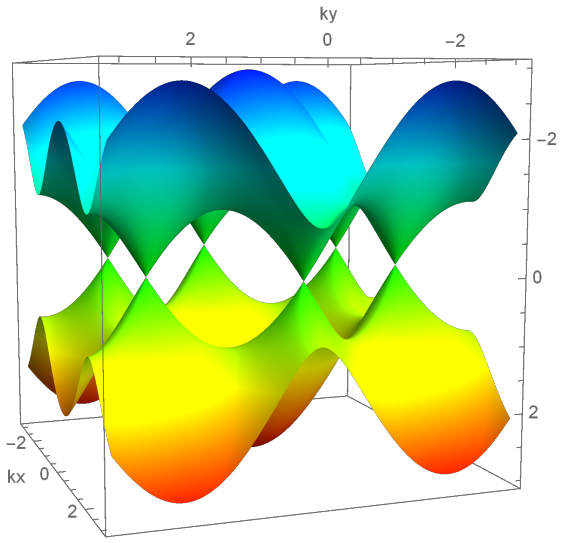

Figure 2.2: The energy dispersion of graphene. The two energy bands touch at six points in the first Brillouin zone where they are called *Dirac points*. A linear energy spectrum emerges around these points.

$\mathbf{q}$ is the relative momentum to the Dirac points $K_\pm$, and $v_F = 3ta/2$ is the Fermi velocity ($\approx 10^6\ m/s$ [8]). In compact way,

$$H_{\text{Dirac}} = v_F \int_{\mathbf{q}} \hat{\Psi}^\dagger_{\mathbf{q}} \tau_z \otimes (k_x \sigma_x + k_y \sigma_y)\, \hat{\Psi}_{\mathbf{q}}, \tag{2.6}$$

where the Pauli-matrices τ_z describes the valley subspace and σ_x, σ_y describes the pseudo-spin arises from the two sublattices of graphene.

2.1.2 Symmetry of graphene

For the topology we will address in the next chapter, a symmetry is an important concept. Among many class of symmetry, spatial inversion $\mathcal{P}$ and time reversal $\mathcal{T}$ symmetry (together, $\mathcal{PT}$ symmetry) are interesting. The spatial inversion implies $\mathbf{r} \to -\mathbf{r}$ in the field theory and exchanges both the 'A' and 'B' sublattices as well as the Dirac points $K_\pm$. $\mathcal{P}$ operator acting on the spinor in (2.5) gives

$$\mathcal{P} \begin{pmatrix} a_{K_+}(\mathbf{k}) \\ b_{K_+}(\mathbf{k}) \\ b_{K_-}(\mathbf{k}) \\ a_{K_-}(\mathbf{k}) \end{pmatrix} \to \begin{pmatrix} b_{K_-}(-\mathbf{k}) \\ a_{K_-}(-\mathbf{k}) \\ a_{K_+}(-\mathbf{k}) \\ b_{K_+}(-\mathbf{k}) \end{pmatrix} \tag{2.7}$$

and $\mathcal{P}^2 = 1$. Corresponding matrix representation for the $\mathcal{P}$ operator is $\tau_x \otimes \sigma_0$ where σ_0 is the 2×2 identity matrix. If the Hamiltonian satisfy $\mathcal{P} H(\mathbf{k}) \mathcal{P}^{-1} = H(-\mathbf{k})$, the spatial inversion symmetry holds. On the other hands, the time reversal $\mathcal{T}$ implies $\mathbf{t} \to -\mathbf{t}$ in the field theory and

only interchanges the Dirac points and the spin. The spinors under time reversal become as

$$\mathcal{T}\begin{pmatrix} a_{K_+}(\mathbf{k}) \\ b_{K_+}(\mathbf{k}) \\ b_{K_-}(\mathbf{k}) \\ a_{K_-}(\mathbf{k}) \end{pmatrix} \rightarrow \begin{pmatrix} a_{K_-}(-\mathbf{k}) \\ b_{K_-}(-\mathbf{k}) \\ b_{K_+}(-\mathbf{k}) \\ a_{K_+}(-\mathbf{k}) \end{pmatrix}. \tag{2.8}$$

Corresponding matrix representation for the $\mathcal{T}$ operator is $\tau_x \otimes \sigma_x$. The time reversal symmetry holds when the Hamiltonian satisfy $\mathcal{T}H^*(\mathbf{k})\mathcal{T}^{-1} = H(-\mathbf{k})$ (note the complex conjugator). If there is no interactions, both of $\mathcal{P}$ and $\mathcal{T}$ symmetry is conserved.

Another symmetry to be considered for the Dirac system is chirality. In short, it is Lorentz invariant quantity which can be obtained by chiral projection. The chiral projection is one way to define the "handedness" of the particles when Dirac spinor Ψ can be represented as $\Psi = \Psi_L + \Psi_R$. We will discuss about it in chapter 2.4. The chirality of two Dirac cones have the opposite chirality.

2.2 Topology and Chern number

2.2.1 Berry phase and Berry curvature

Berry's phase [11] (simply Berry phase) is a correction to the quantum adiabatic theorem, which describes a quantum phase effect that emerges from a slow, cyclic evolution. We can derive the Berry phase in the context of the quantum adiabatic theorem [12]. Consider a Hamiltonian $\mathcal{H}(\mathbf{R})$ in the parameter space $\{R_1, R_2, \cdots, R_N\}$. Let's assume $\mathcal{H}(\mathbf{R})$ has an discrete and non degenerate eigenvalue $E_i(\mathbf{R})$ with an eigenstate $|\Psi_i(\mathbf{R})\rangle$. If the vector $\mathbf{R}$ changes in time, the initial state will not be an exact solution of the time-dependent Schrödinger equation. However, if the change is slow enough (as known as adiabatic change), the system does not jump to another eigenstate. To be specific, let $\mathbf{R}(t/T)$evolve over a time interval $0 \leq t \leq T$, where T is large enough. At time $t = 0$, the system is in the state $|\Psi_i(\mathbf{R}(0))\rangle$. As T approaches to infinity, the probability of the final state $e^{i\phi_i(T)}|\Psi_i(\mathbf{R}(1))\rangle$ approaches to 1 with the phase factor $\phi_i(t)$. By substituting $e^{i\phi_i(t)}|\Psi_i(\mathbf{R})\rangle$ into time-dependent Schrödinger equation,

$$i\hbar\frac{d}{dt}e^{i\phi_i(t)}|\Psi_i(\mathbf{R})\rangle = H(\mathbf{R})\,e^{i\phi_i(t)}|\Psi_i(\mathbf{R})\rangle, \tag{2.9}$$

and projecting both sides of the equation onto $e^{i\phi_i(t)}|\Psi_i(\mathbf{R})\rangle$:

$$i\langle\Psi_i(\mathbf{R})|\nabla_{\mathbf{R}}|\Psi_i(\mathbf{R})\rangle \times \frac{d\mathbf{R}}{dt} - \frac{d\phi_i(t)}{dt} = \frac{1}{\hbar}E_i(\mathbf{R}). \tag{2.10}$$

Thus,

$$\begin{aligned}\phi_i(t) - \phi_i(0) &= \int_0^t dt' \left[i \langle \Psi_i(\mathbf{R}) | \nabla_{\mathbf{R}} | \Psi_i(\mathbf{R}) \rangle \frac{d\mathbf{R}}{dt'} - \frac{1}{\hbar} E_i(\mathbf{R}) \right] \\ &= \int_{\mathbf{R}(0)}^{\mathbf{R}(T)} d\mathbf{R} \langle \Psi_i(\mathbf{R}) | i\nabla_{\mathbf{R}} | \Psi_i(\mathbf{R}) \rangle - \frac{1}{\hbar} \int_0^t dt' E_i(\mathbf{R}) . \end{aligned} \tag{2.11}$$

The phase factor has two parts: the factor with the integrand $A_B \equiv \langle \Psi_i(\mathbf{R}) | i\nabla_{\mathbf{R}} | \Psi_i(\mathbf{R}) \rangle$ (Berry connection) and the dynamical phase. When we consider two different paths which have the same endpoints $\mathbf{R}(0)$ and $\mathbf{R}(1)$ in the parameter space, and the system evolves in a superposition of two states with each path. The Berry phase is the difference between Berry connection integrated along the two paths, and is equivalent to the integration along a closed path. Due to its gauge invariance[1], the Berry phase is uniquely defined.

In condensed matter physics, we consider the Berry phase in a lattice system, where a non-interacting electron is described by Bloch wave functions $\psi_n(\mathbf{r}) = e^{i\mathbf{k}\cdot\mathbf{r}} u_n(\mathbf{r})$. n is the band index and $u_n(\mathbf{r})$ is periodic in space. Similar to the Berry phase, Berry curvature $\Omega_n(\mathbf{q})$ is gauge invariant in momentum space and can be defined analogously to the definition of a magnetic field in electrodynamics:

$$\Omega_n(\mathbf{q}) = \nabla_{\mathbf{q}} \times \langle \psi_n(\mathbf{q}) | i\nabla_{\mathbf{q}} | \psi_n(\mathbf{q}) \rangle , \tag{2.12}$$

or equivalently,

$$(\Omega_n)_{\mu\nu} = \frac{\partial}{\partial q^\mu} (A_n)_\nu - \frac{\partial}{\partial q^\nu} (A_n)_\mu \tag{2.13}$$

where $A_n(\mathbf{q})$ is Berry connection in momentum space.

2.2.2 Masses in graphene

As we mentioned in chapter 2.1, semimetallic graphene exhibits robust massless Dirac fermions protected by space inversion and time reversal symmetries. In this section, we discuss how we can introduce a mass term which is anticommuting with the Hamiltonian of semimetallic graphene. In the two band model of spinless fermions on a bipartite lattice, the only matrix that anticommutes with the low energy Hamiltonian $H_0 = v_F(q_x\sigma_x + q_y\sigma_y)$ is the third Pauli matrix σ_3. For spinless fermions on the honeycomb lattice, which has two valleys, there are 4 possible mass terms (Semenov, Haldane and two Kekule distortions) which all break some lattice symmetry [13].

The semenov insulator is the simplest case for a mass term. It corresponds to a staggered on-site potential that breaks only parity (sublattice) symmetry. The spectrum of the bulk excitations is given by $E^2 = v_F^2 p^2 + M^2$ and there is no edge state. Haldane proposed a Chern insulator, which exhibits quantized Hall conductance in the absence of the Landau level structure [14]. By introducing local fluxes which sum up to zero over each unit cell, this mass breaks time reversal ($\mathcal{T}$) symmetry while preserving the lattice translational symmetry. These fluxes cannot be achieved

[1] An arbitrary phase factor $e^{i\Lambda(R)}$ onto eigenstate will give $-\nabla_{\mathbf{R}}\Lambda(R)$ added to Berry connection, but the Berry phase is unchanged since it is integrated along a closed path.

by the first-neighbor hoppings because the closed path would enclose a complete unit cell. By introducing unimodular phase factors in the second neighbor hopping amplitudes, it gives the third Pauli matrix component whose sign depends on their chiralities. For complex hoppings, the term proportional to σ_3 opens gaps at the Dirac points and breaks $\mathcal{T}$ symmetry. This state is known as the anomalous quantum Hall (QAH) effect, which has topological chiral edge currents. This state will be discussed in detail in chapter 3.1.

While the Haldane model for spinless fermions on the honeycomb lattice exhibits the topologically protected integer quantum Hall effect, Kane and Mele proposed a generalization of the Haldane model which includes the spin in the presence of the spin–orbit interaction. When the spin is coupled to electronic motion, spin–orbit coupling opens a gap at the Dirac points without breaking any of fundamental symmetries ($\mathcal{P}$ and $\mathcal{T}$) [16, 17]. As a result, the Kane–Mele insulator shows a Quantum Spin Hall (QSH) state, which corresponds to two copies of the QAH state, with topologically protected spin currents. This new state of matter cannot be adiabatically connected to a trivial atomic insulator without closing (and re-opening) the bulk gap [13].

2.3 Node-line semimetals

After the discovery of topological insulators (TIs), topologically non-trivial states of matter have been a hot topic in condensed matter physics. TIs exhibit insulating bulk while maintaining robust metallic surface states which are topologically protected by time reversal symmetry [18, 19]. In response to great research interest, topological semimetals (TSM) such as Dirac and Weyl semimetals were discovered which can also host metallic surface states with a semi-metallic bulk [20]. In three dimensional TSM, there are three types: Dirac (DSM), Weyl (WSM), and nodal-line semimetals (NLSM). A DSM is, as 2D Dirac system, the result of two doubly degenerate bands crossing near the Fermi level at Dirac point, a discrete point in k-space. Dirac point has a energy band dispersion which is linear in momentum k. the low-energy excitations near the linearly dispersed points are described by Dirac fermions, which is shortly discussed in chapter 2.1. The existence of a 3D DSM was experimentally confirmed by angular-resolved photoemission spectroscopy (ARPES) in Na_3Bi [21, 22] and Cd_3As_2 [23–25].

When either inversion symmetry or time-reversal symmetry is broken, the Dirac point is separated into two singly degenerate band crossings called Weyl points. They can only appear in pairs of opposite chirality, which we discuss in chapter 2.4. The evidence of Weyl fermions in condensed matter systems has first been observed in inversion symmetry-breaking compounds TaAs [34–36], NbAs [37], TaP, NbP [38, 39] as well as in photonic crystals [40]. They have also been observed in other inversion symmetry-breaking materials such as $MoTe_2$ [41–44], WTe_2 [45], $Me_xW_{1-x}Te_2$ [46–48].

More recently, another area of interest in topological quantum matter is devoted to the topic of topological nodal line semimetals, materials in which Dirac or Weyl points form along special *lines* in momentum space [See Fig. 2.3c]. Those band crossings create either a closed ring or line of

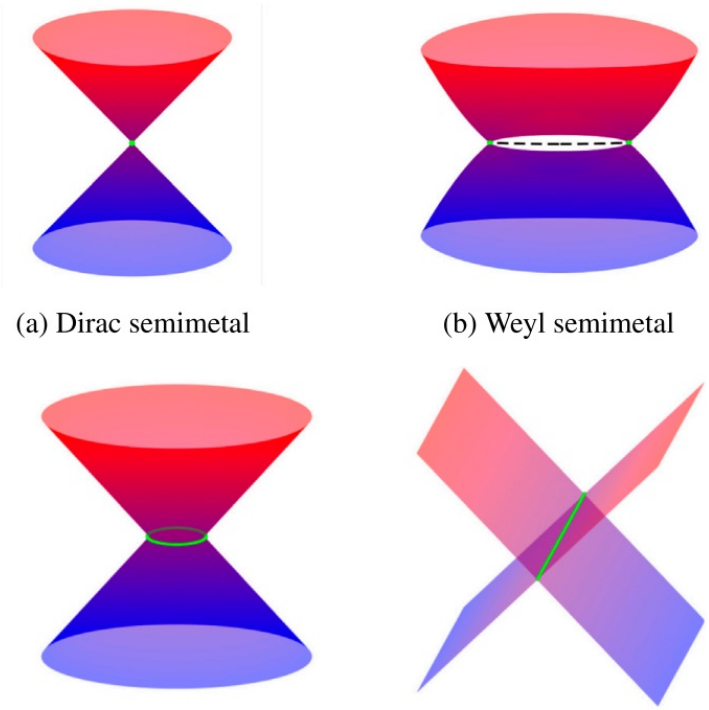

(a) Dirac semimetal

(b) Weyl semimetal

(c) Nodal line semimetals

Figure 2.3: Schematic illustration of 3D topological semimetals (TSM) with (a) Dirac node, (b) Weyl node and (c) Nodal ring & line in momentum space. (a) The Dirac point where the bands are linearly dispersed is shown by the green dot. (b) A pair of Wyle nodes with opposite chirality are shown by the green dot. (c) Nodal line semimetals with band crossing lines in momentum space forming either a ring or line.

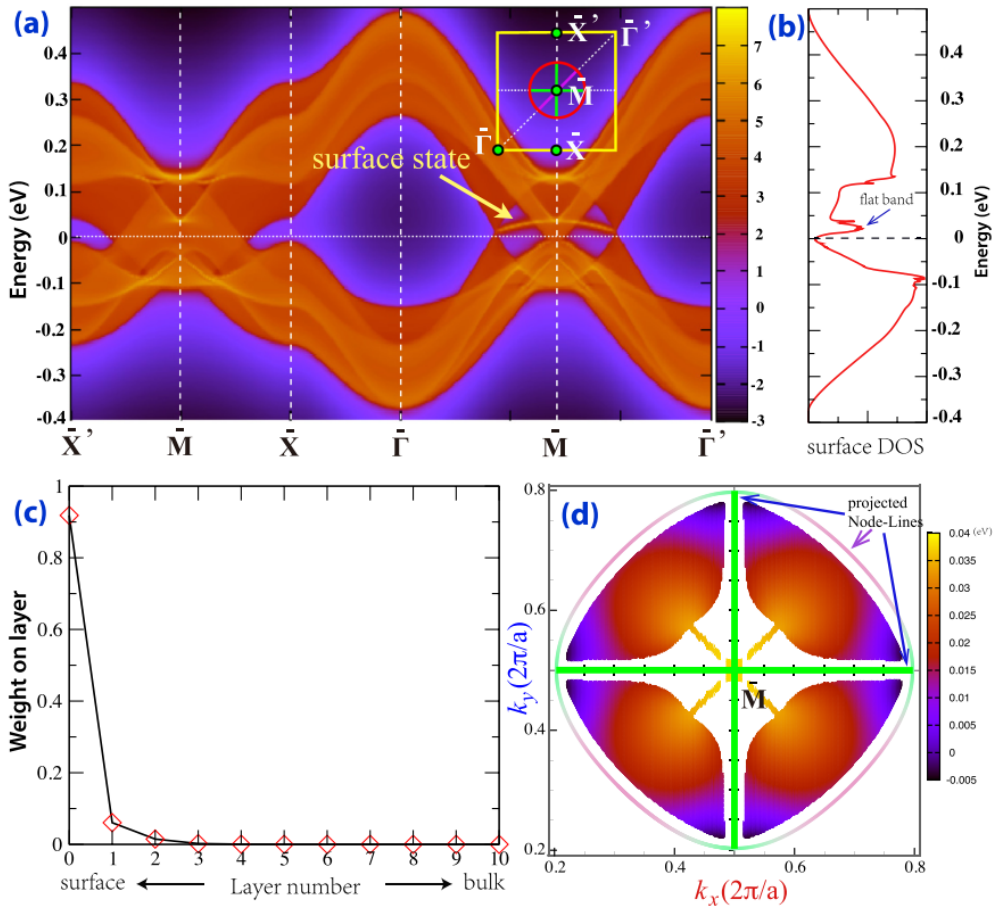

Figure 2.4: The (001)-surface state of Mackay-Terrones crystal calculated with *ab initio* methods. (a) The nearly flat surface band is nestled between two solid Dirac cones, which are the projection of one of the node-line circles as indicated in the inset (red circle). The two orthogonal diameters (green line) are showing the projection of two other node-line rings . (b) The surface density of state. (c) The wave function of the surface state decays rapidly into bulk. (d) The eigenenergy distribution of a surface flat band nestled inside of a projected node-line circle, which looks like a vibration model of a "drumhead." The mixing of surface and bulk states leads to discontinuity in this plot [49].

degeneracies, rather than discrete points. Nodal ring semimetals are characterized by the appearance of a 2D topological 'drumhead' surface state [see Fig 2.4]. The surface states have a distinguishing characteristic, which is they are embedded inside the 'direct gap' between conduction and valence bands in the 2D projection of the nodal ring [50, 51]. The flat band surface states could potentially realize high-temperature superconductivity, magnetism, or other correlated effects [52, 53]. Here, we review some of the experimentally confirmed and theoretically predicted topological nodal line semimetals, focusing in particular on the symmetry protection mechanisms of the nodal lines in various materials.

2.3.1 Symmetries in node-line semimetals

Crystallographic symmetries are key to understand NLSMs. Their topological properties are protected by some symmetries, and hence they can be classified by those symmetries. There are three types of crystalline symmetries that generate NLSMs, including combination of inversion and time reversal symmetry, mirror reflection symmetry, and non-symmorphic symmetry. The non-symmorphic symmetry includes glide mirror or screw rotation. In the absence of spin-orbit coupling (SOC), those crystals are called Dirac node-line semimetal (DNLS). The effect of SOC on DNLS with preserved/broken symmetry could lift or keep the degeneracy and gives various topological states including Weyl Nodal Line Semimetal (WNLS). A schematic diagram for those states and symmetry requirements are shown in Fig 2.5.

As the first recipe of DNLS, presence of time reversal (TR) and inversion (I) symmetries is required. In the perspective of Berry phase we introduced in chapter 2.2.1, inversion and time-reversal symmetry restrict the Berry phase $\phi(k)$ on a closed loop in momentum space k_L to satisfy $\phi(k_L) = \phi(-k_L)$ and $\phi(k_L) = \phi(-k_L)^*$. Where $\phi(k_L) = -1$, means that the loop contains a degeneracy. In 3D, this guarantees a small nodal loop [54]. In the presence of SOC, Dirac nodes are gapped out, turning the system into a TI. However, if the system has an additional $C_{n=3,4,6}$ rotation symmetries, the band crossing at certain generic discrete points can be protected. Everywhere else in the BZ is gapped, thus it give rise to a 3D DSM in the SOC regime [55].

Another symmetry description of DNLS is when the mirror operation and the Hamiltonian commute. Mirror reflection symmetry generates and protects nodal rings in the absence of SOC. Suppose 3D Hamiltonian $H(k_x, k_y, k_z)$ has the mirror symmetry such as $M_{xy}H(k_x, k_y, -k_z)M_{xy}^{-1} = H(k_x, k_y, k_z)$ where M is mirror reflection operator. The mirror operation and the Hamiltonian commute in $k_z = 0, \pi$ planes, which means they can simultaneously diagonalized and labeled by eigenvalue of M, ± 1.

Finally, non-symmorphic symmetry can be understood as a combination of a point group symmetry operation and a lattice translation. For example, glide mirror of square lattice is invariant under lattice translation plus reflection. Such symmetry has energy bands which can be described by inverse process of band folding. This concept was first introduced by Hoffmann in 1987 [57]. Let's consider 1D chain of atom. If two atoms form a bonding or antibonding states, we can consider the system as a 1D lattice two atoms in a unit cell. The bonding branch disperse upward while

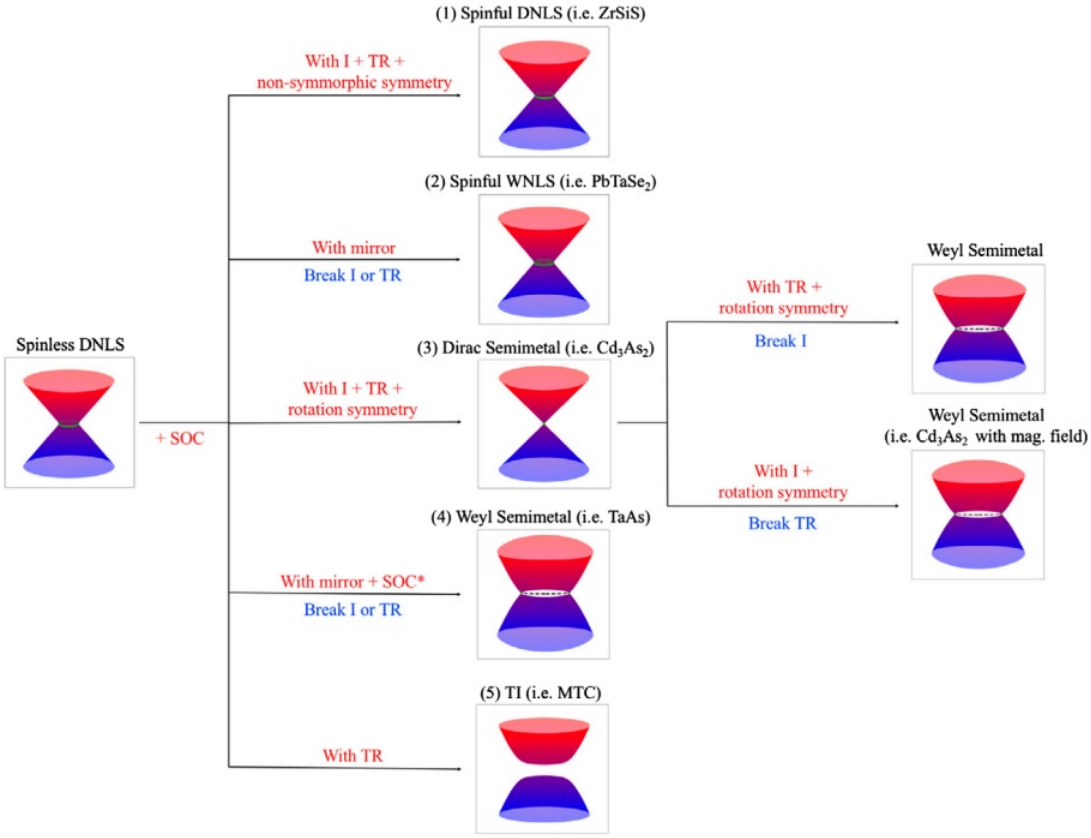

Figure 2.5: Schematic of different topological states and the relationship in symmetry elements with spin-orbit coupling (SOC). [56]

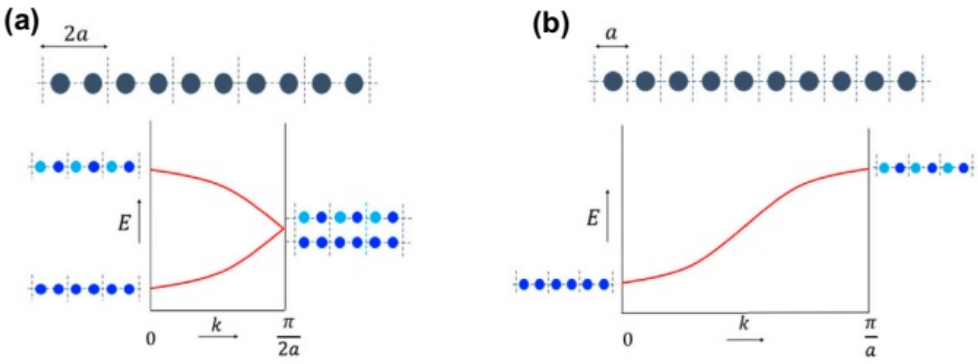

Figure 2.6: Band folding in one-dimensional polymers [56]. (a) Band structure of a 1D polymer where a unit cell contains two atoms. It has two branches from a bonding band and antibonding band starting from $k = 0$. Definitely, energy of antibonding is higher than one of bonding and the two branches should intersect at $k = \pi/2a$. (b) Band structure of a polymer in which there is one atom per unit cell. The BZ is twice as big as (a).

antibonding goes downward, and they are degenerate precisely at $k = \pi/2a$. When the polymer is regarded as having one atom per unit cell, the Brillouin zone (BZ) gets larger, and energy band must carry the same information because physics cannot be changed by a suitable choice of the unit cell. Thus, a branch looks like 'unfolded' (See Fig 2.6). What happens in non-symmorphic symmetry crystals is similar. The lattice translation element of non-symmorphic symmetry do not conserve spatial origin and causes enlargement of a unit cell in comparison to the symmorphic space group. The enlargement of a unit cell is analogous to the two atoms unit cell situation discussed above. Thus, it causes the folding of k-space, and forces a band degeneracy the BZ boundary. The node line protected by a non-symmorphic symmetry cannot be gapped by SOC due to the lattice translation element [58]. Hence, the bands crossings are protected by non-symmorphic symmetries with or without SOC.

2.3.2 Material realization

2.3.2.1 NLSMs with TR and I symmetry

Centrosymmetric materials with time-reversal (TR) symmetry are protected by both of TR and inversion symmetry, and fourfold degeneracies along nodal rings can be realized in the limit of vanishing SOC effect. SOC typically lifts some or all degeneracies. Cu_3NX group has Cu_3N crystal in the cubic anti-RuO_3 structure in space group Pm-3m No. 221. An example with intercalate atoms of Pd was proposed in 2015 [54] (Fig 2.7a, d). CaTe is a CsCl-type structured alkaline-earth chalcogenide also in the space group [59]. Without SOC, three nodal rings are perpendicular to each other, as shown in Fig 2.7e. The family of lanthanum monopnictides LaX has the rock salt structure in space group Fm-3m No. 225, where X could be N, P, As, Sb, or Bi [60–65]. Most of them are predicted to be TI with SOC, but recent transport measurements gave some evidence of semimetal behavior [62–64]. Ca_3P_2 has the hexagonal Mn_5Si_3-type crystal structure with space

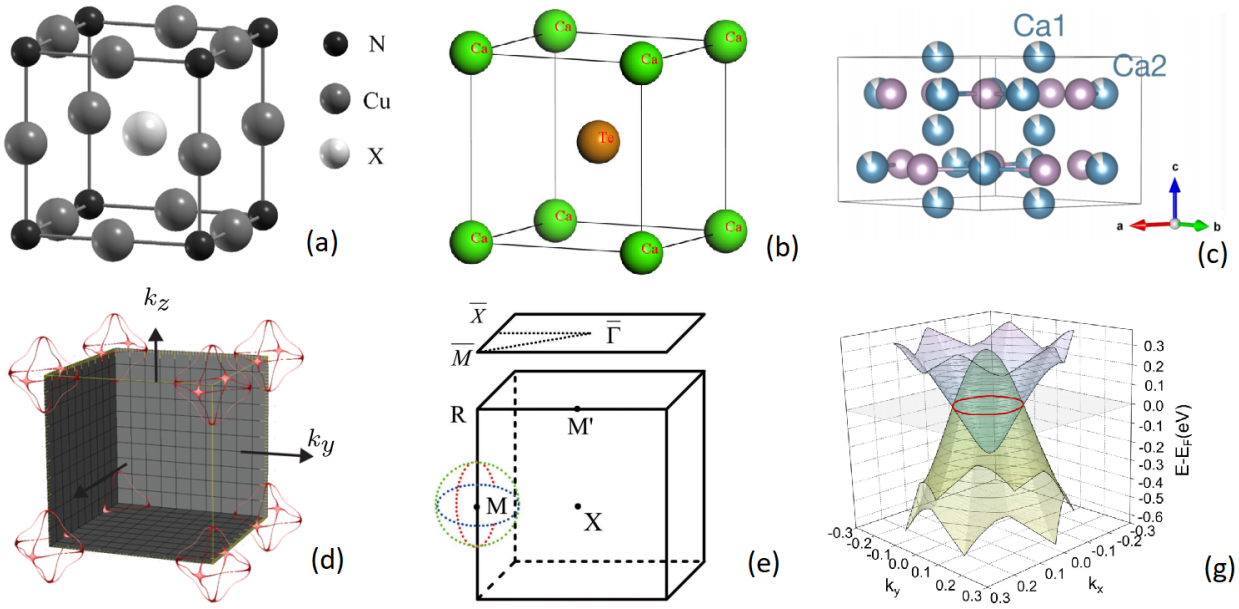

Figure 2.7: The three examples of NLSMs with TR and I symmetry, (a) Cu_3NPd [54], (b) CaTe [59], (c) Ca_3P_2 [73]. Their node lines in the Brillouin zone are illustrated in (d), (e), and (g) respectively.

group $P6_3/mcm$ No. 193 [66, 67]. The crystal structure of Ca_3P_2 with planar view is shown in Fig 2.7b. It shows a fourfold degenerate nodal ring on $k_z = 0$ plane. CaP_3 families have CaP_3, $CaAs_3$, SrP_3, $SrAs_3$, and $BaAs_3$ crystals [68]. When SOC is included, the gaps open along the nodal line and these materials become strong topological insulators for this family. Other than those above, other examples include Alkaline-earth +{stannides, germanides, and silicides} [69], AlB_2-type diborides [70], Mackay-Terrones crystal (MTC) [49], 3D Honeycomb lattice (hyperhoneycomb and stripy-honeycomb lattice) [120]. The $\mathcal{H}$-0 Hyperhoneycom lattice is also the host of quantum anomalous Hall study in chapters 3 and 4. In addition, two-dimensional DNL materials have also been proposed in Cu2Si [71], and in the form of the honeycomb-kagome (HK) lattice [72].

2.3.2.2 NLSMs with Mirror symmetry

PbTaSe2 is a layered, non-centrosymmetric compound in space group P-6m2 No.187 [74]. It can be considered as alternating stacks of TaSe2 and hexagonal Pb layers, with Pb atoms directly sitting above the Se atoms (see Fig 2.8a). It contains a mirror plane passing through the Ta atoms on $k_z = 0$ plane, which plays a role of symmetry plane protecting the topological nodal line. The first two closer to $\bar{K}$ lie on the $k_z = \pi$ plane, while the third one is on the $k_z = 0$ plane (see Fig 2.8c). When the SOC is included, spin degeneracy is lifted due to the lack of I symmetry. Each band splits into two bands with opposite spin polarization and mirror reflection eigenvalues. As a result, four spinful Weyl nodal rings appear from a Dirac nodal ring. Interestingly, SOC also generates a nodal ring which does not exist without SOC, which is called accidental crossing. In addition, this material has spin-momentum locked spin textures which is one of the most prominent characteristics of topological surface states [75].

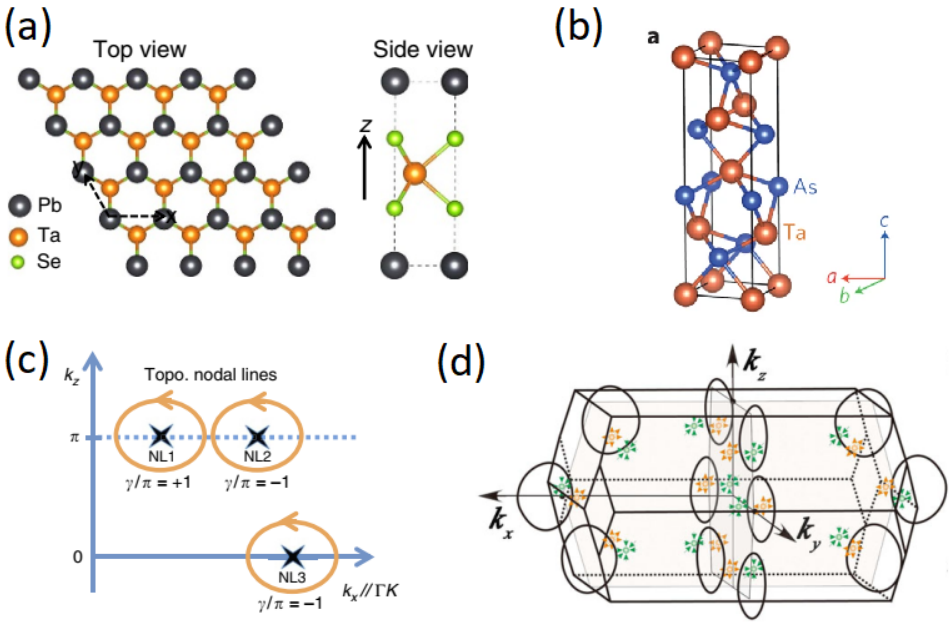

Figure 2.8: The three examples of NLSMs with TR and I symmetry, (a) $PbTaSe_2$ [97] and (b) TaAs [36, 80]. (a) $PbTaSe_2$. The unit cell of $PbTaSe_2$ consists of one Pb, one Ta and two Se atoms, and those atoms appear hexagonal from above. The stacking sequence within the unit cell is Pb-Se-Ta-Se. Schematic of the closed contours encircling the nodal lines coming out of the plane in Brillouin zone (BZ). The Berry's connection is integrated along the arrows and their winding number are shown in (c). (b) shows the crystal structure of TaAs. Node line loops are illustrated as the black circles, and the green and yellow points represent Weyl points with opposite chirality in the First BZ of TaAs (d).

TaAs is in a body-centered tetragonal structure with non-symmorphic space group $I4_1md$ No. 109. Crystal structure of TaAs is shown in Fig 2.8b. It does not have inversion symmetry, and contains two mirror planes (M_x, M_y) and two glide planes (M_{xy}, M_{-xy}). Without SOC, band crossings are protected by mirror symmetry, but not by non-symmorphic mirror operations. The black circles represent nodal line loops in Fig 2.8d. Including SOC, the nodal rings are fully gapped except two pairs of Weyl points. After the theoretical prediction of this Weyl semimetal, the observation of Fermi arcs was made by ARPES [35, 36] and by scanning tunneling microscope (STM) [76, 77]. The WC-type HfC [78] is in hexagonal space group $P\bar{6}m2$ No. 187. It has TR symmetry and two mirror planes, but no I symmetry. Two nodal rings emerge (without SOC) and split into 30 pairs of Weyl points off the mirror plane with SOC. CaAgX (X=P, As) crystallizes in the ZrNiAl-type structure with space group P−62m No. 189 [79]. It has mirror reflection symmetry, but no inversion symmetry.

2.3.2.3 NLSMs with non-symmorphic symmetry

Zr(Hf)SiS is a tetragonal PbFCl-type compound with space group P4/nmm No. 129. 2D Zr(Hf) layer with two S NN layers are sandwiched by Si layers, as shown in fig 2.9. Lattice constant and

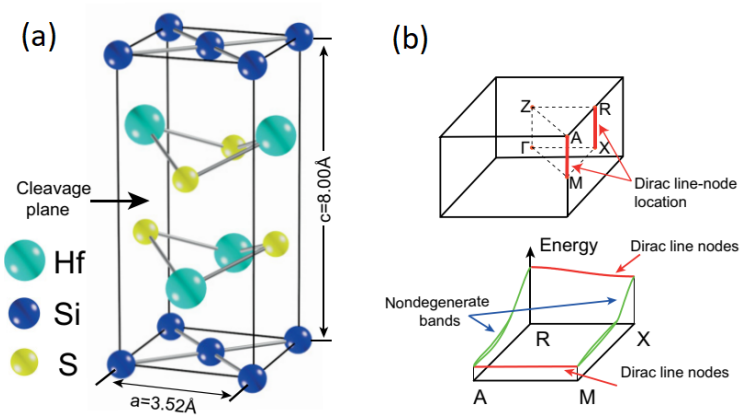

Figure 2.9: Crystal structure of the HfSiS. a) Lattice constant and most probable cleavage plane are indicated. b) Illustration of the Dirac line-node location (upper panel) and the dispersion of the line nodes (lower panel) [85].

most probable cleavage plane is indicated. The Dirac nodal line generated by non-symmorphic symmetry of the square lattice is protected from hybridizing even in the presence of SOC [58] (see Fig 2.9b). ZrSiS and HfSiS are two well-studied examples in the larger ternary material family, which means a compound containing three different elements, WHM, (W=Zr, Hf, or La; H=Si, Ge, Sn, or Sb; M=O, S, Se, and Te) [81–83]. They share the same crystal structure and have topological non-trivial phases.

2.4 Weyl semimetal

The Hamiltonian of a generalized two band model can be expressed by 2×2 matrices in the two component sublattice basis (or other pseudo-spin basis) in the form

$$\mathcal{H}_0(\mathbf{k}) = \epsilon_0(\mathbf{k})\,\sigma_0 + \boldsymbol{h}(\mathbf{k}) \cdot \boldsymbol{\sigma}. \tag{2.14}$$

The crossing of those bands correspond to points in the BZ where the energy dispersion of the quasiparticles $E = \epsilon_0(\mathbf{k}) \pm \sqrt{|\boldsymbol{h}(\mathbf{k})|}$ is zero. In 3D, once we have exhausted all the Pauli matrices, there are no other 2×2 matrices that anticommute with (2.14), and hence the degeneracy at the band crossing is protected against the opening of a gap in that subspace. This simple Hamiltonian has interesting topological properties defined by the flux of Berry curvature around the crossing points, which are known as Weyl points. The monopole of Berry curvature at those points is defined by the helicity of the Weyl fermions, as we explain below. In this section, we go over the history of the Weyl fermion in condensed matter physics and the properties of Weyl semimetals.

2.4.1 Weyl fermion and chirality

Weyl fermions were first proposed in 1929 by Weyl [26] when he suggested the massless Dirac solution can be represented as two combination of Weyl fermions with opposite helicity. Helicity is one of the particles's property that is related to momentum and angular momentum. The free Dirac Hamiltonian can be expressed with γ matrices, where

$$\gamma^0 = \tau_1 \otimes \sigma_0,\ \gamma^i = -i\tau_2 \otimes \sigma_i. \tag{2.15}$$

These matrices satisfy the usual anticommutation relations as in 2+1 dimensional Quantum electrodynamics (QED). The massive Dirac Hamiltonian is $\mathcal{H} = \sum_{i=1,2} \gamma^0 \left(\gamma^i p^i + m\right)$. Then, one can define helicity operator as

$$h_p = \frac{\Sigma \cdot p}{|p|}, \quad \Sigma^i = \frac{1}{2}\epsilon^{ijk}\sigma_{jk}, \quad \sigma_{jk} = \frac{i}{2}\left[\gamma_j, \gamma_k\right]. \tag{2.16}$$

The operator $\frac{1}{2}\Sigma$ satisfies the same commutation relations with angular momentum operators, and the eigenvalues of the helicity operator h_p determine the helicity of the low energy modes. The Hamiltonian commutes with the helicity operator, meaning the quantity is conserved. However, for massive Dirac fermions, the helicity is not invariant under Lorentz boost, which means that different reference frame can observe the helicity of the particle differently. On the other hand, chirality is a Lorentz invariant quantity which is described by the chiral projection. One can define a matrix γ^5which anticommutes with all $\gamma^i$and satisfy $\left(\gamma^5\right)^\dagger = \gamma^5$ and $\left(\gamma^5\right)^2 = 1$. Such γ^5 can be defined as $\gamma^5 = i\gamma^0\gamma^1\gamma^2\gamma^3$. Then, the chiral projection can be defined as

$$L = \frac{1}{2}\left(1 - \gamma^5\right), \quad R = \frac{1}{2}\left(1 + \gamma^5\right) \tag{2.17}$$

where the eigenstate with eigenvalue ± 1 gives left and right chiral modes $L\Psi_L = \Psi_L$ and $R\Psi_R = \Psi_R$ respectively. Interestingly, the difference between helicity and chirality disappear when the particle is massless. Indeed from the eigenvalue equation, $\mathcal{H}\Psi = E\Psi$, then

$$\gamma^0\left(\gamma^i p^i\right)\Psi = p^0\Psi \ \rightarrow\ \left(1 - \gamma^0\frac{(\boldsymbol{\gamma}\cdot\mathbf{p})}{p_0}\right)\Psi = 0. \tag{2.18}$$

In the massless case, $p_0 = |\mathbf{p}|$ for positive energy states. Since $\Sigma_i = -\gamma^0\gamma^i\gamma^5$ [33], then

$$\left(1 - \gamma^5\frac{(\Sigma\cdot\mathbf{p})}{|\mathbf{p}|}\right)\Psi = 0 \ \rightarrow\ \gamma^5\Psi = \frac{(\Sigma\cdot\mathbf{p})}{|\mathbf{p}|}\Psi = h_p\Psi \tag{2.19}$$

with $h_p = \pm 1$.

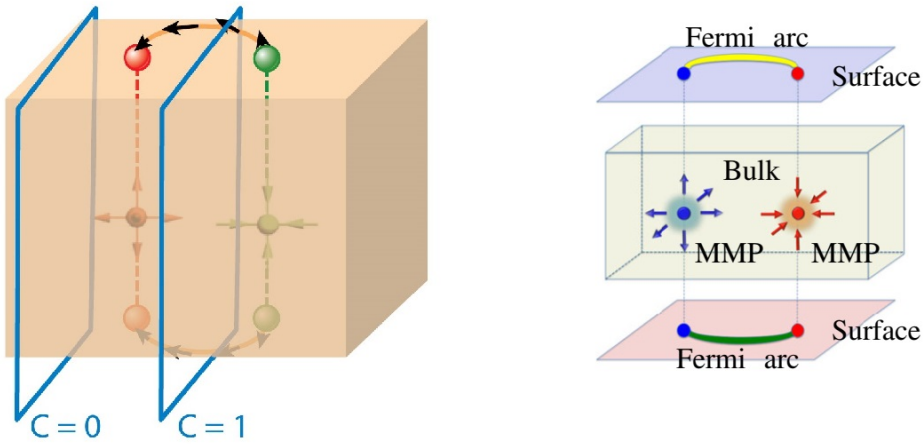

Figure 2.10: (Left) Berry flux passing through a plane is quantized, and the number is known as Chern number. Chern number indicates the edge state of the plane and non-zero when it is placed between two Weyl points. (Right) Bulk and Surface of Weyl semimetals. A Weyl node behaves as a magnetic monopole (MMP) in this system [36][84].

2.4.2 Topological properties of Weyl semimetals

The emergence of Weyl fermions in condensed matter system was theoretically predicted in novel semimetals with non-trivial topology, and first realized in TaAs (Tantalum arsenide) class [34–36]. The simplest model for a Weyl semimetal is a two band Hamiltonian with a linear dispersion around a crossing point is

$$\mathcal{H}_W = \sum_{i=1}^{3} h_i(\mathbf{k})\,\sigma_i. \tag{2.20}$$

This Hamiltonian has energy eigenvalues $\epsilon_\pm = \pm|\boldsymbol{h}(\mathbf{k})|$ and eigenstate $|\psi_\pm\rangle = \frac{1}{|Z|}[h_3(\mathbf{k}) \pm |\boldsymbol{h}(\mathbf{k})|, h_1(\mathbf{k}) - ih_2(\mathbf{k})]$, where $|Z_\pm| = \sqrt{2|\boldsymbol{h}|^2 \pm 2h_3 \cdot |\boldsymbol{h}|}$. Suppose the Weyl point is at $\mathbf{k} = \mathbf{k_0}$ so that $|\boldsymbol{h}(\mathbf{k}_0)| = 0$. From the equation (2.13), the Berry curvature can be found from the Berry connection $A_i = -i\left\langle \psi_- | \frac{\partial}{\partial k_i} | \psi_- \right\rangle$ where we only have one filled band, which is denoted as $(-)$. The configuration of the Berry curvature around the crossing point (Weyl point) determines the chiral charge of the Weyl fermions. The chiral charge or helicity is defined as the source (+ charge) and a sink (- charge) of the Berry curvature in the BZ. In other words, the Berry flux passing through a slice on a given plane of the Brillouin zone (BZ) is quantized by the difference in the chiral (or topological) charges of Weyl points to the left and to the right of the plane (see Fig. 2.10). Since total Berry curvature should be zero inside the BZ according to a 'no-go theorem' [27, 28], Weyl points always appear in pairs with opposite chiral charge [29–32].

The properties of Weyl fermions are interesting for various reasons. The main one is that the system has unique surface states, called Fermi arcs, which are topologically protected. The Fermi arcs connect Weyl points of opposite helicities. The helicity of a Weyl point determines its topological charge. In chapter 2.2.2, we briefly explain the QAH state, which has broken time

reversal symmetry (for spinless fermions). One of the main characteristics of this phase is the presence of robust chiral edge states in the absence of an external magnetic field. The Haldane (Chern) insulator is insulating in the 2D bulk, but has conducting edge channels with quantized Hall conductivity. The Haldane state is characterized by a finite Chern number, a property defined by how the Berry connection of the Block bands winds around the whole BZ [13]. In 3D, we can define the Chern number of the sliced BZ (C), which indicates existence of edge modes intersecting the plane. That number is only non-zero when the plane is located between two Weyl points with different helicities, and the projected surface state has a disconnected line, which is known as the Fermi arc. Since this winding number cannot be changed unless the symmetry of the system is broken, the surface state is also topologically protected. This statement can be clearly seen with the toy model

$$\mathcal{H}(\mathbf{k}) = v_{ij}k_i\sigma_j + m(\mathbf{k})\,\sigma_3. \tag{2.21}$$

The Berry curvature of xy plane is simply

$$\Omega_- = \frac{\partial}{\partial k_1}(A_-)_2 - \frac{\partial}{\partial k_2}(A_-)_1\,, \tag{2.22}$$

and Chern number of the plane is

$$C_{2D} = \frac{1}{2}\mathrm{sign}(m)\,\mathrm{sign}(\det[\mathbf{v}_{2D}])\,. \tag{2.23}$$

Around the Weyl points, the first term of $\mathcal{H}(\mathbf{k})$ remains but $m(\mathbf{k})$ changes the sign (cross zero at the point). The difference of $C_{xy}|_{k_z=+0}$ and $C_{xy}|_{k_z=-0}$ gives $+1$ or -1 depends on it's a source $(+1)$ or a sink (-1) of Berry curvature. Since the gradient of the third Pauli matrix corresponds to the velocity of z direction in this model, the number corresponds to the $\det[\mathbf{v}_{3D}]$ which is exactly chirality of the Weyl fermion.

In general, either the inversion symmetry [86] and time reversal symmetry [87] should be broken for Weyl points to form. Provided a Weyl point exists, time reversal symmetry requires the existence of a pair of Weyl points with opposite momenta with respect to the center of the BZ have the *same* helicity. Therefore, Weyl semimetals with $\mathcal{T}$ require at least four Weyl points in the BZ for the total chiral charge to be zero. On the other hand, inversion symmetry requires a pair of Weyl points with opposite helicity, so the minimum number of the Weyl point is two. (see Fig 2.11.) If both symmetries are preserved, two Weyl points with opposite helicity must merge and a four band degeneracy will occur at a Dirac point. Dirac points in 3D cannot be reduced into Weyl representation and are described by a larger representation (Dirac matrices) as in a three-dimensional Dirac semimetals (DSMs) [88–90].

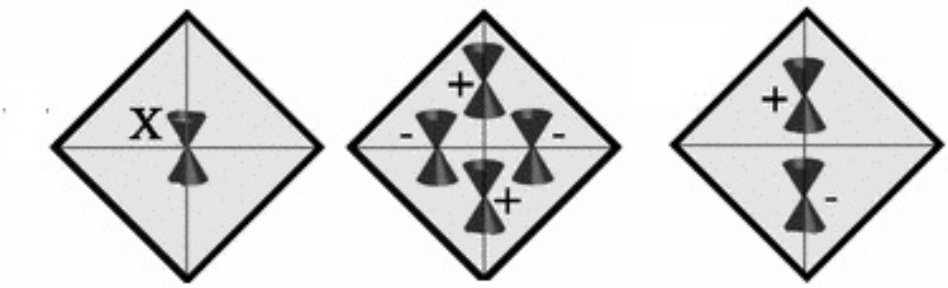

Figure 2.11: Schematic picture of Weyl semimetal (WSM) and Dirac semimetal (DSM). When $\mathcal{T}$ and $\mathcal{P}$ symmetry are both present, Dirac cone don't carry chiral charge (left). If $\mathcal{P}$ symmetry is broken, two Weyl points on the opposite site has the same chiral charge (center). On the other hands, $\mathcal{T}$ broken WSM has opposite chiral charge (right). The chiral charge of each Weyl point is illustrated by $\pm$ sign [88].

Chapter 3

Quantum Anomalous Hall effect

The Hall conductivity is the coefficient of the transverse Hall current, which flows in a perpendicular direction to the applied electric field. The Hall current can be observed in a 2D conducting plate when a perpendicular magnetic field is applied on the plate. In the quantum limit, in the presence of Landau levels, the quantum Hall conductivity describes dissipationless transport of electrons in a system that breaks time reversal symmetry (TRS) due to an external applied magnetic field. In two dimensions (2D), the current is carried through the edges [91], and the Hall conductivity σ_{xy} is quantized in units of e^2/h. In three dimensions (3D), the Hall conductivity is not universal and has an extra unit of inverse length. As shown by Halperin [110], the 3D conductivity tensor on a lattice has the form $\sigma_{ij} = e^2/(2\pi h)\epsilon_{ijk}G_k$, where G is a reciprocal lattice vector (it could be zero). The realization of the 3D quantum Hall effect has been proposed in systems with very anisotropic Fermi surfaces [116–118], or else in node-line semimetals [92, 112, 120, 122], where the Fermi surface has the form of a line of Dirac nodes [49, 54, 56, 66, 93, 95–99, 123–126, 144].

Equally interesting would be to realize the 3D quantum anomalous Hall (QAH) effect [32, 101–103], where the anomalous Hall conductivity emerges from the topology of the 3D band structure in the absence of Landau levels. The first proposal for a Chern insulator system was the Haldane model [14] on the honeycomb lattice, where loop currents break TRS and can produce a non-zero Chern number in the bulk states. Hyperhoneycomb lattices have the same planar trigonal connectivity of the honeycomb lattice (see Fig. 1a), and hence could provide a natural system for the emergence of a 3D QAH conductivity. While we are not aware of a concrete example of a material that realizes this lattice, this geometry has been realized in honeycomb iridates as a spin lattice [142]. The metallic version of it, which is a nodal-line semimetal, requires s-wave orbitals and may in principle be realized in optical lattices with cold atoms. Very recently, the Haldane model was simulated with cold atoms [143] and in quantum circuits [150].

In this chapter, we describe the 3D QAH state that emerges from repulsive interactions in a hyperhoneycomb lattice with spinless fermions. This state competes with a CDW state, and produces a very anisotropic gap around a line of Dirac nodes in the semimetallic state. Due to a broken inversion and time reversal symmetry, the QAH gap changes sign along the nodal line, forming Weyl points connected by Fermi arcs [20, 30]. We show that the QAH conductivity of the

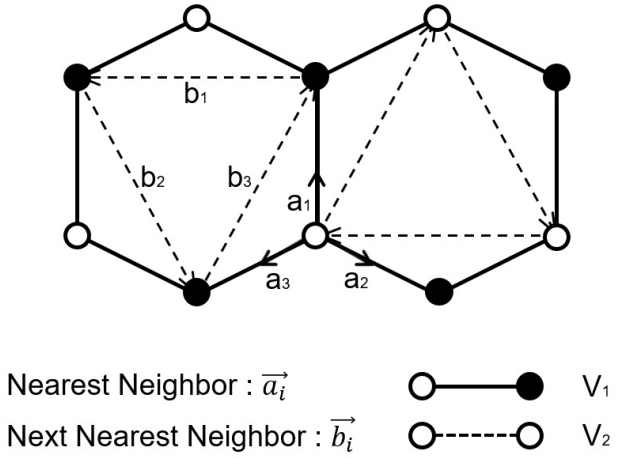

Figure 3.1: Honeycomb lattice with nearest neighbor (NN) interaction V_1 and next nearest neighbor (NNN) interaction V_2. Two sublattice are illustrated as empty and solid dots. Dashed arrows indicates NNN vectors [15]. The local flux enclosed by the loop is determined by total phase of NNN transitions.

surface states is $e^2/\sqrt{3}ah$, with a the lattice constant.

3.1 2D Quantum Anomalous Hall effect

As briefly mentioned in section 2.2.2, the Haldane mass can be introduced by the complex hopping amplitude for next-nearest neighbor (NNN) sites in the honeycomb lattice. The idea is that those phases produce loop currents in the unit cell, as shown in Fig. 3.1, which nevertheless do not create a net magnetic flux. Repulsive interactions (possibly Coulomb interaction) can also effectively induce NNN hopping. In mean field approximation, Raghu et al. [15] proposed an effective effective model for graphene with possible topological phases induced by repulsive interactions. We briefly describe that model below.

The Hamiltonian with a nearest neighbor (NN) interaction (V_1) and NNN interaction (V_2) is

$$\mathcal{H}_{\text{tot}}(\mathbf{R}) = H_0(\mathbf{R}) + H_1(\mathbf{R}) + H_2(\mathbf{R}) \tag{3.1}$$

$$\mathcal{H}_0(\mathbf{R}) = -t \sum_{\langle i,j \rangle} \left(a_i^\dagger b_j + b_j^\dagger a_i \right) \tag{3.2}$$

$$\mathcal{H}_1(\mathbf{R}) = V_1 \sum_{\langle i,j \rangle} a_i^\dagger a_i b_j^\dagger b_j \tag{3.3}$$

$$\mathcal{H}_2(\mathbf{R}) = V_2 \left(\sum_{\langle\langle i,j \rangle\rangle} a_i^\dagger a_i a_j^\dagger a_j + \sum_{\langle\langle i,j \rangle\rangle} b_i^\dagger b_i b_j^\dagger b_j \right) \tag{3.4}$$

where a and b are fermionic annihilation operators in sublattice A and B, $\langle i,j\rangle$ indicates nearest neighbor (NN) sites, while $\langle\langle i,j\rangle\rangle$ means NNN sites. As in the Haldane model, spin degrees of freedom are suppressed to avoid the fermionic doubling problem [14], which hinders topological phases. In mean-field approximation, the four-fermion operator terms can be expressed as

$$a_i^\dagger a_i b_j^\dagger b_j = a_i^\dagger a_i b_j^\dagger b_j = \left\langle a_i^\dagger a_i \right\rangle b_j^\dagger b_j + a_i^\dagger a_i \left\langle b_j^\dagger b_j \right\rangle - \left\langle a_i^\dagger a_i \right\rangle \left\langle b_j^\dagger b_j \right\rangle \tag{3.5}$$

$$\begin{aligned} a_i^\dagger a_i a_j^\dagger a_j &= a_i^\dagger a_i \left(1 - a_j a_j^\dagger\right) = a_i^\dagger a_i + a_i^\dagger a_j a_i a_j^\dagger \\ &= a_i^\dagger a_i + \left\langle a_i^\dagger a_j \right\rangle a_i a_j^\dagger + a_i^\dagger a_j \left\langle a_i a_j^\dagger \right\rangle \\ &= a_i^\dagger a_i + \left\langle a_i^\dagger a_j \right\rangle a_i a_j^\dagger + \left\langle a_i a_j^\dagger \right\rangle^* a_i^\dagger a_j. \end{aligned} \tag{3.6}$$

Each expectation value is related to an order parameter associated to a physical observable. For instance, $\left\langle a_i^\dagger a_i \right\rangle$ is the charge density on sublattice A (ρ_A) and $\left\langle b_i^\dagger b_i \right\rangle$ on sublattice B (ρ_B). $\left\langle a_i^\dagger a_j \right\rangle$ is the NNN transition amplitude with a complex phase (complex value, χ_{ij}). If the order parameters are spatially independent then the Fourier transformation of the Hamiltonian has the form

$$\begin{aligned} \mathcal{H}_{MF}(\mathbf{k}) = &- \sum_{\mathbf{k}} \epsilon_{\mathbf{k}} e^{-i\theta_k} c_A^\dagger c_B - \sum_k \epsilon_{\mathbf{k}} e^{i\theta_k} c_B^\dagger c_A - 3V_1\rho \left(c_A^\dagger c_A - c_B^\dagger c_B\right) + 3V_1 N\rho^2 \\ &- 2V_2 |\chi| \sum_{\mathbf{k}} \sum_{\mathbf{b}_n} \left(\cos(\mathbf{k}\cdot\mathbf{b}_n - \phi)\, c_A^\dagger c_A + \cos(\mathbf{k}\cdot\mathbf{b}_n + \phi)\, c_B^\dagger c_B\right) + 6V_2 N |\chi|^2 \end{aligned} \tag{3.7}$$

where we defined order parameter ρ for charge density wave (CDW) state as

$$\rho = \frac{1}{2}(\rho_A - \rho_B), \text{ simply use } \rho_A = \rho,\ \rho_B = -\rho, \tag{3.8}$$

and QAH order parameter χ_{ij} as

$$\chi_{ij} = \begin{cases} |\chi| e^{i\phi} & \text{for } \left\langle a_i^\dagger a_j \right\rangle \text{ in the same direction with Fig3.1} \\ |\chi| e^{-i\phi} & \text{for } \left\langle b_i^\dagger b_j \right\rangle \text{ in the same direction with Fig3.1} \end{cases}. \tag{3.9}$$

$\epsilon_{\mathbf{k}}$ is the kinetic energy of the non-interacting system. As a result, at zero chemical potential, $\cos(\mathbf{k}\cdot\mathbf{b}_n)\cos(\phi)$ breaks particle-hole symmetry (shift cone) and $\sin(\mathbf{k}\cdot\mathbf{b}_n)\sin(\phi)$ breaks time-reversal symmetry. If we impose conservation of particle-hole symmetry, $\phi = \pm\frac{\pi}{2}$, what enforces χ_{ij} to be purely imaginary. At zero temperature and half filling, the mean-field free energy is readily obtained:

$$F = -\sum_{\mathbf{k}} \sqrt{\epsilon_{\mathbf{k}}^2 + \left(3V_1\rho + 2V_2|\chi| \sum_{\mathbf{b}_n} \sin(\mathbf{k}\cdot\mathbf{b}_n)\sin\phi\right)^2} + 3V_1 N\rho^2 + 6V_2 N|\chi|^2. \tag{3.10}$$

The value $\phi = \pm\frac{\pi}{2}$ can also also be verified to minimize the free energy with respect to ϕ.

To check for any instabilities in the charge and topological channels, we minimize the free energy with respect to ρ and $|\chi|$. The minimization results in the set of self-consistent equations

$$\rho = \frac{1}{6N}\sum_{\mathbf{k}} \frac{V_1\rho + 2V_2\chi\sum_{\mathbf{b}_n}\sin\left(\mathbf{k}\cdot\mathbf{b}_n\right)}{\sqrt{\epsilon_{\mathbf{k}}^2 + \left(3V_1\rho + 2V_2\left|\chi\right|\sum_{\mathbf{b}_n}\sin\left(\mathbf{k}\cdot\mathbf{b}_n\right)\sin\phi\right)^2}}, \tag{3.11}$$

and

$$\chi = \frac{1}{6N}\sum_{\mathbf{k}} \frac{\left(\sum_{\mathbf{b}_n}\sin\left(\mathbf{k}\cdot\mathbf{b}_n\right)\right)\left(V_1\rho + 2V_2\chi\sum_{\mathbf{b}_n}\sin\left(\mathbf{k}\cdot\mathbf{b}_n\right)\right)}{\sqrt{\epsilon_{\mathbf{k}}^2 + \left(3V_1\rho + 2V_2\left|\chi\right|\sum_{\mathbf{b}_n}\sin\left(\mathbf{k}\cdot\mathbf{b}_n\right)\sin\phi\right)^2}}. \tag{3.12}$$

For graphene, the phase diagram is shown in Fig 3.2. When both ρ and $|\chi|$ are zero, the system is a semimetal with two Dirac point $K_\pm$. The CDW state ($\rho \neq 0$) corresponds to an ordinary insulator with fully gapped Dirac points. The QAH state ($\chi \neq 0$) of this model has the same configuration with spontaneous parity and $\mathcal{T}$ symmetry breaking in a honeycomb lattice with spinless fermions. Also, the energy gap at the Dirac points are

$$E_{\text{gap}} = 4\left|V_2\chi\sum_{\mathbf{b}_n}\sin\left(K_\pm\cdot\mathbf{b}_n\right)\right| = 2\sqrt{3}V_2\left|\chi\right|. \tag{3.13}$$

Hence, it has insulating bulk state. However, since it breaks both inversion and time reversal symmetry, it has Chern number[2] 1. In 2D space, the Hall conductance is exactly given by Chern number of the lower band times e^2/h (see Appendix A). Therefore,

$$\sigma_{xy} = \frac{e^2}{h}, \tag{3.14}$$

reflecting the spontaneous emergence of chiral conducting edge states. Such state of matter is known as the Chern (or Mott) insulator.

3.2 3D QAH transition for NLSMs

The hyperhoneycomb lattice is 3D structure with planar trigonal bonds spaced by 120°. Although this lattice is 3D, it has the same planar trigonal connectivity of graphene (see Fig 3.3). The structure shown in Fig. 3.3a has a screw symmetry along the z axis, giving rise to a nodal line (red) in the $k_z = 0$ plane of the BZ shown in fig. 3.3b. In the QAH phase, one can geometrically construct four types of current loops which have local flux inside, but overall net zero flux in the 3D unit cell. Two of them are located on xz plane and the other two are on yz plane (see Fig 3.4).

We start from the tight binding model of the hyperhoneycomb lattice, which has four atoms per unit cell, as shown in Fig. 3.3a. The lattice has three vector generators $\mathbf{a}_1 = (\sqrt{3}, 0, 0)$,

[2]Both Dirac points sitting at K and $-K$ have the Chern number $\nu = \frac{1}{2}$. Thus, the total Chern number adds up to 1.

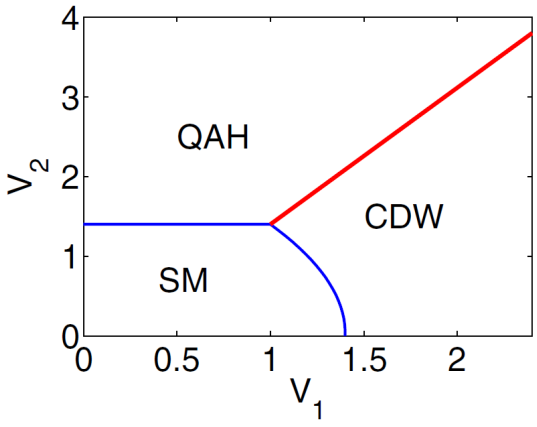

Figure 3.2: Phase diagram of graphene with spinless fermions. Energy scale is $t = 1$ where t is the transition amplitude introduced at (3.1). The transition from semimetallic (SM) state to CDW and QAH states are a continuous transition. The boundary of QAH and CDW is identified as a first-order transition [15].

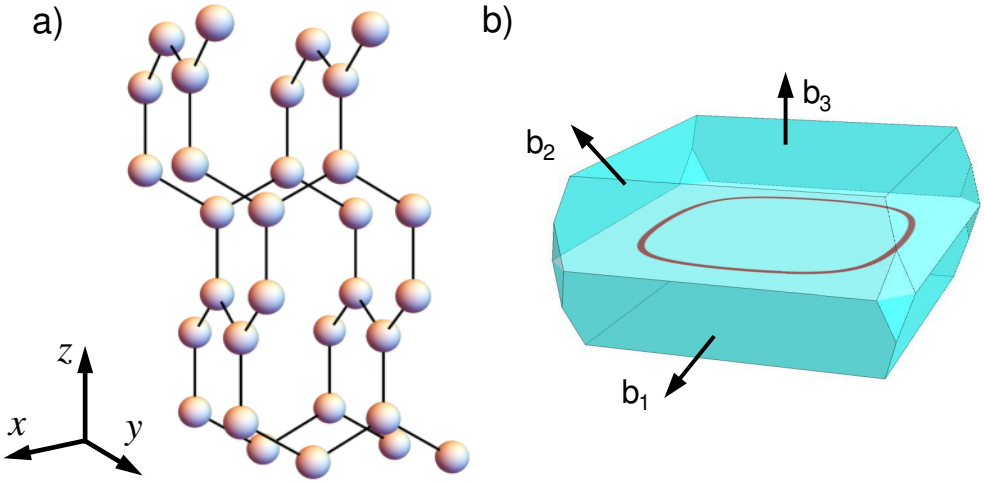

Figure 3.3: (a) Hyperhoneycomb lattice with four sublattice, depicted as colored spheres. All sites are trigonally connected in plane with nearest neighbor sites by 120°. The connections are spanned on two planes which are rotated by 90° one another. (b) 3D Brillouin zone (BZ) of the crystal. In the semimetallic state, closed band gap line (Dirac node) is shown in the red curve on the $k_z = 0$ plane. The black arrows indicate the reciprocal lattice vectors [105, 106].

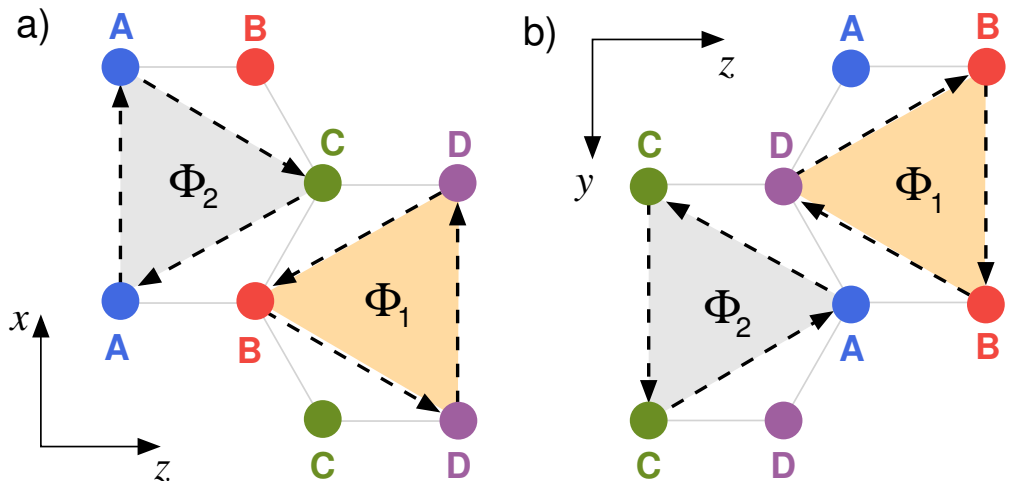

Figure 3.4: xz (a) and yz (b) planes of the HHC lattice with sublattice A, B, C, and D. Complex NNN hoping amplitude give the local flux Φ and breaks time reversal symmetry. Total flux in the unit cell is zero due to the geometry of the lattice [105].

$\mathbf{a}_2 = (0, \sqrt{3}, 0)$ and $\mathbf{a}_3 = (-\sqrt{3}/2, \sqrt{3}/2, 3)$, and the corresponding reciprocal lattice vectors $\mathbf{b}_1 = (2\pi/\sqrt{3}, 0, -\pi/3)$, $\mathbf{b}_2 = (0, -2\pi/\sqrt{3}, \pi/3)$ and $\mathbf{b}_3 = (0, 0, 2\pi/3)$. For a model of spinless fermions, which could physically result from a strong Rashba spin orbit coupling [16], the kinetic energy is $\mathcal{H}_0 = -t\sum_{\langle i,j\rangle}(a_i^\dagger a_j + h.c.)$, where a_i destroys an electron on site i, t is the hopping energy and $\langle ij\rangle$ denotes nearest neighbor (NN) sites. In the four-sublattice basis, the Hamiltonian is a 4×4 matrix [120].

$$\mathcal{H}_0 = -t \begin{pmatrix} 0 & \Theta_x & 0 & \mathrm{e}^{-ik_z} \\ \Theta_x^* & 0 & \mathrm{e}^{ik_z} & 0 \\ 0 & \mathrm{e}^{-ik_z} & 0 & \Theta_y \\ \mathrm{e}^{ik_z} & 0 & \Theta_y^* & 0 \end{pmatrix}, \tag{3.15}$$

where $\Theta_\gamma \equiv 2\mathrm{e}^{ik_z/2}\cos(\sqrt{3}k_\gamma/2)$, with $\gamma = x$, y, and $\mathbf{k}$ is the momentum away from the center of the Brillouin zone (BZ). The electronic structure has a doubly degenerate zero energy line of nodes in the form of a Dirac loop at the $k_z = 0$ plane, $\mathbf{k}_0(s) \equiv (k_x(s), k_y(s), 0)$ in some parametrization that satisfies the equation $4\cos(\sqrt{3}k_x(s)/2)\cos(\sqrt{3}k_y(s)/2) = 1$, as schematically depicted in Fig. 3.3b.

Consider the interaction between NN and NNN sites (V_1 and V_2 respectively). For spinless fermions, one possible instability is a charge density wave (CDW) state that corresponds to a charge imbalance among the different sublattices. The CDW state is defined by the four component order parameter $\rho_\alpha = \langle a_i^\dagger a_i\rangle - \rho_0$ with $i \in \alpha$ belonging to sublattice $\alpha = A, B, C, D$, as shown in Fig 3.4, and ρ_0 a uniform density. At the neutrality point, the local densities at the four sites of the unit cell add up to zero, $\sum_\alpha \rho_\alpha = 0$. The nodal line is protected by a combination of TRS and mirror symmetry along the z axis. The state where $\rho_A = -\rho_B = \rho_C = -\rho_D$, namely $(\rho, -\rho, \rho, -\rho)$, breaks the mirror symmetry and opens the largest gap among all possible charge neutral configurations of ρ_α. The more symmetric state $(\rho, \rho, -\rho, -\rho)$ does not open a gap. Hence, the former state is the

dominant CDW instability. We will not consider other possible states that enlarge the size of the unit cell [107], such as an n-site CDW state, with $n > 4$.

The other dominant instability is the QAH state, where complex hopping terms between NNN sites lead to loop currents in the xz and yz planes, as shown in Fig. 2. Each plane can have loop currents with opposite flux (Φ), producing zero magnetic flux in the unit cell, in analogy with the 2D case in the honeycomb lattice [14]. The QAH order parameter is defined as $\chi_{ij} = \langle a_i^\dagger a_j \rangle$, where i and j sites are connected by NNN vectors [15]. We define the Ansatz $\chi_{ij} = \chi e^{i\phi_{ij}}$ for i, $j \in \{A, C\}$ sublattices and $\chi_{ij} = \chi e^{i\bar{\phi}_{ij}}$ for i, $j \in \{B, D\}$, where χ is real. Due to particle-hole symmetry, χ_{ij} is purely imaginary and hence $\phi, \bar{\phi} = \pm\frac{\pi}{2}$. The state that minimizes the free energy of the system has $\phi = -\bar{\phi}$. The QAH order parameter is $\chi_{ij} = \pm i\chi$ for NNN sites and zero otherwise, with the $+$ for A,C and $-$ for B,D following the convention of the arrows in Fig. 3.4.

We perform a mean-field decomposition of the NN interaction in the CDW state (ρ) and of the NNN repulsion in the QAH order parameter χ_{ij}. For simplicity, we absorb the couplings V_1 and V_2 in the definition of the order parameters, $\rho V_1 \to \rho$ and $\chi V_2 \to \chi$, which have units of energy from now on. The effective interaction in the four-sublattice basis is

$$H_I^{\mathrm{MF}} = \begin{pmatrix} \chi g - 3\rho & 0 & -\chi f & 0 \\ 0 & -\chi g + 3\rho & 0 & \chi f^* \\ -\chi f^* & 0 & \chi g - 3\rho & 0 \\ 0 & \chi f & 0 & -\chi g + 3\rho \end{pmatrix} \tag{3.16}$$

where

$$g(\mathbf{k}) \equiv 2\left[\sin\left(\sqrt{3}k_x/2\right) + \sin\left(\sqrt{3}k_y/2\right)\right] \tag{3.17}$$

$$f(\mathbf{k}) \equiv 2\left[e^{3ik_z/2}\sin\left(\sqrt{3}k_x/2\right) + e^{-3ik_z/2}\sin\left(\sqrt{3}k_y/2\right)\right] \tag{3.18}$$

as shown in Appendix B. The mean-field Hamiltonian $\mathcal{H}^{\mathrm{MF}} = \mathcal{H}_0 + \mathcal{H}_I^{\mathrm{MF}}$ has an additional constant energy term $E_0 = 6\rho^2/V_1 + 16\chi^2/V_2$ that is reminiscent of the decomposition of the interactions to quadratic form. The phase diagram follows from the numerical minimization of the free energy F with respect to ρ and χ at zero temperature, $\partial F/\partial\chi = \partial F/\rho = 0$. The semimetal state is unstable to a CDW order at the critical coupling $V_{1,c} = 0.41t$, and to a QAH phase at $V_{2,c} = 1.51t$. The CDW and QAH states compete with each other, as shown in Fig. 3.5. Fluctuation effects are expected to be less dramatic in 3D compared to the more conventional 2D case [15, 108, 109]. Hence, the mean-field phase diagram is likely a reliable indication of the true instabilities of the fermionic lattice for the spinless case.

In real crystals, screening and elastic effects lead to a distortion of the lattice in the CDW state, in order to minimize the Coulomb energy due to electron-ion coupling, which can be high [111]. While the CDW appears to be the leading instability over the QAH state, the elastic energy cost to displace the ions and equilibrate the charge in the electron-ion system may hinder the CDW order and favor the QAH phase when $V_2 > V_{2,c}$.

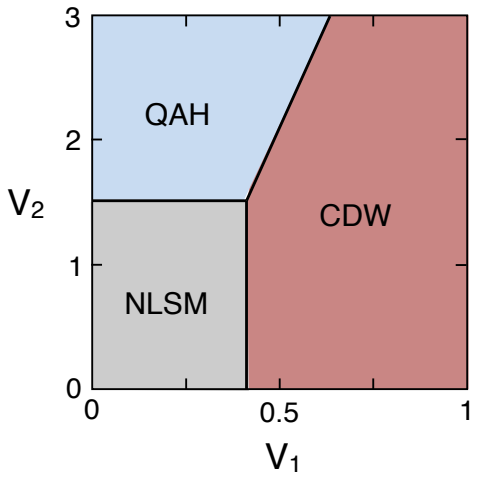

Figure 3.5: Mean field phase diagram for spinless fermions in HHC. The node-line semimetal phase (NLSM) turns into the CDW state at the critical value $V_1 = 0.41t$ and into the QAH phase in 3D at $V_2 = 1.51t$. The CDW is fully gapped, while the QAH phase has nodes around the Dirac loop [105].

Recall the Hamiltonian (3.16). Without Coulomb interaction ($V_1\rho = 0$, $V_2\chi = 0$), one can find a line of nodes in the Brillouin zone (red curve in Fig 3.3), which has linear dispersion to the radial and k_z direction. The low-energy excitation around the line can be described as projected Hamiltonian around the points on the line, which has a form of

$$H_0^P(s, \mathbf{q}) = \left[v_x(s) q_x + v_y(s) q_y\right] \sigma_x + v_z(s) q_z \sigma_y, \tag{3.19}$$

where $\mathbf{q}$ is the relative momentum from the node line, and

$$v_x(s) = \frac{\sqrt{3}}{2} t \sin\left[\frac{\sqrt{3}}{2} k_x(s)\right] \frac{1}{1+\kappa^2(s)} \tag{3.20}$$

$$v_y(s) = \frac{\sqrt{3}}{2} t \sin\left[\frac{\sqrt{3}}{2} k_y(s)\right] \frac{\kappa^2(s)}{1+\kappa^2(s)} \tag{3.21}$$

$$v_z(s) = -3t \frac{\kappa(s)}{1+\kappa^2(s)} \tag{3.22}$$

where $\kappa(s) = 2\cos\left[\sqrt{3} k_x(s)/2\right]$. Integrating out the two high energy bands using perturbation theory, the effective low energy Hamiltonian (3.19) of the nodal line becomes massive, as expected. The leading correction to Hamiltonian (3.19) around the nodal line to lowest order in ρ and χ has the form of a mass term

$$H_I^P(s, \mathbf{q}) = -\left[m(s) + v_x' q_x + v_y' q_y\right] \sigma_3, \tag{3.23}$$

where

$$m\left(\mathbf{k_0}\right) = \chi\left(g\left(\mathbf{k_0}\right) + \frac{2}{\alpha + \frac{1}{\alpha}} f\left(\mathbf{k_0}\right)\right) \tag{3.24}$$

$$v'_{\alpha=x,y}\left(\mathbf{k}_0\right) = 2\chi\left[\cos\left(\sqrt{3}\left(\mathbf{k_0}\right)_\alpha\right) + \frac{1}{\alpha + \frac{1}{\alpha}}\cos\left(\frac{\sqrt{3}}{2}\left(\mathbf{k_0}\right)_\alpha\right)\right] \tag{3.25}$$

$$\alpha\left(\mathbf{k}_0\right) = 2\cos\left(\frac{\sqrt{3}}{2}\left(\mathbf{k_0}\right)_x\right). \tag{3.26}$$

The low energy spectrum is

$$\epsilon(\mathbf{q}) = \pm\sqrt{\epsilon_0^2(\mathbf{q}) + \left[3\rho + m(\mathbf{k}_0) + v'_x q_x + v'_y q_y\right]^2}, \tag{3.27}$$

which describes either a uniformly gapped state in the CDW phase ($\rho \neq 0$, $\chi = 0$) or a non-uniform QAH gap ($\rho = 0, \chi \neq 0$) with six nodes at the zeros of $m(\mathbf{k}_0)$, as indicated in Fig. 3.6. The CDW state breaks mirror symmetry along the z axis, but preserves the screw axis symmetry and hence creates a fully gapped state that is rotationally symmetric along the nodal line. The QAH state, on the order hand, breaks TR symmetry. The mass term (3.24) changes sign at six zeros along the nodal line, as shown in Fig. 3.6b. Two zeros are located along the diagonal direction of the nodal line, at the points $\pm\mathbf{Q}_1 = \pm\left(\frac{2\pi}{3\sqrt{3}}, -\frac{2\pi}{3\sqrt{3}}, 0\right)$. The other four zeros of $m(\mathbf{k}_0)$ are symmetrically located around that direction, at $\pm\mathbf{Q}_2 = \mp(Q_+, Q_-, 0)$ and $\pm\mathbf{Q}_3 = \pm(Q_-, Q_+, 0)$, as shown in Fig. 4, with

$$Q_\pm = \frac{1}{\sqrt{3}}\arccos(\frac{\sqrt{17}-1}{4}) \pm \frac{1}{\sqrt{3}}\arccos(\frac{3-\sqrt{17}}{4}). \tag{3.28}$$

The position of the nodal points extracted from the low energy Hamiltonian (3.23) is in agreement with the values calculated numerically from Hamiltonians (3.15) and (3.16) in the regime where $\chi \ll t$. For larger values of χ, the nodal points $\pm\mathbf{Q}_2$ and $\pm\mathbf{Q}_3$ can move in the $k_z = 0$ plane, as the position of the nodal line is renormalized by the interactions. The two nodal points in the diagonal $\pm\mathbf{Q}_1$ remain fixed.

3.2.1 Weyl fermions and topological surface states

Expanding the mass term (3.24) around the zeros of $m(\mathbf{k}_0)$, the low energy quasiparticles around the nodes are Weyl fermions. Performing a rotation of the quasiparticle momenta into a new basis $p_x = (q_x - q_y)/\sqrt{2}$, $p_y = -q_z$ and $p_z = (q_x + q_y)/\sqrt{2}$, the expansion around the nodes at $\pm\mathbf{Q}_1$ gives the low energy Hamiltonian

$$\mathcal{H}_{\pm Q_1}(\mathbf{p}) = \mathbf{h}_{\pm Q_1}(\mathbf{p}) \cdot \vec{\sigma} = \sum_{i=x,y,z} v_{0,i}^{(\pm)} p_i \sigma_i, \tag{3.29}$$

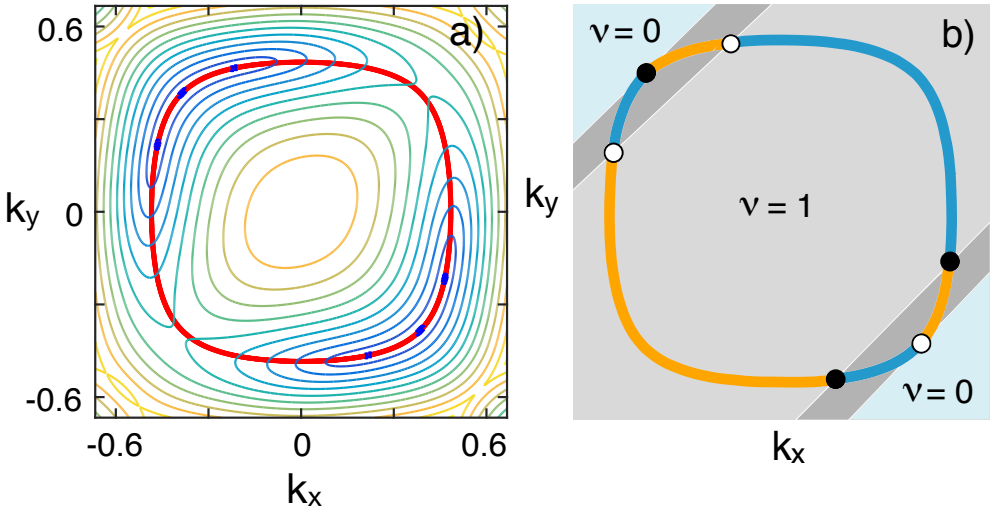

Figure 3.6: (a) Contour plot of the mass gap of the QAH state. Node-line is depicted as a red line. Momenta are in units of π/a where a in an interatomic length of HHC lattice. The mass gap vanishes at six points along the node line indicated by the blue dots. (b) Schematic picture of the sign of the mass term along the node line: blue ($m > 0$), orange ($m < 0$). At six ($m = 0$) points, the low-energy excitations are Weyl fermions with helicities $+1$ (white dots) and -1 (black dots). The planes intersecting the points separate the domain of planes with distinct 2D Chern numbers: Gray area has $C_{2D} = 1$, and Dark gray has $C_{2D} = -1$ [105].

with $\mathbf{p}$ the momentum away from the nodes and $v_{0,x}^{(\pm)} = \pm 3\sqrt{2}t/4$, $v_{0,y} = 3t/2$ and $v_{0,z} = \sqrt{3/2}\chi$ the corresponding velocities in the rotated basis. The equation above describes two Weyl points with opposite helicities $\gamma = (2\pi)^{-2} \int_\Omega \mathrm{d}^2 p\, \hat{h} \cdot (\partial_{p_x} \hat{h} \times \partial_{p_y} \hat{h}) = \pm 1$, and hence broken TRS, with $\hat{h} = \mathbf{h}/|\mathbf{h}|$ a unitary vector and Ω the surface of a small sphere enclosing each node. Similarly, the expansion around the nodes $\pm\mathbf{Q}_2$ and $\pm\mathbf{Q}_3$ give Hamiltonians of Weyl fermions with helicities ± 1, as indicated in Fig. 3.6.

The Weyl points delimit a topological domain wall between slices of the BZ parallel to the $(1\bar{1}0)$ plane. Each slice in the light gray region in Fig. 3.6 crosses the nodal line twice and has a well defined Chern number $\nu = +1$. The slices in the dark gray regions across the domain walls have opposite Chern number $\nu = -1$, as the QAH mass changes sign simultaneously at the two Weyl points (with the same helicity) where each domain wall intersects the nodal line. The BZ slices in the light blue region do not cross the nodal line and have zero Chern number.

The 3D QAH conductivity is defined as $\sigma_{ij} = (e^2/h)(2\pi)^{-3} \int_{BZ} \mathrm{d}^3 k \sum_{n\in\text{filled}} (\frac{\partial}{\partial k_i} A_j - \frac{\partial}{\partial k_j} A_i)$, where $A_j = -i \langle \psi_n | \frac{\partial}{\partial k_j} | \psi_n \rangle$ is the Berry connection of the n-th occupied Block band integrated over the entire BZ [149]. As mentioned before, a 2D slice of BZ has analogous features of a 2D Chern insulator. From the Kubo formula for 3D Hall conductivity [110]

$$\sigma_{ij} = \frac{e^2}{2\pi^2 h} \int d^3k \sum_{n\in\text{filled}} \mathrm{Im} \int d^3 r \frac{\partial u^*_{\mathbf{k},n}}{\partial k_i} \frac{\partial u_{\mathbf{k},n}}{\partial k_i} \tag{3.30}$$

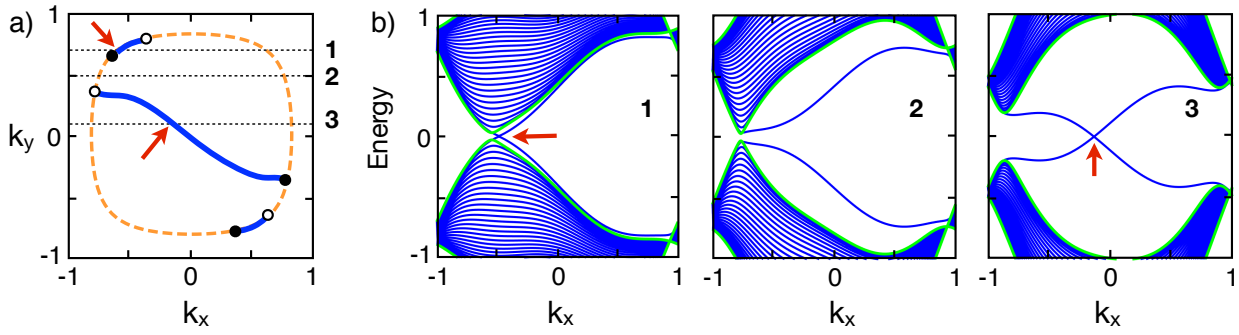

Figure 3.7: (a) Fermi arcs on the (001) surface of BZ indicated by the blue solid lines. The dashes represent the projection of the node-line in the bulk in the absence of interactions. Weyl points and their chirality are illustrated as black (-1) and white dots (+1). (b) Panels showing the energy bands along three momentum slices labeled 1, 2, 3 in (a). All momenta are in units of $\pi/\sqrt{3}$, and energy has units of the hopping energy t. Slice 1 and 3 which are intersecting with Fermi arc have zero energy modes [105].

and the integrand is equivalent to the 2 times Berry curvature. We can separate the integration variables into two component of 2D plane and one of perpendicular direction. For example,

$$\begin{aligned}\sigma_{xy} &= \frac{e^2}{\pi h}\int dk_z \frac{1}{2\pi}\int d^2k\,(\Omega_-)_{xy} \\ &= \frac{e^2}{\pi h}\int dk'_z C_{2D}\left(k'_z\right) \\ &= \frac{e^2}{2\pi h}\nu_z \end{aligned} \tag{3.31}$$

where $C_{2D}\left(k'_z\right)$ is the total Chern number of 2D slice from the plane with $k_z = k'_z$. ν_z has units of the inverse of the length scale. The final result is

$$\sigma_{ij} = \frac{e^2}{2\pi h}\epsilon^{ijk}\left(\boldsymbol{\nu}\right)_k \tag{3.32}$$

where $\boldsymbol{\nu}$ is some vector in momentum space, named the *Chern vector*. In the hyperhoneycomb lattice, the vector is roughly $\approx \left(2\pi/\sqrt{3}, -2\pi/\sqrt{3}, 0\right)$. In short, in the AQH phase, the bulk of the system is a semimetal with topologically protected Weyl quasiparticles. In this state, topological surface Hall currents spontaneously emerge. Those currents are maximized along the Chern vector $\vec{\boldsymbol{\nu}}$ in momentum space.

A physical consequence of those topological surface currents is manifested in appearance of low energy states in the form of Fermi arcs connecting the Weyl points. The Fermi arcs can be obtained numerically by projecting zero modes of the sliced BZ. In Fig. 3.7b, we scan the energy spectrum of the $k_z = 0$ plane along the k_x axis along three paths indicated by the dotted horizontal lines in panel 3.7a. Line 1 ($k_y = 3\pi/(4\sqrt{3})$ intersects a Fermi arc close to the node at $\mathbf{Q}_1$, as indicated by the arrow in the left panel of Fig. 3.7b, which has a zero energy crossing in the vicinity of a node. The scan on line 2, at $k_y = \pi/(2\sqrt{3})$, does not intercept a Fermi arc, as shown in the center panel

of Fig. 3.7b. The third path at $k_y = \pi/(10\sqrt{3})$ crosses the Fermi arc near the center of the zone, as indicated by the zero energy mode shown in the right panel of Fig. 3.7b.

We have shown that hyperhoneycomb lattices with spinless fermions may host a 3D QAH effect, which competes with a CDW state. The 3D anomalous Hall conductivity σ_{ij} is $e^2/\left(\sqrt{3}ha\right)$ for (i,j)=(y,z) or (x,z). Due to the symmetry of the mass term, which spontaneously breaks TR symmetry around the nodal line, the low energy excitations of the QAH state have a rich structure, with Weyl fermions in bulk and topologically protected surface states.

Chapter 4

Elastic QHE and Elastic Hall viscosity

4.1 Preview

The electronic structure of a lattice is amenable to many external influences, including mechanical deformation. Usually mechanical strain smoothly changes interatomic distances but does not drastically change electronic properties of the lattice. However, in systems with Dirac fermions such as graphene, strain shifts Dirac points in a similar way to the effect of an external applied magnetic field. In other words, strain deformations couple to charge carriers as an gauge-field vector potential $\mathbf{A}$. Interestingly, the strain-induced pseudomagnetic field has opposite sign for two different valleys K and K' of graphene. Hence, elastic deformations do not break the time-reversal symmetry of the system and produce no net magnetic flux. In honeycomb lattices such as graphene [114], strain deformations can induce Landau level (LL) quantization with very large effective pseudomagnetic fields [112, 113, 115, 127]. In graphene nanobubbles, for instance, pseudomagnetic fields as large as 300 tesla have been observed with scanning tunneling spectroscopy [113].

When the chemical potential is inside the gap of the LLs, the Hall conductivity per valley is quantized and the system is expected to show a zero-field quantum Hall effect (QHE). Due to the dispersion of the LLs, Hall conductivity quantization is not common in three dimensions (3D), and may occur only in extremely anisotropic systems such as Bechgaard salts [116, 117], Bernal graphite [118, 119], and in nodal-line semimetals [120–122]. Even in strongly anisotropic systems such as in nodal line semimetals, the physical implementation of the 3D QHE is challenging due to the unusual toroidal field geometry required [120]. With the help of strain engineering, one may in principle design 3D LLs with well defined gaps in between from real space configurations of magnetic field that would be otherwise impractical to realize.

In this chapter, we derive the elastic gauge fields that follow from arbitrary lattice deformations in the hyperhoneycomb lattice, a natural 3D generalization of the honeycomb geometry where all sites are connected by coplanar trigonal bonds, as shown in Fig. 3.3. In the semimetallic form, this lattice is an example of a nodal-line semimetal [49, 54, 78, 120, 124–126]. We identify a whole family of lattice deformations that produce uniform nearly flat LLs in 3D, a prerequisite for the 3D zero-field QHE. We show that this family of non-trivial deformations can be physically implemented

with the application of a simple temperature gradient along the axis perpendicular to the nodal line, leading to a tunable metal-insulator transition in the bulk. The strain deformations can be uniquely specified by the set of thermal expansion coefficients of the crystal. We propose that a tunable temperature controlled 3D zero-field QHE can be implemented in acoustic metamaterials [128].

In the presence of topological states, the topological invariants can manifest in the elastic response of the crystal through phonons. In the 3D quantum anomalous Hall (QAH) phase [105], which is the extension of the Haldane model [14] to the hyperhoneycomb lattice, we also calculate the elastic Hall viscosity tensor $\eta_{\mu\nu\rho\gamma}$. Also known as the phonon Hall viscosity [130], this quantity is analogous to the dissipationless viscous response of electrons in the quantum Hall regime [132–134] and is topological in nature. We show that the components of the Hall viscosity tensor are $\pm\eta_H$ or $\pm 2\eta_H$ (or zero), with $\eta_H = \beta^2\sqrt{3}/\left(8\pi a^3\right)$, where β is an elastic parameter and a is the lattice constant.

4.2 Elastic gauge field in hyperhoneycomb lattice

As described in the last chapter, the hyperhoneycomb lattice has four sites per unit cell $\mu = 1, \cdots, 4$ and is generated by the lattice vectors $\mathbf{a}_1 = (\sqrt{3}, 0, 0)$, $\mathbf{a}_2 = (0, \sqrt{3}, 0)$, and $\mathbf{a}_3 = (-\sqrt{3}/2, \sqrt{3}/2, 3)$, in units of the lattice constant a. In the momentum space, the reciprocal lattice is generated by the vectors $\mathbf{b}_1 = (2\pi/\sqrt{3}, 0, -\pi/3)$, $\mathbf{b}_2 = (0, -2\pi/\sqrt{3}, \pi/3)$ and $\mathbf{b}_3 = (0, 0, 2\pi/3)$, shown in Fig. 3.3. The tight-binding Hamiltonian is a 4×4 matrix [120]

$$\mathcal{H}_{0,\mu\nu}(\mathbf{k}) = -t_0 \sum_{\vec{\delta}_{\mu\nu}} \mathrm{e}^{i\mathbf{k}\cdot\vec{\delta}_{\mu\nu}}, \tag{4.1}$$

where t_0 is the hopping amplitude, $\vec{\delta}_{\mu\nu}$ are the nearest neighbor (NN) vectors between sites of species μ and ν and $\mathbf{k}$ is the momentum measured from the center of the Brillouin zone (BZ). In total, there are six NN vectors $\vec{\delta}_{12} = \left(\pm\sqrt{3}a/2, 0, a/2\right)$, $\vec{\delta}_{34} = \left(0, \pm\sqrt{3}a/2, a/2\right)$, $\vec{\delta}_{14} = (0, 0, -a)$ and $\vec{\delta}_{23} = (0,\, 0, a)$. The low energy bands of this lattice have a line of Dirac nodes $\mathbf{k}_0 = [k_x(s), k_y(s), 0]$ in the $k_z = 0$ plane, which can be written in terms of some parameter s that satisfies the equation $4\cos[3k_x(s)/2]\cos[3k_y(s)/2] = 1$. The low energy projected Hamiltonian is described by a 2×2 matrix expanded around the nodal line

$$\mathcal{H}_{0,p}(\mathbf{q}) = \left[v_x(s)q_x + v_y(s)q_y\right]\sigma_1 + v_z(s)q_z\sigma_2 \tag{4.2}$$

where $\mathbf{q} \equiv \mathbf{k} - \mathbf{k}_0(s)$ is the relative momentum, σ_1, σ_2 are the two off-diagonal Pauli matrices and

$$\begin{aligned} v_x(s) &= \frac{\sqrt{3}}{1+\alpha^2} \sin\left(\frac{\sqrt{3}}{2} k_x(s)\right) t_0 \\ v_y(s) &= \frac{\alpha^2\sqrt{3}}{1+\alpha^2} \sin\left(\frac{\sqrt{3}}{2} k_y(s)\right) t_0 \\ v_z(s) &= -\frac{3\alpha}{1+\alpha^2} t_0, \end{aligned} \tag{4.3}$$

are the velocities of the quasiparticles, with $\alpha(s) \equiv 2\cos[\sqrt{3}k_x(s)a/2]$ [105]. The energy spectrum of the quasiparticles is $E_0(\mathbf{q}) = \pm\sqrt{(v_x q_x + v_y q_y)^2 + v_z^2 q_z^2}$. The wavefunctions have a π Berry phase for closed line trajectories that encircle the nodal loop.

Elastic gauge fields. The inclusion of lattice deformations can be done by locally changing the distance between lattice sites, which affect value of the hopping constant. Expanding it to lowest order in the displacement of the lattice,

$$t\left(\vec{\delta}^{(n)} + \delta\mathbf{r}\right) \approx t_0 + \frac{\beta}{a^2} \delta_i^{(n)} \delta_j^{(n)} u_{ij} + \mathcal{O}\left(\delta r^2\right), \tag{4.4}$$

with $n = 1, \ldots, 6$ indexing the 6 NN lattice vectors $\vec{\delta}^{(n)}$, $u_{ij} = \frac{1}{2}\left(\partial_i u_j + \partial_j u_i\right)$ is the strain tensor defined in terms of the displacement field $\mathbf{u}$ of the lattice and $\beta = a\frac{\partial t}{\partial r} = \frac{\partial \log t}{\partial \log r}$ is the Grüneisen parameter of the model [129]. Including the lattice distortions in Hamiltonian (4.5), one gets two terms, $\mathcal{H}_p = \mathcal{H}_{0,p} + \mathcal{H}_{el}$, where

$$\mathcal{H}_{el} = \frac{3}{4}\frac{\beta}{a} v_z \left(u_{xx} + u_{yy} - 2u_{zz}\right)\sigma_1 - \frac{\beta}{a}\left(v_x u_{xz} + v_y u_{yz}\right)\sigma_2 \tag{4.5}$$

is the elastic contribution. As in the 2D case (graphene), the deformation of the lattice couples to the Dirac fermions as an elastic gauge field $\mathbf{A}$. It is convenient to rewrite the Hamiltonian in the more familiar form

$$\mathcal{H}_p(\mathbf{q}) = \left[v_x\left(q_x + A_x\right) + v_y\left(q_y + A_y\right)\right]\sigma_1 + v_z\left(q_z + A_z\right)\sigma_2, \tag{4.6}$$

where

$$\begin{aligned} A_x(s) &= \frac{v_x v_z}{v_\rho^2}\frac{3\beta}{4a}\left(u_{xx} + u_{yy} - 2u_{zz}\right) \\ A_y(s) &= \frac{v_y v_z}{v_\rho^2}\frac{3\beta}{4a}\left(u_{xx} + u_{yy} - 2u_{zz}\right) \\ A_z(s) &= -\frac{\beta}{a}\left(\frac{v_x}{v_z} u_{xz} + \frac{v_y}{v_z} u_{yz}\right) \end{aligned} \tag{4.7}$$

are the components of the elastic gauge field along the nodal line, with $v_\rho^2(s) = v_x^2(s) + v_y^2(s)$. The definition of the A_x and A_y components is to a degree arbitrary. In (4.7) we chose the most

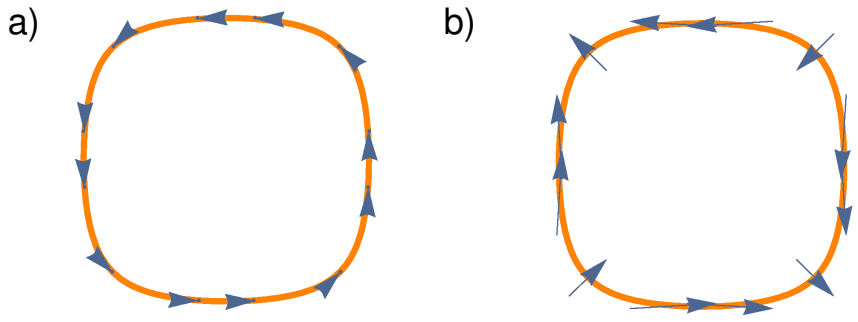

Figure 4.1: Pseudomagnetic field $\mathbf{B}$ along the nodal line for two different strain field configurations, (a) $\mathbf{u} = \left(2xz, 2yz, z^2\right)$ and (b) $\mathbf{u} = (2yz, 2xz, 0)$ Both configurations preserve TRS as $\mathbf{B}$ fields (or gauge fields $\mathbf{A}$) on the other side of the nodal line have opposite sign. Only configuration (a) produces nearly flat LLs. [106].

symmetric combination, although this choice has no effect in physical observables.

Those gauge fields can be associated to a pseudomagnetic field $\mathbf{B} = \nabla \times \mathbf{A}$, which follows from lattice deformations and hence must preserve time reversal symmetry (TRS). While pseudo magnetic fields couple to the Dirac fermions similarly to conventional magnetic fields and can produce Landau level (LL) quantization, they create a zero net magnetic flux at each lattice site. Therefore, electrons sitting at opposite points in the nodal line are related by TRS and must necessarily couple to opposite $\mathbf{B}$ fields. In order to produce zero-field quantum Hall effect, one needs to create 3D LL quantization with well defined gaps in between. In 2D, the conventional Hall conductivity σ_{xy} is a dimensionless and quantized in units of e^2/h. In 3D, it has an extra unit of inverse length. According to Halperin [110], the Hall conductivity tensor is $\sigma_{ij} = e^2/(2\pi h)\epsilon_{ijk}G_k$, where $\mathbf{G}$ is some reciprocal vector (and could be zero). In general, a finite Hall conductivity in 2D (3D) is allowed whenever the chemical potential is in the gap between different LLs, and implies in the existence of chiral edge (surface) states. At zero field, the Hall conductivity tensor due to pseudomagnetic fields does not create chiral charge currents as in the conventional quantum Hall effect, but rather a valley current.

4.3 Strain engineering

In all possible strain configurations, the effective Hamiltonian (4.6) has the form $\mathcal{H}_p(\mathbf{q}) = h_1\sigma_1 + h_2\sigma_2$. In specific, for configuration $\mathbf{u} = (2xz, 2yz, z^2)$,

$$h_1 = v_x q_x + v_y q_y \tag{4.8}$$

$$h_2 = v_z q_z - \frac{\beta}{a} v_x x - \frac{\beta}{a} v_y y. \tag{4.9}$$

The corresponding pseudomagnetic field $\mathbf{B} = (-v_y/v_z, v_x/v_z, 0)$ forms a closed loop in the BZ around the nodal line, as shown in Fig. 4.1a. In order to calculate the spectrum of Landau levels, we generically define the canonically conjugated ladder operators

$$a = \frac{1}{\omega}\left(h_1 + ih_2\right), \quad a^\dagger = \frac{1}{\omega}\left(h_1 - ih_2\right) \tag{4.10}$$

which satisfy $\left[a, a^\dagger\right] = 2i\left[h_2, h_1\right]/\omega^2 = 1$. The parameter

$$\omega\left(s\right) = \sqrt{\frac{\beta}{a}}\left[2v_x^2\left(s\right) + 2v_y^2\left(s\right)\right]^{\frac{1}{2}} \tag{4.11}$$

is the analog of the cyclotronic frequency. By taking the square of the Hamiltonian, we can write it in terms of the ladder operator only and define the eigenvalue as E^2,

$$\left[\mathcal{H}_u^P\left(s\right)\right]^2 = \omega^2\left[a^\dagger a + \frac{1}{2}\right]\sigma_0 - \frac{1}{2}\omega^2\sigma_3 \tag{4.12}$$

$$E_N^2\left(s\right) = \omega^2\left(s\right)N, \qquad N \in \{0, 1, 2, \cdots\} \tag{4.13}$$

That results in the spectrum of the LLs parametrized along the nodal line,

$$E_N\left(s\right) = \mathrm{sign}(N)\omega\left(s\right)\sqrt{|N|}, \tag{4.14}$$

where $N \in \mathbb{Z}$. Because $\omega^2\left(s\right)$ is nonzero positive for everywhere on the node line with this deformation, the gap between LLs is well defined, and the energy spectrum has a zeroth LL, as expected for Dirac fermions (see Fig 4.2a). That permits the emergence of a zero-field QHE due to strain whenever the chemical potential lays in the LL gap. However, not all deformations with spatially independent pseudomagnetic fields create 3D LL quantization with well-defined gaps in between. For the strain configuration $\mathbf{u} = (2yz, 2xz, 0)$, which corresponds to the pseudomagnetic field $B = (-v_x/v_z, v_y/v_z, 0)$ shown in Fig 4.1(b), the parameter ω is defined as

$$\omega\left(s\right) = \sqrt{\frac{\beta}{a}\left|v_x\left(s\right)v_y\left(s\right)\right|} \tag{4.15}$$

has zeros at some points on the node line, where all LLs collapse, as shown in Fig 4.2(b). In that configuration, although the LLs are well defined away from those points, the system does not have a zero-field QHE since their dispersion does not show a well-defined gap in the excitation spectrum [106].

One can generalize the deformation of Fig 4.2 (a) and (c) to a families of strain deformations that lead to a 3D zero-field QHE,

$$\mathbf{u} = \left(\alpha_x xz, \alpha_y yz, \alpha_z z^2\right). \tag{4.16}$$

While the energy spectrum is generically defined by Eq. (4.14), in those families $\omega(s) = \sqrt{2|[h_2, h_1]|}$

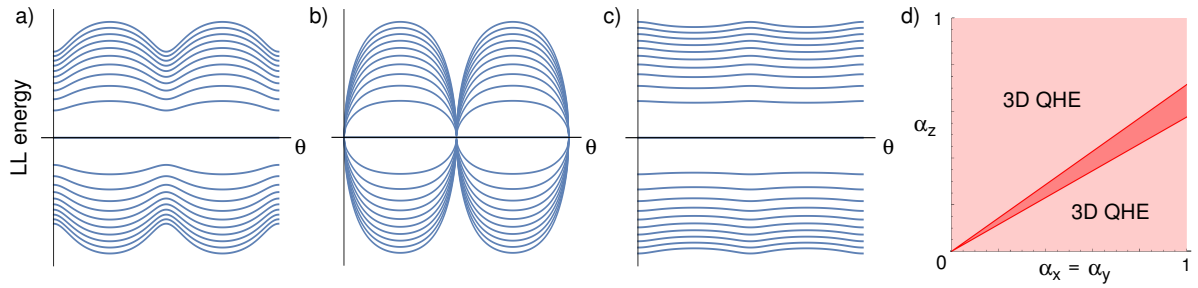

Figure 4.2: Energy of the Landau levels (LLs) around the nodal line vs polar angle θ of the line ($0 \leq \theta < \pi$) for three strain configurations: (a) $\mathbf{u} = \left(2xz, 2yz, z^2\right)$, (b) $\mathbf{u} = (2yz, 2xz, 0)$, and (c) $\mathbf{u} = \left(2xz, 2yz, z^2\right)$. The first and third configurations belong to a broader family of deformations of $\mathbf{u} = \left(2xz, 2yz, z^2\right)$ that produce nearly flat LLs in 3D. In the second configuration, the LLs collapse at discrete points of the nodal line, preventing the zero-field QHE. (d) Phase space for $\alpha_x = \alpha_y$ and α_z with a zero-field 3D QHE (light red regions) [106].

can be non zero for all points along the nodal line,

$$\omega = \sqrt{\frac{\beta}{a}\left|\alpha_x v_x^2(s) + \alpha_y v_y^2(s) + \frac{3}{2}\left(\alpha_x + \alpha_y - 4\alpha_z\right) v_z^2\right|}. \tag{4.17}$$

where the constants α_i ($i = x, y, z$) are such that $\omega(s) \neq 0$ for all s. The anisotropic case $\alpha_x = \alpha_y \gg \alpha_z$ is shown in Fig. 4.2c. The phase space of parameters with $\alpha_x = \alpha_y$ that leads to a zero-field QHE is shown in the light red areas of Fig. 4.2d., which is non zero for values of α_i ($i = x, y, z$) in the QHE phase in Fig 4.2(d).

One way to implement the family of deformations (4.16) is by applying a mechanical force field which generates a deformation over entire sample. For instance, the deformation pattern $\mathbf{u} = (2xz, 2yz, 0)$ can be created with the strain forces indicated by the arrows in Fig. 4.3a. Interestingly, the physical implementation of a subset of those deformations can be achieved with the application of a uniform temperature gradient along the z axis of the crystal (see Fig. 4.3b). Since $\mathbf{u}$ describes the displacement of the lattice sites from their equilibrium position, the thermal expansion is represented as $u_i = \Delta x_i = x_i \gamma_i \Delta T \propto \gamma_i x_i z$, where $\gamma_i = \mathrm{d}x_i/\mathrm{d}T$ is the linear thermal expansion coefficient in the $i = x, y, z$ direction and $\Delta T(z) = T - T_0 \propto z$ is the temperature variation from equilibrium. This tunable pattern of deformations could be created with temperature gradients in crystals and acoustic metamaterials [128].

4.4 Hall viscosity

In quantum Hall systems, the Hall viscosity follows from the linear response of the system to gravitational fluctuations, which manifest through local changes in the metric of space $\xi_{ij} = \frac{1}{2}(\partial_i \xi_j + \partial_j \xi_i)$, where ξ_i has the physical meaning of a strain field. The so called gravitational Hall viscosity is defined as the variation of the stress tensor $T_{\mu\nu} = \partial\mathcal{H}/\partial\xi_{\mu\nu}$ to time variations of the strain tensor $\dot{\xi}_{ij}$. By analogy, the elastic (phonon) Hall viscosity can be derived using linear response as

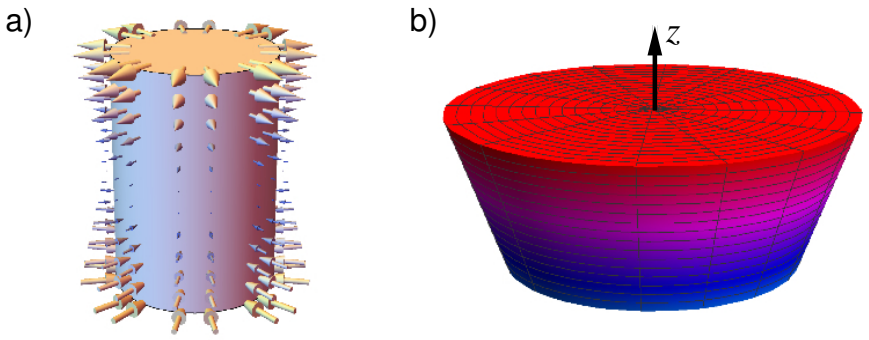

Figure 4.3: (a) Elastic deformation of a cylindrical sample under the deformation $\mathbf{u} = (2yz, 2xz, 0)$. The arrows indicate the forces that create uniform nearly flat LLs as in Fig 4.2(b) in HHC lattice. (b) Temperature gradient along the z axis (red: hot, blue: cold) that implements the strain field $\mathbf{u}$ at 4.16. Coefficient α_i $(i = x, y, z)$ corresponds to the thermal expansion coefficients in i direction [106].

[130, 131, 133, 134]

$$\left\langle \frac{\partial \mathcal{H}_p}{\partial \xi_{\mu\nu}} \right\rangle = \lambda_{\mu\nu\rho\gamma}\xi_{\rho\gamma} + \eta_{\mu\nu\rho\gamma}\dot{\xi}_{\rho\gamma} \tag{4.18}$$

where $\langle \ldots \rangle$ integrates over the fermions, $\lambda_{\mu\nu\rho\gamma}$ is the elastic moduli, $\dot{u}_{\rho\gamma}$ the strain-rate tensor and $\eta_{\mu\nu\rho\gamma}$ the elastic Hall viscosity tensor. The first term is the elastic response of a charge neutral fluid and the second one the viscous response [133, 134]. As the stress tensor, the tensors u, $\dot{u}$ are symmetric, while the viscosity tensor is symmetric under $\mu \leftrightarrow \nu$ or $\rho \leftrightarrow \gamma$. However, with respect to $\mu\nu\alpha\beta \leftrightarrow \alpha\beta\mu\nu$, $\eta_{\mu\nu\alpha\beta}$ can be separated into symmetric part $\eta^S_{\mu\nu\alpha\beta}$ and antisymmetric part $\eta^A_{\mu\nu\alpha\beta}$:

$$\eta^S_{\mu\nu\alpha\beta} = \eta^S_{\alpha\beta\mu\nu} \tag{4.19}$$

$$\eta^A_{\mu\nu\alpha\beta} = -\eta^A_{\alpha\beta\mu\nu}. \tag{4.20}$$

The symmetric part is associated with dissipation, and the antisymmetric part of the viscosity tensor describes non dissipative response. $\eta^A_{\mu\nu\alpha\beta}$ can only be nonzero when time reversal symmetry ($\mathcal{T}$) is broken and is called "odd" viscosity [133, 134]. For a quantum fluid, this dissipationless viscosity can be observed in the quantum Hall effect (QHE), is hence $\eta^A_{\alpha\beta\mu\nu}$ also called the Hall viscosity. Possible experimental signatures of this Hall viscosity have been proposed in [135–137]. In general, one can calculate the antisymmetric viscosity tensor from the effective action,

$$\delta\mathcal{S}_{\text{eff}} = \frac{1}{2}\int d^3x\, dt\, \eta_{\mu\nu\alpha\beta} u_{\mu\nu} \dot{u}_{\alpha\beta}, \tag{4.21}$$

which resembles a Chern-Simons action for the usual QHE [138, 139]. We will consider the elastic Hall viscosity for the 3D QAH state, which is an extension of the Haldane model for the hyperhoneycomb lattice, described in detail in chapter 3. For nodal line semimetals, loop currents on the

lattice can create a mass term around the nodal line with the general form

$$\mathcal{H}_m(\mathbf{q}) = \left[m(s) + \sum_{i=x,y,z} v_i'(s) q_i \right] \sigma_3, \tag{4.22}$$

according to Eq. (3.23), where $v_i'(s)$ is gives the mass dispersion in the $i = x, y, z$ direction. The Haldane mass $m(s)$ changes sign at $2(2n+1)$ points along the nodal line, with $n \in \mathbb{N}$, breaking inversion and TRS symmetry [104, 105]. The nodes of the mass, where $m(s) = 0$, are Weyl points with a well defined helicity [105].

In the QAH state, the projected Hamiltonian away from the Weyl points of the nodal line has the form

$$\mathcal{H}^P_{\mathrm{QAH}}(\mathbf{q}) = \mathcal{H}_0(\mathbf{q}) + \mathcal{H}_m(\mathbf{q}), \tag{4.23}$$

The effective action in terms of the strain tensor u_{ij} can be derived by integrating out the fermions. That results in the effective action $S_{\mathrm{ef}}(u) = \mathrm{Tr}\left[\ln\left(G^{-1}\right)\right]$, where $G^{-1}(q) = iq_0 - \mathcal{H}^P_{\mathrm{QAH}}(\mathbf{q}) - \Sigma_{\mathrm{el}}$ is the Green's function and

$$\Sigma_{\mathrm{el}}(u) = v_z A_1 \sigma_1 + (v_x A_2 + v_y A_2')\sigma_2 \equiv \sum_{\mu=1,2} h_u^\mu \sigma_\mu \tag{4.24}$$

is the self-energy due to elastic terms, which follows from (4.6). For convenience, we defined the elastic gauge fields in (4.5) as $A_1 = -\frac{\beta}{a}\frac{3}{4}(u_{xx} + u_{yy} - 2u_{zz})$, $A_2 = -\frac{\beta}{a}u_{xz}$ and $A_2' = -\frac{\beta}{a}u_{yz}$, with

$$(h_u)_1 = v_z \bar{A}_1, \qquad (h_u)_2 = v_x \bar{A}_2 + v_y \bar{A}_2'. \tag{4.25}$$

To see how the elastic gauge field $\mathbf{A}^{el}$ couples to the system, we expanding the action in powers of the elastic gauge fields,

$$\begin{aligned} \mathcal{S}_{\mathrm{eff}} &= N\,\mathrm{Tr}\left[\ln\left(G^{-1}\right)\right] \\ &= N\,\mathrm{Tr}\left[\ln\left(G_0^{-1} - \Sigma_{\mathrm{el}}\right)\right] \qquad (4.26) \\ &= N\,\mathrm{Tr}\left[\ln G_0^{-1} - \sum_n \frac{1}{n}\left(G_0\Sigma_{\mathrm{el}}\right)^n\right], \qquad (4.27) \end{aligned}$$

where

$$G_0^{-1}(k) = ik_0 - \mathcal{H}^P_{\mathrm{QAH}}(\mathbf{k}) \tag{4.28}$$

is the unperturbed Green's function in the QAH state. The lowest order contribution to the Hall viscosity comes from two loop, $S^{(2)}_{\mathrm{ef}} = -\frac{1}{2}\mathrm{tr}\left[G_0\Sigma_{\mathrm{el}}G_0\Sigma_{\mathrm{el}}\right]$. This term is reminiscent of the Chern-Simon term. Let's take Fourier transformation for the second order term,

$$\mathcal{S}'_{\mathrm{eff}} = -\frac{N}{2}\int \frac{d^3k}{(2\pi)^3}\left[h_u^\mu \Pi^{\mu\nu} h_u^\nu\right], \tag{4.29}$$

where

$$\Pi^{\mu\nu} = \int \frac{d^3q}{(2\pi)^3} \mathrm{Tr}\left[G_0\left(q+k\right)\sigma_\mu G_0\left(q\right)\sigma_\nu\right].$$

In graphene, h_1 and h_2 are equal to $v_x A_x$ and $v_y A_y$ respectively, as follows from application of the minimal substitution rule. However, one should note that h_u^μ is defined in (4.24) and (4.25) hence $\bar{A}_1$ and $\bar{A}_2$ in h_u^μ are distinguished from $v_\alpha A_\alpha$ in chapter 4.2. From (4.29), the term in the action which is expected to give the antisymmetric Hall viscosity is:

$$\mathcal{S}'_{\mathrm{eff}} = -\frac{N}{2}\int \frac{d^4k}{(2\pi)^4}\left[v_x v_z \bar{A}_1 \Pi^{12} \bar{A}_2 + v_y v_z \bar{A}_1 \Pi^{12} \bar{A}'_2 + (1 \leftrightarrow 2)\right]. \tag{4.30}$$

We calculate the action by integrating first on a slice on the xz plane for the first term and in the yz plane for the second term. This is the trick we used in the calculation of Hall conductance. The first term is

$$\begin{aligned} v_x v_z \Pi^{12} &= \int \frac{d^4q}{(2\pi)^4} v_x v_z \mathrm{Tr}\left[G_0\left(q+k\right)\sigma_1 G_0\left(q\right)\sigma_2\right] \\ &= \int \frac{dq_y}{(2\pi)}\left\{\int \frac{dq_0 dq_x dq_z}{(2\pi)^3} v_x v_z \mathrm{Tr}\left[G_0\left(q+k\right)\sigma_1 G_0\left(q\right)\sigma_2\right]\right\} \\ &= \int \frac{dq_y}{(2\pi)} v_x v_z \int \frac{dq_0 dq_x dq_z}{(2\pi)^3} \mathrm{Tr}\left[\frac{iq_0 + \mathcal{H}^P_{\mathrm{QAH}}\left(\mathbf{q}+\mathbf{k}\right)}{q_0^2 + \left[\mathcal{H}^P_{\mathrm{QAH}}\left(\mathbf{q}+\mathbf{k}\right)\right]^2}\sigma_1 \frac{iq_0 + \mathcal{H}^P_{\mathrm{QAH}}\left(\mathbf{q}\right)}{q_0^2 + \left[\mathcal{H}^P_{\mathrm{QAH}}\left(\mathbf{q}\right)\right]^2}\sigma_2\right]. \end{aligned} \tag{4.31}$$

The result of the integral (4.31) is

$$v_x v_z \Pi^{12} = \int \frac{dq'_y}{(2\pi)} \frac{1}{2\pi} \left[C_{2D}\right]_{q_y = q'_y} k_0 \tag{4.32}$$

where $\left[C_{2D}\right]_{q_y=q'_y}$ is the 2D Chern number of the slice (or Section Chern number) with $q_y = q'_y$ when q'_y is constant value for the slice. Integrating the Section Chern number over q'_y corresponds to the half of the y component of Chern vector $\vec{\boldsymbol{\nu}}$ we defined at (3.32).

$$v_x v_z \Pi^{12} = \frac{1}{8\pi^2}\nu_y k_0. \tag{4.33}$$

In the same way,

$$v_y v_z \Pi^{12} = \frac{1}{8\pi^2}\nu_x k_0, \tag{4.34}$$

For $v_x v_z \Pi^{21}$ and $v_y v_z \Pi^{21}$, those terms simply change sign from the result above. Applying them to (4.30), we get

$$v_x v_z \bar{A}_1 \Pi^{12} \bar{A}_2 + v_y v_z \bar{A}_1 \Pi^{12} \bar{A}'_2 \tag{4.35}$$

or equivalently

$$\mathcal{S}'_{eff} = -\frac{N}{2}\int \frac{dk_0 d^3k}{(2\pi)^4}\frac{1}{8\pi^2}\left[\nu_y \bar{A}_1 k_0 \bar{A}_2 + \nu_x \bar{A}_1 k_0 \bar{A}'_2 - \nu_y \bar{A}_2 k_0 \bar{A}_1 - \nu_x \bar{A}'_2 k_0 \bar{A}_1\right]. \tag{4.36}$$

Defining $\bar{A}_1 = d_z$, $\bar{A}_2 = -d_x$, $\bar{A}'_2 = d_y$, we can write the effective action in a more compact form,

$$\mathcal{S}'_{eff} = \frac{N}{16\pi^2}\int \frac{dk_0 d^3k}{(2\pi)^3}\left[\epsilon^{\mu\nu\rho}\nu_\mu d_\nu k_0 d_\rho\right] \tag{4.37}$$

where

$$\begin{cases} d_x = \frac{\beta}{a}\left(u_{xz}\right) \\ d_y = -\frac{\beta}{a}\left(u_{yz}\right) \\ d_z = \frac{\beta}{4a}\left(u_{xx} + u_{yy} - 2u_{zz}\right). \end{cases} \tag{4.38}$$

For the hyperhoneycomb lattice, the Chern vector is $\vec{\boldsymbol{\nu}} = (2\pi/\sqrt{3}, -2\pi/\sqrt{3}, 0)a^{-1}$ [105]. Writing the action in a more explicit form,

$$S'_{eff} = \frac{N}{16\pi^2}\int d^4x\, \eta_H \left[\left(u_{xx} + u_{yy} - 2u_{zz}\right)\left(-\dot{u}_{xz} + \dot{u}_{yz}\right)\right. \tag{4.39}$$

$$\left. - \left(-u_{xz} + u_{yz}\right)\left(\dot{u}_{xx} + \dot{u}_{yy} - 2\dot{u}_{zz}\right)\right] \tag{4.40}$$

where $\eta_H = \beta^2\sqrt{3}/\left(16\pi^2 a^3\right)$. The action can be cast in the form of Eq. (4.21), where the elastic Hall viscosity tensor is $\eta_{xx\alpha\beta} = \eta_{yy\alpha\beta} = \eta_H$ and $\eta_{zz\alpha\beta} = -2\eta_H$ for $(\alpha, \beta) \in \{(x, z), (y, z)\}$. The elastic Hall viscosity tensor is anisotropic, as expected in a nodal line system in 3D. Also, the Hall viscosity reflects the topological nature of the QAH state. For instance, the system with a tilted node line has broken $\mathcal{T}$ and $\mathcal{P}$ but preserves the product of the two, keeping the nodal line ungapped. This effect is not topological and does not convey a finite elastic Hall viscosity at zero temperature. Moreover, if one adapts a small tilt angle in the QAH state, particle-hole symmetry around the Weyl points is broken, inhibiting the topological response [106, 140, 141].

Although there are no known examples of semimetallic hyperhoneycomb crystals [142], this lattice may be artificially created in optical lattices [143], and also in photonic [115, 144] and acoustic metamaterials [128]. In twisted graphene bilayers, elastic gauge fields can be created with electric field effects [145]. In synthetic lattices, strain deformations can be readily implemented with local displacements of the lattice sites, without the need to apply pressure. While local probes such as scanning tunneling spectroscopy can fully characterize the LLs in 2D [113, 127], this method can be used to characterize the surface states of the LLs in the 3D case.

In quantum Hall systems, the measurement of the Hall viscosity is typically challenging [147], as it involves probing the response of the stress tensor under changes of the space metric [134]. In Galilean invariant systems in the hydrodynamic regime, the Hall viscosity can be determined solely in terms of the electromagnetic response due to a non-homogeneous electric field [148, 149]. The elastic Hall viscosity nevertheless can be measured in terms of the dispersion of sound waves. When

$\eta_H = \eta_{xxxz}$ is zero, the longitudinal and transverse modes are decoupled at long wavelengths. In the topological phase, where η_H is finite, the transverse and longitudinal modes are expected to mix, allowing one to measure the elastic Hall viscosity through the corrections to the dispersion of the phonons [130]. The quantum simulation of Chern insulating phases has been done in honeycomb lattices of cold atoms [143], in quantum circuits [150] and acoustic metamaterials [128]. We conjecture that the QAH state in 3D may be experimentally realized in synthetic lattices as well.

Chapter 5

Hydrodynamic transport

5.1 Introduction

Hydrodynamics describes the behavior of quantum fluids in the regime where the relaxation of electrons is dominated by collision among the quasiparticles. This theory describes long wavelength deviations from local thermal equilibrium, when transport is dominated by conservation laws [154]. Since the time between collisions is the shortest time scale in the problem, the electrons exchange momentum faster than they can relax to phonons or disorder. That leads to universal behavior in the form of a slow diffusion of densities and to viscous flow. This framework has been successfully applied to a variety of different systems, ranging from strong coupling gauge theories with holographic duals [155], quark-gluon plasma [156] and graphene [158, 159, 187].

It has been conjectured by Kovtun *et al.* [181] that relativistic quantum systems have a universal lower bound for the ratio between the sheer viscosity and the entropy, $\eta/s \geq (1/4\pi)\hbar/k_B$. The shear viscosity measures the longitudinal resistivity to transverse gradients in the velocity of the fluid. The lower bound has been associated with 'perfect fluids', systems that are so strongly interacting that they can display quantum turbulence [161, 187]. This ratio is widely believed to be a proxy for the strength of interactions in many classes of quantum systems, including Plankian metals [162], which entirely that lack quasiparticles.

In general, the shear viscosity $\eta \sim F\tau$, where F is the free energy and τ the relaxation time [163]. In relativistic systems at the neutrality point, the free energy is mostly entropic $F \sim sT$. In the absence of screening, the scattering time due to Coulomb interactions is $\tau \sim \hbar/(k_B T)$, and hence $\eta/s \sim \hbar/k_B$, with a prefactor of the order 1. In Fermi liquids, the free energy is dominated by the Fermi energy whereas $\tau \propto T^{-2}$. The entropy in a Fermi liquid $s \propto T$, and hence the ratio $\eta/s \propto T^{-3}$ diverges at low temperature and is typically very far above the lower bound for any realistic temperatures.

Violations of the lower bound were found before in strongly interacting conformal field theories. More recently, it has been suggested that anisotropic Dirac fermions found at a topological Lifshitz transition, where two Dirac cones merge [164], violate the proposed lower bound [165]. In this chapter, we show that in relativistic systems with a Fermi surface, such as in nodal-line semimetals

(NLSMs), the ratio between the shear viscosity and the entropy is *unbounded*,

$$\frac{\eta}{s} \propto \frac{\hbar}{k_B} \frac{k_B T}{v_F k_F}, \tag{5.1}$$

where k_F is the radius of the nodal line and v_F the velocity of the quasiparticles. Due to the absence of screening at the nodal line in combination with the presence of a large Fermi surface, the scattering time between collisions is nearly temperature independent, $\tau \sim \hbar/v_F k_F$, with additional logarithmic corrections. We confirm that behavior by calculating the longitudinal conductivity in the collision dominated regime ($\omega \ll \tau^{-1}$),

$$\sigma(\omega, T) \propto \frac{e^2}{h} \frac{k_B T}{v_F} \sim \frac{e^2}{h} k_F \left(k_B T \frac{\tau}{\hbar} \right), \tag{5.2}$$

which is indicative of insulating behavior. We point out that the violation of the lower bound does not indicate that NLSMs are perfect fluids, but rather suggest the necessity to modify the lower bound to account for unscreened relativistic systems with Fermi surfaces.

In this chapter, we offer a general overview of the quantum kinetic theory, which describes universal transport phenomena of quantum fluid in terms of the nonequilibrium statistical distribution of particles in response to external perturbation. When interaction of a system between different energy scales become important, electrons in the system are strongly correlated. At finite frequencies, there are two regimes for the transport coefficients. The collisionless limit $\omega \gg \tau^{-1}$ is dominated by particle-hole production. In contrast, the limit $\omega \ll \tau^{-1}$ is dominated by collisions between thermally excited particles and holes. The former regime can be experimentally accessed by optical experiments. The latter regime defines the hydrodynamic regime. In this regime, it is possible to investigate the universal collision dominated dynamics of a quasiparticle *fluid*, while the couplings to the lattice and to impurities can be ignored.

In the following sections we offer a general description of the quantum kinetic theory, and then apply those results to the well known case of graphene, where we describe the results for both the longitudinal conductivity and the shear viscosity. For those not interested in the arcane details of the derivation of the Boltzmann equation, one can skip to section 5.3. In the final sections we the same method to derive the conductivity and shear viscosity for a NLSM, which are the main results.

5.2 Quantum kinetic theory

In this section we derive the Boltzmann equation. In the Heisenberg representation, the time evolution of an operator is

$$i \frac{\partial}{\partial t} X(t) = [X(t), H(t)], \tag{5.3}$$

where $X(t) = e^{iHt}X(0)e^{-iHt}$. The expectation value of any operator X in grand-canonical ensemble can be written as

$$\langle X \rangle = \frac{\mathrm{Tr}\left[e^{-\beta(H-\mu N)}X\right]}{\mathrm{Tr}\left[e^{-\beta(H-\mu N)}\right]}. \tag{5.4}$$

The Green's functions are thermodynamic averages of products of the field operators $\psi^\dagger(\mathbf{r},t)$ and $\psi(\mathbf{r},t)$:

$$G\left(\mathbf{1},\mathbf{1'}\right) = \frac{1}{i}\left\langle \boldsymbol{T}\left(\psi(\mathbf{1})\psi^\dagger(\mathbf{1'})\right)\right\rangle \tag{5.5}$$

$$G_2\left(\mathbf{12},\mathbf{1'2'}\right) = \left(\frac{1}{i}\right)^2\left\langle \boldsymbol{T}\left(\psi(\mathbf{1})\psi(\mathbf{2})\psi^\dagger(\mathbf{2'})\psi^\dagger(\mathbf{1'})\right)\right\rangle \tag{5.6}$$

where G is one particle Green's function, and G_2 is two particle Green's function. $\mathbf{1}$ represents the coordinate and time of the particle (r_1,t_1) and so do $\mathbf{1'}$, $\mathbf{2}$ and $\mathbf{2'}$. $\boldsymbol{T}$ represents the Wick time-ordering operation. Ordering is given early (right) to late (left). Depends on time-ordering, we define

$$G\left(\mathbf{1},\mathbf{1'}\right) = G^{>}\left(\mathbf{1},\mathbf{1'}\right) = \frac{1}{i}\left\langle \psi(\mathbf{1})\psi^\dagger(\mathbf{1'})\right\rangle, \quad \text{for } t_1 > t_1' \tag{5.7}$$

$$G\left(\mathbf{1},\mathbf{1'}\right) = G^{<}\left(\mathbf{1},\mathbf{1'}\right) = \frac{1}{i}\left\langle \psi^\dagger(\mathbf{1'})\psi(\mathbf{1})\right\rangle, \quad \text{for } t_1 < t_1' \tag{5.8}$$

Here, $G^{>}$ is analytic when $0 > \mathrm{Im}\left(t_1 - t_{1'}\right) > -\beta$ and so is $G^{<}$ when $0 < \mathrm{Im}\left(t_1 - t_{1'}\right) < \beta$. Thus, the Green's functions are well defined in the interval $0 \le it \le \beta$. $G^{>,<}$ are related as

$$G^{<}\left(\mathbf{1},\mathbf{1'}\right)\big|_{t_1=0} = \pm e^{\beta\mu}G^{>}\left(\mathbf{1},\mathbf{1'}\right)\Big|_{t_1=-i\beta} \tag{5.9}$$

where it takes upper sign for boson and lower sign for fermion.

Finally, we define the spectral function

$$A\left(\mathbf{p},\omega\right) = G^{>}\left(\mathbf{p},\omega\right) \pm G^{<}\left(\mathbf{p},\omega\right), \tag{5.10}$$

which normalized as $\int \frac{d\omega}{2\pi}A\left(\mathbf{p},\omega\right) = 1$. It is related to the Green functions as

$$G^{>}\left(\mathbf{p},\omega\right) = \left[1 + f(\omega)\right]A\left(\mathbf{p},\omega\right) \tag{5.11}$$

$$G^{<}\left(\mathbf{p},\omega\right) = f(\omega)A\left(\mathbf{p},\omega\right) \tag{5.12}$$

where $f(\omega) = 1/\left(e^{-\beta(\omega-\mu)} \mp 1\right)$ is the equilibrium distribution function for bosons $(-)$ or fermions $(+)$.

5.2.1 Equations of motion

Let's assume general Hamiltonian with mass m and two-body potential $V\left(|\mathbf{r}-\mathbf{r}'|\right)$

$$\begin{aligned} H(t) = & \int d\mathbf{r} \frac{\nabla\psi^\dagger(\mathbf{r},t)\cdot\nabla\psi(\mathbf{r},t)}{2m} \\ & + \frac{1}{2}\int d\mathbf{r}d\mathbf{r}'\psi^\dagger(\mathbf{r},t)\psi^\dagger(\mathbf{r}',t)V\left(\left|\mathbf{r}-\mathbf{r}'\right|\right)\psi(\mathbf{r},t)\psi(\mathbf{r}',t). \end{aligned} \tag{5.13}$$

We can build the equations of motion using the Eq (5.3) and the commutation relations.

$$\left(i\frac{\partial}{\partial t}+\frac{\nabla^2}{2m}\right)\psi\left(\mathbf{r},t\right) = \int d\bar{\mathbf{r}}V\left(|\mathbf{r}-\bar{\mathbf{r}}|\right)\psi^\dagger\left(\bar{\mathbf{r}},t\right)\psi\left(\bar{\mathbf{r}},t\right)\psi\left(\mathbf{r},t\right) \tag{5.14}$$

$$\left(-i\frac{\partial}{\partial t'}+\frac{\nabla'^2}{2m}\right)\psi^\dagger\left(\mathbf{r}',t'\right) = \int d\bar{\mathbf{r}}'V\left(\left|\mathbf{r}'-\bar{\mathbf{r}}'\right|\right)\psi^\dagger\left(\bar{\mathbf{r}}',t'\right)\psi\left(\bar{\mathbf{r}}',t'\right)\psi^\dagger\left(\mathbf{r}',t'\right) \tag{5.15}$$

Then, we multiply $\psi^\dagger\left(\mathbf{r}',t'\right)$ and $\psi\left(\mathbf{r},t\right)$ respectively and take time-ordering operation $\boldsymbol{T}$ on both side. The spatial derivatives commute with $\boldsymbol{T}$, and the difference

$$\frac{\partial}{\partial t}\left\langle \boldsymbol{T}\left(\psi(\mathbf{1})\psi^\dagger(\mathbf{1}')\right)\right\rangle - \left\langle \boldsymbol{T}\left(\frac{\partial}{\partial t}\psi(\mathbf{1})\psi^\dagger(\mathbf{1}')\right)\right\rangle \tag{5.16}$$

is proportional to a delta function of $t_1 - t_1'$. Then, we find

$$\left(i\frac{\partial}{\partial t}+\frac{\nabla_1^2}{2m}\right)G\left(\mathbf{1},\mathbf{1}'\right) = \delta\left(\mathbf{1}-\mathbf{1}'\right) \pm i\int d\mathbf{r}_2 V\left(|\mathbf{r}_1-\mathbf{r}_2|\right)G_2\left(\mathbf{12};\mathbf{1}'\mathbf{2}^+\right) \tag{5.17}$$

$$\left(-i\frac{\partial}{\partial t'}+\frac{\nabla_{1'}^2}{2m}\right)G\left(\mathbf{1},\mathbf{1}'\right) = \delta\left(\mathbf{1}-\mathbf{1}'\right) \pm i\int d\mathbf{r}_2 V\left(\left|\mathbf{r}_2-\mathbf{r}_1'\right|\right)G_2\left(\mathbf{12}^-;\mathbf{1}'\mathbf{2}\right) \tag{5.18}$$

where the notation $2^\pm$ intended to imply the time must be chosen to be slightly larger (smaller) than the others. When $V \neq 0$, there are few approximations for the two particle Greens function G_2.

5.2.2 Hartree-Fock approximation & Born Collision approximation

In the system that has identical particles, we cannot distinguish particles in process from $\mathbf{1}$ and $\mathbf{2}$ to $\mathbf{1}'$ and $\mathbf{2}'$ for $G_2\left(\mathbf{12},\mathbf{1}'\mathbf{2}'\right)$. Considering the symmetry $G_2\left(\mathbf{12},\mathbf{1}'\mathbf{2}'\right) = \pm G_2\left(\mathbf{21},\mathbf{1}'\mathbf{2}'\right)$, we can take simple approximation

$$G_2\left(\mathbf{12},\mathbf{1}'\mathbf{2}'\right) = G\left(\mathbf{1},\mathbf{1}'\right)G\left(\mathbf{2},\mathbf{2}'\right) \pm G\left(\mathbf{1},\mathbf{2}'\right)G\left(\mathbf{2},\mathbf{1}'\right) \tag{5.19}$$

and its result is called Hartree-Fock approximation.

We can also consider a interaction in the process of G_2. It takes a form of

$$\begin{aligned} G_2\left(\mathbf{12},\mathbf{1'2'}\right) &= G\left(\mathbf{1},\mathbf{1'}\right)G\left(\mathbf{2},\mathbf{2'}\right) \pm G\left(\mathbf{1},\mathbf{2'}\right)G\left(\mathbf{2},\mathbf{1'}\right) \\ &\quad + \int d\bar{\mathbf{r}}_1 \int d\bar{\mathbf{r}}_2 \int d\bar{t}_1 v\left(\bar{\mathbf{r}}_1 - \bar{\mathbf{r}}_2\right) \\ &\quad \times \left[G\left(\mathbf{1},\bar{\mathbf{1}}\right)G\left(\bar{\mathbf{1}},\mathbf{1'}\right)G\left(\mathbf{2},\bar{\mathbf{2}}\right)G\left(\bar{\mathbf{2}},\mathbf{2'}\right)\right. \qquad (5.20) \\ &\quad \left. \pm G\left(\mathbf{1},\bar{\mathbf{1}}\right)G\left(\bar{\mathbf{1}},\mathbf{2'}\right)G\left(\mathbf{2},\bar{\mathbf{2}}\right)G\left(\bar{\mathbf{2}},\mathbf{1'}\right)\right]\big|_{\bar{t}_2=\bar{t}_1}. \qquad (5.21) \end{aligned}$$

Then, the equation of motion(49) has the form:

$$\left(i\frac{\partial}{\partial t} + \frac{\nabla_1^2}{2m}\right)G\left(\mathbf{1},\mathbf{1'}\right) - \int_0^{-i\beta} d\bar{t}_1 d\bar{\mathbf{r}}_1 \Sigma\left(\mathbf{1},\bar{\mathbf{1}}\right)G\left(\bar{\mathbf{1}},\mathbf{1'}\right) = \delta\left(\mathbf{1}-\mathbf{1'}\right), \qquad (5.22)$$

where $\Sigma\left(\mathbf{1},\mathbf{1'}\right) = \Sigma_{HF}\left(\mathbf{1},\mathbf{1'}\right) + \Sigma_C\left(\mathbf{1},\mathbf{1'}\right)$ with

$$\begin{aligned} \Sigma_{HF}\left(\mathbf{1},\bar{\mathbf{1}}\right) &= \delta\left(t_1 - \bar{t}_1\right)\delta\left(\mathbf{r}_1 - \bar{\mathbf{r}}_1\right)\int dr_3 v\left(\mathbf{r}_1 - \mathbf{r}_3\right)\left\langle n\left(r_3\right)\right\rangle \\ &\quad + iV\left(\mathbf{r}_1 - \bar{\mathbf{r}}_1\right)G^{<}(\mathbf{1},\bar{\mathbf{1}})\big|_{\bar{t}_1=t_1} \qquad (5.23) \end{aligned}$$

and

$$\begin{aligned} \Sigma_C\left(\mathbf{1},\bar{\mathbf{1}}\right) &= \pm i^2 \int dr_2 dr_{2'} V\left(\mathbf{r}_1 - \mathbf{r}_2\right) v\left(\mathbf{r}_{1'} - \mathbf{r}_{2'}\right) \\ &\quad \left[G\left(\mathbf{1},\mathbf{1'}\right)G\left(\mathbf{2},\mathbf{2'}\right)G\left(\mathbf{2'},\mathbf{2}\right) - G\left(\mathbf{1},\mathbf{2'}\right)G\left(\mathbf{2},\mathbf{1'}\right)G\left(\mathbf{2'},\mathbf{2}\right)\right]. \qquad (5.24) \end{aligned}$$

If we take Fourier transformation,

$$\left[i\frac{\partial}{\partial t} - \varepsilon\left(\mathbf{p}\right)\right]G\left(\mathbf{p},t-t'\right) - \int_0^{-i\beta} d\bar{t}\,\Sigma_C\left(\mathbf{p},t-\bar{t}\right)G\left(\mathbf{p},\bar{t}-t'\right) = \delta\left(t-t'\right) \qquad (5.25)$$

where $\varepsilon(\mathbf{p})$ and Σ_C is

$$\varepsilon\left(\mathbf{p}\right) = \frac{p^2}{2m} + nV\left(p\right) \pm \int_{p'} V\left(\mathbf{p}-\mathbf{p'}\right)\left\langle n\left(\mathbf{p'}\right)\right\rangle \qquad (5.26)$$

$$\begin{aligned} \Sigma_C\left(\mathbf{p},t-\bar{t}\right) &= \pm i^2 \int_{p_1}\int_{p_2}\int_{p_3} \frac{1}{2}\left(V\left(\mathbf{p}-\mathbf{p}_2\right) \pm V\left(\mathbf{p}-\mathbf{p}_3\right)\right)^2 \\ &\quad \times (2\pi)^d \delta^d\left(\mathbf{p}+\mathbf{p}_1-\mathbf{p}_2-\mathbf{p}_3\right)G\left(\mathbf{p}_1,\bar{t}-t\right)G\left(\mathbf{p}_2,t-\bar{t}\right))G\left(\mathbf{p}_3,t-\bar{t}\right). \qquad (5.27) \end{aligned}$$

The self-energy Σ_C above is composed of two analytic functions

$$\Sigma_C^{>}\left(\mathbf{p},t-\bar{t}\right) = \int \cdots G^{<}\left(\mathbf{p}_1,\bar{t}-t\right)G^{>}\left(\mathbf{p}_2,t-\bar{t}\right)G^{>}\left(\mathbf{p}_3,t-\bar{t}\right) \qquad (5.28)$$

$$\Sigma_C^{<}\left(\mathbf{p},t-\bar{t}\right) = \int \cdots G^{>}\left(\mathbf{p}_1,\bar{t}-t\right)G^{<}\left(\mathbf{p}_2,t-\bar{t}\right)G^{<}\left(\mathbf{p}_3,t-\bar{t}\right). \qquad (5.29)$$

We can derive two equations from (5.25). For the time domain $0 < t_1 < t_{1'} < -i\beta$, one is:

$$\begin{aligned}\left[i\frac{\partial}{\partial t} - \varepsilon(\mathbf{p})\right] G^{<}(\mathbf{p}, t-t') = &\int_0^{t_1} d\bar{t}\, \Sigma_C^{>}(\mathbf{p}, t-\bar{t})\, G^{<}(\mathbf{p}, \bar{t}-t') \\ &+ \int_t^{t'} d\bar{t}\, \Sigma_C^{>}(\mathbf{p}, t-\bar{t})\, G^{<}(\mathbf{p}, \bar{t}-t') \\ &+ \int_{t_{1'}}^{-i\beta} d\bar{t}\, \Sigma_C^{>}(\mathbf{p}, t-\bar{t})\, G^{>}(\mathbf{p}, \bar{t}-t'), \end{aligned} \tag{5.30}$$

and the other one has opposite sign for $<$ and $>$. Shift the time range by t_0 so that the time domain become $t_0 < t_1 < t_{1'} < t_0 - i\beta$. When $t_0 \to -\infty$, this is equivalent to the equations of motion for real-time Green's function $g(\mathbf{1}, \mathbf{1}')$ in perturbative approach[3]. The equation can be written as

$$\begin{aligned}&\left(i\frac{\partial}{\partial t} + \frac{\nabla_1^2}{2m} - U_{\text{eff}}(\mathbf{1})\right) g^{<}(\mathbf{1}, \mathbf{1}') \\ &= \int_{-\infty}^{t} d\bar{t}_1 d\bar{\mathbf{r}}_1 \left(\Sigma^{>}(\mathbf{1}, \bar{\mathbf{1}}) - \Sigma^{<}(\mathbf{1}, \bar{\mathbf{1}})\right) g^{<}(\bar{\mathbf{1}}, \mathbf{1}') \\ &\quad - \int_{-\infty}^{t'} d\bar{t}_1 d\bar{\mathbf{r}}_1 \Sigma^{<}(\mathbf{1}, \bar{\mathbf{1}}) \left(g^{>}(\bar{\mathbf{1}}, \mathbf{1}') - g^{<}(\bar{\mathbf{1}}, \mathbf{1}')\right) \end{aligned} \tag{5.31}$$

where

$$g(\mathbf{1}, \mathbf{1}') = \frac{1}{i}\left\langle \boldsymbol{T}\left(\psi(\mathbf{1})\psi^{\dagger}(\mathbf{1}')\right)\right\rangle. \tag{5.32}$$

It describes physical response of the system, which initially in thermodynamic equilibrium, to the applied disturbance U that affects the system as a form of $H' = \int d\mathbf{r} n(\mathbf{r}, t)\, U(\mathbf{r}, t)$. In linear response, Hartree approximation gives the effective potential as

$$U_{\text{eff}}(\boldsymbol{R}, T) = U(\boldsymbol{R}, T) \pm i \int d\boldsymbol{R}' V\left(\boldsymbol{R} - \boldsymbol{R}'\right) g^{<}\left(\boldsymbol{R}' T, \boldsymbol{R}' T\right). \tag{5.33}$$

Similarly the equation corresponding to (5.18) is

$$\begin{aligned}&\left(-i\frac{\partial}{\partial t'} + \frac{\nabla_{1'}^2}{2m} - U_{\text{eff}}(\mathbf{1}')\right) g^{<}(\mathbf{1}, \mathbf{1}') \\ &= \int_{-\infty}^{t} d\bar{t}_1 d\bar{\mathbf{r}}_1 \left(g^{>}(\mathbf{1}, \bar{\mathbf{1}}) - g^{<}(\mathbf{1}, \bar{\mathbf{1}})\right) \Sigma^{<}(\bar{\mathbf{1}}, \mathbf{1}') \\ &\quad - \int_{-\infty}^{t'} d\bar{t}_1 d\bar{\mathbf{r}}_1 g^{<}(\mathbf{1}, \bar{\mathbf{1}}) \left(\Sigma^{>}(\bar{\mathbf{1}}, \mathbf{1}') - \Sigma^{<}(\bar{\mathbf{1}}, \mathbf{1}')\right). \end{aligned} \tag{5.34}$$

When U varies slowly in space and time at relative coordinate $(\boldsymbol{R}, T)$, we can express the subtraction

[3]The green's function g is defined with Hamiltonian and operators in response to external disturbances U. When U turn on, evolution of operators are written in interaction representation. G and g are closely related and details can be found in the textbook [167].

of two equations (5.31,5.34) as

$$\begin{aligned}
&\left(i\frac{\partial}{\partial T}+\frac{\nabla_R\nabla_r}{m}-\left(r\cdot\nabla_R+t\frac{\partial}{\partial T}\right)U_{\text{eff}}\left(\boldsymbol{R},T\right)\right)g^{<}\left(\mathbf{r},t,\boldsymbol{R},T\right)\\
&=\int d\bar{\mathbf{r}}d\bar{t}\left[g^{<}\left(\mathbf{r},t,\boldsymbol{R},T\right)\Sigma^{>}\left(\mathbf{r}-\bar{\mathbf{r}},t-\bar{t},\boldsymbol{R},T\right)\right.\\
&\qquad\left.-g^{>}\left(\mathbf{r},t,\boldsymbol{R},T\right)\Sigma^{<}\left(\mathbf{r}-\bar{\mathbf{r}},t-\bar{t},\boldsymbol{R},T\right)\right],
\end{aligned}\tag{5.35}$$

where we define averaged space and time coordinates, which is defined as

$$R=\frac{r_1+r_1'}{2},\quad T=\frac{t_1+t_1'}{2}\tag{5.36}$$

$$r=r_1-r_1',\quad t=t_1-t_1'.\tag{5.37}$$

The Fourier transformed form of the eq(5.35) is,

$$\begin{aligned}
&\left(\frac{\partial}{\partial T}+\nabla_{\mathbf{p}}\varepsilon_0\left(\mathbf{p}\right)\cdot\nabla_{\mathbf{R}}-\nabla_{\mathbf{R}}U_{\text{eff}}\left(\boldsymbol{R},T\right)\cdot\nabla_{\mathbf{p}}+\frac{\partial U_{\text{eff}}}{\partial t}\frac{\partial}{\partial\omega}\right)g^{<}_{\alpha\beta}\left(\mathbf{p},\omega\right)_{\mathbf{R},T}\\
&=\left\{-g^{<}_{\alpha\beta}\left(\mathbf{p},\omega\right)_{\mathbf{R},T}\Sigma^{>}_{\alpha\beta}\left(\mathbf{p},\omega\right)_{\mathbf{R},T}+g^{>}_{\alpha\beta}\left(\mathbf{p},\omega\right)_{\mathbf{R},T}\Sigma^{<}_{\alpha\beta}\left(\mathbf{p},\omega\right)_{\mathbf{R},T}\right\}
\end{aligned}\tag{5.38}$$

where $g_{\alpha\beta}\left(\mathbf{p},\omega\right)$ is the Fourier transform of

$$g_{\alpha\beta}\left(\mathbf{1},\mathbf{1}'\right)=\frac{1}{i}<\boldsymbol{T}\left(\psi(\mathbf{1})\psi^{\dagger}(\mathbf{1}')\right)>_{\alpha\beta}\tag{5.39}$$

$$g^{>}_{\alpha\beta}\left(\mathbf{1},\mathbf{1}'\right)=\frac{1}{i}<\left(\psi(\mathbf{1})\psi^{\dagger}(\mathbf{1}')\right)>_{\alpha\beta}\tag{5.40}$$

$$g^{<}_{\alpha\beta}\left(\mathbf{1},\mathbf{1}'\right)=-\frac{1}{i}<\left(\psi^{\dagger}(\mathbf{1}')\psi(\mathbf{1})\right)>_{\alpha\beta}\tag{5.41}$$

and $\Sigma^{>}$and $\Sigma^{<}$ is given by

$$\begin{aligned}
&\Sigma^{>,<}_{\alpha\beta}\left(\mathbf{p},\omega\right)\\
&=\int_{\mathbf{p}_1,\omega_1}\int_{\mathbf{p}_2,\omega_2}\int_{\mathbf{p}_3,\omega_3}\left(2\pi\right)^{d+1}\delta\left(\mathbf{p}+\mathbf{p}_1-\mathbf{p}_2-\mathbf{p}_3\right)\delta\left(\omega+\omega_1-\omega_2-\omega_3\right)\\
&\times\left[V\left(\mathbf{p}-\mathbf{p}_2\right)V\left(\mathbf{p}-\mathbf{p}_2\right)g^{<,>}_{\gamma\delta}(\mathbf{p}_1,\omega_1)g^{>,<}_{\alpha\beta}(\mathbf{p}_2,\omega_2)g^{>,<}_{\delta\gamma}(\mathbf{p}_3,\omega_3)\right.\\
&\quad\left.-V\left(\mathbf{p}-\mathbf{p}_2\right)V\left(\mathbf{p}-\mathbf{p}_3\right)g^{<,>}_{\gamma\delta}(\mathbf{p}_1,\omega_1)g^{>,<}_{\alpha\gamma}(\mathbf{p}_2,\omega_2)g^{>,<}_{\delta\beta}(\mathbf{p}_3,\omega_3)\right]
\end{aligned}\tag{5.42}$$

for spinor basis.

We change the symbol $T\to t$ since we are only interested in the overall behavior of the fluid, and T denotes temperature for later parts. We define the velocity of quasiparticle fluid at $\mathbf{R},t$ as $\mathbf{v_k}=\nabla_{\mathbf{p}}E_0\left(\mathbf{p}\right)$.

5.2.3 Boltzmann equation

One can subtract the corresponding equation of the Eq (5.38) for $g^{>}$ from the Eq (5.38) itself. Then, we obtain $\Box a(\mathbf{p},\omega) = 0$ where the operator $\Box$ implies the derivatives applied to the left hand side of Eq (5.38), and we defined $a(\mathbf{p},\omega) = g^{<}(\mathbf{p},\omega) \mp g^{>}(\mathbf{p},\omega)$, which is a spectral function. $a(\mathbf{p},\omega)$ is some function of $(\omega - K - U_{\text{eff}})$ where K is energy of the single particle with momentum $\mathbf{p}$. Unfortunately, $a(\mathbf{p},\omega)$ is not directly related to the spectral function of imaginary time Green's function $A(\mathbf{p},\omega)$. However, we can complete exact correspondence later and employ the simplest configuration $a(\mathbf{p},\omega) = 2\pi\delta(\omega - \varepsilon_{\mathbf{p}})$ (which is similar with the spectral function of Hartree result of G). With the simple assumption that the spectral function has a peak at the energy of the particle, $A_{\alpha\beta}(k,\omega) = 2\pi\delta(\omega - \varepsilon_{\lambda}(k,t))\,\delta_{\alpha\beta}$, we get

$$g^{<}_{\alpha\beta}(\mathbf{p},\omega) = 2\pi\delta(\omega - \varepsilon_{\lambda}(k,t))\, f_{\lambda}(k,t)\,\delta_{\lambda\lambda'} \tag{5.43}$$

$$g^{>}_{\alpha\beta}(\mathbf{p},\omega) = 2\pi\delta(\omega - \varepsilon_{\lambda}(k,t))\,(1 - f_{\lambda}(k,t))\,\delta_{\lambda\lambda'} \tag{5.44}$$

where $f_{\lambda}(k,t)$ is the Fermi distribution function in equilibrium state. Thus, the eq (5.38) reduces into

$$\begin{aligned}
&\left(\frac{\partial}{\partial t} + \mathbf{v}_{\lambda,\mathbf{k}} \cdot \nabla_{\mathbf{R}} - \nabla_{\mathbf{R}} U_{\text{ext}}(\boldsymbol{R},t) \cdot \nabla_{\mathbf{k}}\right) f_{\lambda}(k,t) \\
&= -f_{\lambda}(k,t)\left(\bar{\Sigma}^{>}_{\lambda,\lambda}(k,t)\right)_{\omega=\varepsilon_{\lambda}} + (1 - f_{\lambda}(k,t))\left(\bar{\Sigma}^{<}_{\lambda,\lambda}(k,t)\right)_{\omega=\varepsilon_{\lambda}},
\end{aligned} \tag{5.45}$$

with

$$\begin{aligned}
&\left(\bar{\Sigma}^{>}_{\lambda,\lambda}\right)_{\omega=\varepsilon_{\lambda}} \\
&= \int_{\mathbf{k}_1}\int_{\mathbf{k}_2}\int_{\mathbf{k}_3} (2\pi)^4\,\delta(\mathbf{p} + \mathbf{p}_1 - \mathbf{p}_2 - \mathbf{p}_3)\,\delta(\varepsilon_{\lambda,k} + \varepsilon_{\lambda_1,k_1} - \varepsilon_{\lambda_2,k_2} - \varepsilon_{\lambda_3,k_3}) \\
&\times [NV(\mathbf{k} - \mathbf{k}_2)\,V(\mathbf{k} - \mathbf{k}_2)\,M_{\lambda_3\lambda_1}M_{\lambda_1\lambda_3}M_{\lambda\lambda_2}M_{\lambda_2\lambda}f_{\lambda_1}(1 - f_{\lambda_2})(1 - f_{\lambda_3}) \\
&- V(\mathbf{k} - \mathbf{k_2})\,V(\mathbf{k} - \mathbf{k_3})\,M_{\lambda\lambda_2}M_{\lambda_2\lambda_1}M_{\lambda_1\lambda_3}M_{\lambda_3\lambda}f_{\lambda_1}(1 - f_{\lambda_2})(1 - f_{\lambda_3})] \\
&\left(\bar{\Sigma}^{>}_{\lambda,\lambda}\right)_{\omega=\varepsilon_{\lambda}} = \{f \leftrightarrow 1 - f\},
\end{aligned} \tag{5.46}$$

where M is some unitary matrix that transform the spinor basis into quasiparticle basis. The Eq (5.45) above reproduces a form of the classical Boltzmann equation for transport properties. Inconsistency of $a(\mathbf{p},\omega)$ we mentioned above can be solved with the generalized Boltzmann equation obtained by including all contribution from (5.35) to (5.38). Here, only final result is addressed[4].

$$\left[\omega - \varepsilon^{(0)}_{\mathbf{p}} - U_{\text{eff}} - \text{Re}\bar{\Sigma}, g^{<}\right] + \left[\text{Re}g, \Sigma^{<}\right] = -\Sigma^{>}g^{<} + \Sigma^{<}g^{>} \tag{5.47}$$

$$\bar{\Sigma} = \int \frac{d\omega'}{2\pi}\frac{\Sigma^{>} \mp \Sigma^{<}}{\omega - \omega'} \tag{5.48}$$

[4]One can find a full derivation in Ref [167]

$$g = \int \frac{d\omega'}{2\pi} \frac{g^{>} \mp g^{<}}{\omega - \omega'} \tag{5.49}$$

where the bracket $[X, Y]$ denotes Poisson bracket

$$[X, Y] = \frac{\partial X}{\partial \omega}\frac{\partial Y}{\partial T} - \frac{\partial X}{\partial T}\frac{\partial Y}{\partial \omega} - \nabla_{\mathbf{p}} X \cdot \nabla_{\mathbf{R}} Y + \nabla_{\mathbf{R}} X \cdot \nabla_{\mathbf{p}} Y. \tag{5.50}$$

We don't have to worry too much about the equation above because Eq (5.45) works with $f_{\mathbf{p}}$ equals to local occupation number in fermionic system at low temperature. In equilibrium at zero temperature, all states with ω less than chemical potential μ are occupied and empty otherwise. We assume $f_{\mathbf{p}}$ to be similar when $g^{<}(\mathbf{p}, \omega)_{\mathbf{R},T} = a(\mathbf{p}, \omega)_{\mathbf{R},T} f(\mathbf{p}, \omega)_{\mathbf{R},T}$, even in the presence of a disturbance. That means there is chemical potential $\mu_{\mathbf{R},T}$ such that

$$f = 0 \quad \text{for } \omega > \mu \tag{5.51}$$

$$1 - f = 0 \quad \text{for } \omega < \mu. \tag{5.52}$$

In nonequilibrium case, when ω near μ, both $\Sigma^{>}$ and $\Sigma^{<}$ are small, and $\Gamma = \Sigma^{>} + \Sigma^{<} \to 0$. The solution for $a(\mathbf{p}, \omega)_{\mathbf{R},T}$ from eq(5.47) is

$$a(\mathbf{p}, \omega)_{\mathbf{R},T} = \frac{\Gamma}{\mathrm{Re} g^{-1} + \Gamma/2} \tag{5.53}$$

$$\mathrm{Re} g^{-1} = \omega - \varepsilon^{(0)}_{\mathbf{p}} - U - \mathrm{Re}\bar{\Sigma}, \tag{5.54}$$

and thus

$$a(\mathbf{p}, \omega)_{\mathbf{R},T} = 2\pi\delta\left(\omega - \varepsilon^{(0)}_{\mathbf{p}} - U - \mathrm{Re}\bar{\Sigma}\right). \tag{5.55}$$

The root is $\omega = \varepsilon(\mathbf{p}, \omega)_{\mathbf{R},T} + U(\boldsymbol{R}, T)$ where $\varepsilon(\mathbf{p}, \omega)_{\mathbf{R},T} = \varepsilon^{(0)}_{\mathbf{p}} + \mathrm{Re}\bar{\Sigma}(\mathbf{p}, \omega)_{\mathbf{R},T}$. In equilibrium state, $\varepsilon_{\mathbf{p}}(\mathbf{p}, \omega)_{\mathbf{R},T} = \varepsilon_{\mathbf{p}}$ which is non-local and $\mu = \varepsilon(p_F)$ where p_F is called Fermi momentum. As a result, the left and side of eq (5.47) become

$$2\pi\delta\left(\omega - \varepsilon(\mathbf{p}, \omega)_{\mathbf{R},T} - U(\boldsymbol{R}, T)\right)\left[\frac{\partial n}{\partial T} + \nabla_{\mathbf{p}}\varepsilon \cdot \nabla_{\boldsymbol{R}} n - \nabla_{\boldsymbol{R}}(\varepsilon + U) \cdot \nabla_{\mathbf{p}} n\right] \tag{5.56}$$

where we defined $n(\mathbf{p}, \boldsymbol{R}, T) = f(\mathbf{p}, \omega)_{\mathbf{R},T}|_{\omega=\varepsilon+U}$ as the density of quasi-particles with momentum $\mathbf{p}$ at the space-time $(\boldsymbol{R}, T)$. The delta function will be integrated with the one on the right hand side, and the equation is consistent with the Boltzmann equation.

5.3 Background and graphene

Although the flow of electrons in a conductor is expected to obey the laws of hydrodynamics under certain circumstances [152], hydrodynamic behavior for electrons in solids has been only recently experimentally observed [153]. Why is it difficult to implement electron hydrodynamics in a laboratory experiment? As briefly mentioned in the introduction, the hydrodynamic regime

can be realized when the frequency of electron-electron collisions is much larger than the rates of electron-phonon and electron-impurity scattering. In a typical lattice system, the elastic impurity scattering dominates electronic transport at low temperatures, whereas the leading mechanism is the electron-phonon scattering at high temperatures. Hydrodynamic behavior hence requires extremely clean samples because the collisions between electrons can dominate only if the impurity scattering time is much longer the time of collision between particles. A fascinating experimental realizations of hydrodynamic behavior has been achieved in graphene [146]. Graphene is an excellent material for the observation of hydrodynamic flow of electrons because of its very high carrier mobility, high sample quality, and the presence of massless 2D Dirac fermions, which suppresses screening effects. As a two band semimetal, the fluid emerges in the graphene is composed of two species of carriers with opposite charges – electrons and holes.

5.3.1 Conductivity

The graphene conductivity as a hydrodynamic response of the fluid to a specially uniform electrical field has been well studied by Kashuba [169] and Fritz *et al* [168]. We assume the electron distribution is spatially homogeneous to a reasonable approximation. Hence, the Boltzmann equation for the conductivity has no term of $\mathbf{v} \cdot \nabla_{\mathbf{R}}$. Also, the term in the Boltzmann equation due to the change in the average energy particle at $(\mathbf{R}, T)$ caused by the time variation of the potential field is assumed to be zero as the electrical field varies slowly. The quantum Boltzmann equation (5.45) should be rewritten in particle-hole basis (equivalent to upper and lower band basis). We find unitary transformation of basis from sublattice basis to low-energy band basis:

$$U_{\mathbf{k}} = \frac{1}{\sqrt{2}} \begin{pmatrix} 1 & 1 \\ K/k & -K/k \end{pmatrix} \tag{5.57}$$

where $K = k_x + ik_y$, $k = |K| = \sqrt{(k_x)^2 + (k_y)^2}$. The low-energy Hamiltonian of graphene is diagonalized by $U_{\mathbf{k}}$ such as

$$U_{\mathbf{k}}^{-1} H_0 U_{\mathbf{k}} = v_F U_{\mathbf{k}}^{-1} \begin{pmatrix} 0 & K^* \\ K & 0 \end{pmatrix} U_{\mathbf{k}} = v_F \begin{pmatrix} k & 0 \\ 0 & -k \end{pmatrix} \tag{5.58}$$

$$E_\lambda(k) = \lambda v_F k. \tag{5.59}$$

With this transformation, we define the green's function in quasiparticle basis $g^<_{\lambda,\lambda'}$ as

$$g^<_{\lambda,\lambda'} = 2\pi\delta\left(\omega - \varepsilon_\lambda(k,t)\right) f_\lambda(k,t)\, \delta_{\lambda\lambda'} \tag{5.60}$$

$$g^>_{\lambda,\lambda'} = 2\pi\delta\left(\omega - \varepsilon_\lambda(k,t)\right) \left(1 - f_\lambda(k,t)\right) \delta_{\lambda\lambda'}, \tag{5.61}$$

where $f_\lambda(k,t)$ denotes the nonequilibrium distribution function of two particle species (quasiparticle and quasihole). From Eq (5.45) and (5.46), Boltzmann equation for conductivity is:

$$\left(\frac{\partial}{\partial t}+F_{\text{ext}}\cdot\nabla_{\mathbf{k}}\right)f_\lambda(\mathbf{k},t)=I_{\text{col}} \tag{5.62}$$

where

$$\begin{aligned}I_{\text{col}}=-\frac{1}{2}\int\frac{d^2k_1}{(2\pi)^2}\frac{d^2q}{(2\pi)^2}\frac{2\pi}{v_F}\delta\left(\lambda k+\lambda_1k_1-\lambda_2\left|\mathbf{k}+\mathbf{q}\right|-\lambda\left|\mathbf{k}_1-\mathbf{q}\right|\right)\\ \times\left[NV(-\mathbf{q})V(-\mathbf{q})M_{\lambda_3\lambda_1}M_{\lambda_1\lambda_3}M_{\lambda\lambda_2}M_{\lambda_2\lambda}\right.\\ \left.-V(-\mathbf{q})V(\mathbf{k}-\mathbf{k_1}+\mathbf{q})M_{\lambda_1\lambda_3}M_{\lambda_2\lambda_1}M_{\lambda\lambda_2}M_{\lambda_3\lambda}\right]\\ \times\left[f_\lambda f_{\lambda_1}(1-f_{\lambda_2})(1-f_{\lambda_3})-(1-f_\lambda)(1-f_{\lambda_1})f_{\lambda_2}f_{\lambda_3}\right]\end{aligned} \tag{5.63}$$

is the collision term. $F_{\text{ext}}=e\mathbf{E}$ is the external electric force, $\mathbf{q}\equiv\mathbf{k_2}-\mathbf{k}$, and momentum conservation is applied for integration over $\mathbf{k}_2=\mathbf{k}+\mathbf{q}$ and $\mathbf{k_3}=\mathbf{k}_1-\mathbf{q}$. The M matrices are defined as

$$\begin{aligned}M_{\lambda\lambda_1}(\mathbf{k},\mathbf{k_1})\equiv\left[U_{\mathbf{k}}^{-1}U_{\mathbf{k_1}}\right]_{\lambda\lambda_1}&=\frac{1}{2}\begin{pmatrix}1+\frac{K^*K_1}{kk_1} & 1-\frac{K^*K_1}{kk_1}\\ 1-\frac{K^*K_1}{kk_1} & 1+\frac{K^*K_1}{kk_1}\end{pmatrix}_{\lambda\lambda_1}\\ &=\frac{1}{2}\left(1+\lambda\lambda_1\frac{K^*K_1}{kk_1}\right).\end{aligned} \tag{5.64}$$

One can notice the four M components imply corresponding diagrams of the Born approximation.

One assumes the distribution of particles driven out of equilibrium has a term which is linear to the external source. In equilibrium, the distribution is merely fermi distribution $f^{(0)}(k)$:

$$f^{(0)}(k)=\frac{1}{e^{(\lambda v_Fk)\beta}+1} \tag{5.65}$$

where $\beta=1/(k_BT)$. For conductivity, the force from external electrical field gives the first order nonequilibrium distribution function. Since $F_{\text{ext}}\cdot\nabla_{\mathbf{k}}f^{(0)}(k)=\beta e\mathbf{E}(t)\cdot\mathbf{v}_{\lambda,\mathbf{k}}$, we can reasonably define $f_\lambda(k,t)$ as

$$f_\lambda(k,t)=f^{(0)}(k)+\beta f_\lambda^{(0)}\left(1-f_\lambda^0\right)eE_i(t)\left(\mathbf{v}_{\mathbf{k}}\right)_i\chi_\lambda(k,t) \tag{5.66}$$

where $\chi_\lambda(k,t)$ is unknown function of k. The velocity $\mathbf{v}_{\lambda,\mathbf{k}}$ is, by definition,

$$\mathbf{v}_{\lambda,\mathbf{k}}=\nabla_{\mathbf{k}}\varepsilon^0(k)=\nabla_{\mathbf{k}}\lambda v_Fk=\lambda v_F\frac{\mathbf{k}}{k}=\lambda\mathbf{v}_{\mathbf{k}} \tag{5.67}$$

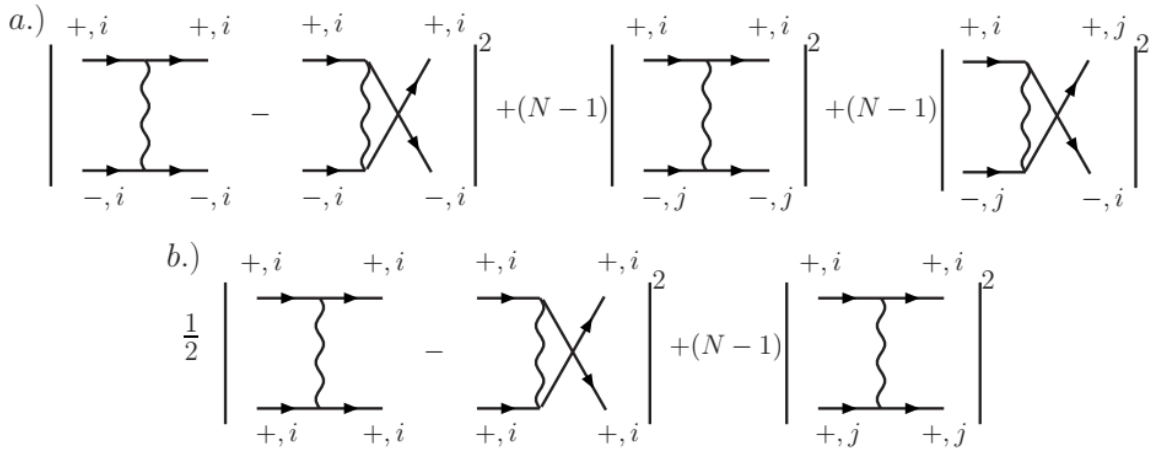

Figure 5.1: Illustration of the golden rule diagrams for (a) R_1 and (b) R_2 part of collision integral. The vertex preserves the flavor $a = i, j$, which means there is no spin or valley exchange [168].

With the equation (5.62) and (5.66), we find the linearized Boltzmann equation (see Appendix C):

$$\begin{aligned}
&\left(-i\omega\chi_\lambda\left(\beta,\varepsilon_k,\omega\right)-1\right)\lambda v_F\frac{\mathbf{k}}{k}f_\lambda^{(0)}\left(1-f_\lambda^{(0)}\right)\\
&\quad=-\int\frac{d^2k_1}{\left(2\pi\right)^2}\frac{d^2q}{\left(2\pi\right)^2}\frac{2\pi}{v_F}\delta\left(\lambda\left|\mathbf{k}\right|+\lambda_1\left|\mathbf{k}_1\right|-\lambda_2\left|\mathbf{k}+\mathbf{q}\right|-\lambda_3\left|\mathbf{k}_1-\mathbf{q}\right|\right)\\
&\qquad\times\mathcal{M}^{\mathrm{Col}}_{\lambda\lambda_1\lambda_2\lambda_3}f^{(0)}_{-\lambda}f^{(0)}_{-\lambda_1}f^{(0)}_{\lambda_2}f^{(0)}_{\lambda_3}v_F\left[\frac{\mathbf{k}}{k}g_\lambda\left(k,\omega\right)+\frac{\mathbf{k_1}}{k_1}g_{\lambda_1}\left(k_1,\omega\right)\right.\\
&\qquad\left.-\frac{\mathbf{k}+\mathbf{q}}{\left|\mathbf{k}+\mathbf{q}\right|}g_{\lambda_2}\left(\left|\mathbf{k}+\mathbf{q}\right|,\omega\right)-\frac{\mathbf{k_1}-\mathbf{q}}{\left|\mathbf{k}_1-\mathbf{q}\right|}g_{\lambda_3}\left(\left|\mathbf{k}_1-\mathbf{q}\right|,\omega\right)\right],
\end{aligned}\tag{5.68}$$

where we have performed a Fourier transform from time domain to frequency domain ω, and $\chi_i\left(\lambda,k\right)\equiv v_F\frac{\mathbf{k}}{k}\chi_\lambda\left(k,\omega\right)$. To simplify the equation, Fritz referred to publications by Sachdev[170, 171] and applied only three combination of λs; $(\lambda,\lambda_1,\lambda_2,\lambda_3)=(\lambda,-\lambda,\lambda,-\lambda)$, $(\lambda,-\lambda,-\lambda,\lambda)$, and $(\lambda,\lambda,\lambda,\lambda)$. Those imply the number of quasiparticles/quasiholes are conserved during collision process. The first two configurations describe scattering between two oppositely charged particles while the last describes collisions between like charges. As a result, the collision part is divided into two part, namely R_1 part and R_2 part. Corresponding schematic diagrams for each term are shown in Fig 5.1.

Instead of working the complete set of eigenfunctions of collision operator and use the variational method to find the eigenfunctions of χ. In the collinear regime, one can identify the eigenfunctions of collision operator (zero modes), which gives zero eigenvalues by some conservation laws. For example, $\chi_{\lambda,k}=\lambda\chi\left(\omega\right)$ is a zero mode by the conservation of the number of chirality. However, the modes which are symmetric under $\lambda\to-\lambda$ don't contribute to the electrical current because of particle hole symmetry. Also, $\chi_{\lambda,k}=\lambda k\chi\left(\omega\right)$ zero mode arise from momentum conservation annihilates collision terms even in non-collinear regime by momentum conservation. Thus, the biggest contribution to the conductivity comes from the mode $\chi_{\lambda,k}=\lambda\chi\left(\omega\right)$.

However, we now face the problem with the mode of χ which has a divergence in collinear limit. The logarithmic divergence in phase space occurs in collinear limit. Without loss of generality, one can define $\mathbf{k}$, $\mathbf{k_1}$, and $\mathbf{q}$ as

$$\mathbf{k} = (k, 0)\,, \quad \mathbf{k_1} = (k_1, k_\perp)\,, \quad \mathbf{q} = (q, q_\perp) \tag{5.69}$$

with $k > 0$ and both of $k_\perp$ and $q_\perp$ are small. With this approach, one can confirm the logarithmic divergence in $k_\perp \to 0$ limit from the delta function in (5.68) and find the integral gives a factor $2\ln(1/\alpha)$ in small perturbative α approach. It is valid as long as the leading correction of χ has a factor of $[\ln(1/\alpha)]^{-1}$. In the non-collinear regime, one can derive the solution of the equation (5.68),

$$f(\omega) = \frac{1}{-i(\omega/T) + \kappa\alpha^2} \tag{5.70}$$

where $\kappa \approx 3.646$.

Finally, electrical current can be expressed with a functional derivative of the action with respect to a vector potential $\mathbf{A}$. $\mathbf{A}$ is related to the external field by $E = -\partial A/\partial t$. As we introduced the low energy Hamiltonian in Eq (5.58), the system has particle-hole symmetry and the Hamiltonian is written in the transformed basis:

$$H_0 = \sum_{\lambda,a} \int_{\mathbf{k}} \lambda v_F k \gamma^\dagger_{\lambda,a}(\mathbf{k})\, \gamma_{\lambda,a}(\mathbf{k}) \tag{5.71}$$

where λ goes over ± 1 and index a indicates the different flavors[5] of fermions. For a spatially independent current, the current operator is

$$\mathbf{J} = \mathbf{J}_1 + \mathbf{J}_2 \tag{5.72}$$

$$\mathbf{J}_1 = e \sum_{\lambda,a} \int_{\mathbf{k}} \lambda \frac{\mathbf{k}}{k} \gamma^\dagger_{\lambda,a}(\mathbf{k})\, \gamma_{\lambda,a}(\mathbf{k}) \tag{5.73}$$

$$\mathbf{J}_2 = -iev_F \int_{\mathbf{k}} \frac{\hat{\mathbf{z}} \times \mathbf{k}}{k} \left[\gamma^\dagger_{+,a}(\mathbf{k})\, \gamma_{-,a}(\mathbf{k}) - \gamma^\dagger_{-,a}(\mathbf{k})\, \gamma_{+,a}(\mathbf{k})\right] \tag{5.74}$$

where $\mathbf{J}_1$ measures the current carried by the quasiparticles and quasiholes which are indicated with λ. $\mathbf{J}_2$ operator creates a quasiparticle-quasihole pair and does not contribute to the collision dominated transport. Within the first type current, the average value can be expressed with the distribution function of quasiparticle $f_\lambda(\mathbf{k}, t) = \left\langle \gamma^\dagger_{\lambda,a}(\mathbf{k})\, \gamma_{\lambda,a}(\mathbf{k}) \right\rangle$,

$$\langle \mathbf{J}_1 \rangle = e \sum_{\lambda,a} \int_{\mathbf{k}} \mathbf{v}_{\lambda,\mathbf{k}} f_\lambda(\mathbf{k}, t)\,. \tag{5.75}$$

One can find conductivity from the current carried by nonequilibrium quasiparticles (or quasiholes)

[5] The word "flavor" is simply for distinguishing particles or quasiparticles which have identical charge and properties after the transformation. For example, spin and valley in the graphene gives four copies of 2×2 Hamiltonian.

with $\delta f_\lambda(k,t)$ at (5.66) and (5.70):

$$\sigma(\omega) = \frac{e^2}{h}\frac{Nk_BT\ln 2}{-i\hbar\omega + \kappa k_BT\alpha^2}. \tag{5.76}$$

Spin and valley degeneracy N is four. One can note that the frequency independent conductivity depends only upon $\alpha(T)$. This result can be qualitatively understood by inserting lifetime τ into the expression of the conductivity given by Wallace [172],

$$\sigma = \frac{N_{\text{eff}}e^2}{m_{\text{eff}}}\tau = \frac{Ae^2}{h}\hbar^{-1}\tau k_BT \tag{5.77}$$

with the inelastic relaxation rate $\hbar\tau^{-1} = \kappa k_BT\alpha^2$. The temperature dependence of the inelastic relaxation time $\tau \propto \beta$ can be also predicted from comparing Boltzmann equation with the transport lifetime [173]

$$\frac{\partial f}{\partial t} + \nabla_r f\cdot\mathbf{v} + \frac{1}{\hbar}\nabla_k f\cdot[e\mathbf{E} + \mathbf{v}\times\mathbf{B}] + \frac{\delta f}{\tau} = 0 \tag{5.78}$$

with Eq (5.62) and (5.63).

5.3.2 Shear viscosity

Classically, the viscosity is a dissipative response of a fluid to strain forces. The viscosity describes the effect of energy dissipation in a fluid due to internal friction. Viscous phenomenon can be observed when different particles of the fluid move with different velocities. The simplest setup to observe this is flow through a confined channel[6]. More intuitively, suppose the fluid is filled between two plates. If one of the plates moves stably for a long time, a velocity gradient $\partial u/\partial x$ is exhibited in the fluid due to these boundary conditions. In this system, the stronger shear stress $\tau = F/A$ acting on the moving plate is the more viscous the fluid is.

In order to define viscosity in the context of fluid mechanics [175], let us consider the equation of continuity and the equation of motion (Euler's equation) for ideal fluids.

$$\frac{\partial\rho}{\partial t} + \frac{\partial(\rho v_k)}{\partial x_k} = 0 \tag{5.79}$$

$$\frac{\partial u_i}{\partial t} = -v_k\frac{\partial u_k}{\partial x_k} - \frac{1}{\rho}\frac{\partial p}{\partial x_k} \tag{5.80}$$

Then, we obtain

$$\frac{\partial}{\partial t}(\rho u_i) = -\frac{\partial\Pi_{ik}}{\partial x_k}, \tag{5.81}$$

where ρ is the density of the fluid with the velocity u, and $\Pi_{ik} = P\delta_{ik} + \rho u_i u_k$ is the momentum flux density tensor. The indices i,k denote the spatial components. In such ideal fluids, the momentum flux density tensor has terms with thermodynamic pressure and two velocity weighted by fluid density. So far, it represent a completely reversible momentum transfer. Once internal friction

[6]For electron, one can find the experiment which shows viscous electron flow in [174]

(viscosity) is taken into account, it cause irreversible transfer of momentum from high velocity regime to low velocity regime. We define additional term $-T'_{ik}$ which is called viscous stress tensor, and the term should depends on the spacial gradient of the velocity field $\partial u/\partial x$. Assuming the velocity difference to be small, the viscous stress tensor can be written as the linear combination of $\partial u_k/\partial x_i$. In the most general form,

$$T'_{ij} = \eta_{ijk\ell}\frac{\partial u_k}{\partial x_\ell} \tag{5.82}$$

where $\eta_{ijk\ell}$ is called coefficient of viscosity.

Analogously, there has been studies about viscous response of the electronic system to a strain field. One can define the viscosity coefficients describing the relaxation of a deviation of the momentum density from its equilibrium (possibly only local) value in [176]. In momentum conserved system, the continuity equation for momentum is

$$\frac{\partial \zeta_j(\mathbf{x},t)}{\partial t} + \partial_i \tau_{ij}(\mathbf{x},t) = 0 \tag{5.83}$$

where $\zeta_j(x,t)$ is the momentum density at space&time x,t. Indices i, j refer to space components in d dimension. The stress tensor operator τ_{ij} plays an important role in the transport of viscous quantum fluids. It is composed of pressure, direct momentum flux $m\bar{n}v_iv_j$, and viscous stress tensor $-\tau'_{ij}$. The pressure corresponds to the diagonal part of the stress tensor. The viscous stress tensor $\tau'_{\mu\nu}$ can be defined as the expectation of the stress tensor due to strain. In non-equilibrium systems, the deviation in the average stress tensor $-\langle\tau'_{\mu\nu}\rangle$ should depends on strain tensor and its time derivative in linear response as we defined in (4.18),

$$\langle\tau'_{ij}\rangle = \lambda_{ijk\ell}\xi_{k\ell} + \eta_{ijk\ell}\frac{\partial\xi_{k\ell}}{\partial t} \tag{5.84}$$

The viscosity tensor $\eta_{\mu\nu\alpha\beta}$ is separated into symmetric part $\eta^S_{ijk\ell}$, namely *shear viscosity,* and antisymmetric part $\eta^A_{ijk\ell}$, namely *Hall viscosity.* $\eta^A_{ijk\ell}$ can only be nonzero when time reversal symmetry is broken. Sometimes, the viscosity $\eta_{ijk\ell}$ with the component $i=j$ is called *bulk viscosity.* What we are interested in this chapter is the shear viscosity. Comparing classical (5.82) and quantum fluids (5.84), we find an analogous relation between the gradients of velocity field $\vec{u}$ and the time derivative of the metric tensor ξ_{ij} [176]:

$$\frac{\partial u_i}{\partial x_j} = \frac{\partial\xi_{ij}}{\partial t}. \tag{5.85}$$

Thus, the shear viscosity can be obtained by the non-equilibrium stress tensor, which is linearized with respect to space derivative of average velocity $\vec{u}$.

As alluded in the introduction, the interest in the viscosity is related to the correspondence between strongly coupled field theories and classical gravitational theories, later called the anti-de Sitter/conformal field theory (AdS/CFT) correspondence [177–180]. Kovtun, Son and Starinets [181, 182] conjectured the existence of a lower bound on the ratio of the shear viscosity η and the

entropy density s for a wide class of condensed matter systems at finite temperature. Models close to this bound have been referred to as *perfect fluids*. The ratio η/s has been believed as a good indicator for the strength of interactions among the electrons. The physical picture for this ratio is following: the viscosity of a system is proportional to the transport mean free time of a quasi-particle τ and the energy density n_ϵ while the entropy density of the system is proportional to the particle density n and the Boltzmann constant k_B. Thus, the ratio τ/s is found to be $\tau/s \propto \tau n_\epsilon/nk_B$. Due to Heisenberg's uncertainty principle, the product of τ and n_ϵ/n cannot be smaller than $\hbar/2$. However, there are theoretical counter-examples to the bound [183–185]. The violation of the bound also can be found in some anisotropic Dirac fluids [186].

In order to find a effect on the Hamiltonian due to strain which is a linear transformation in the coordinates, we define the strain generator

$$\mathcal{J}_{ij} = -\frac{1}{2}\sum_n \left\{x_i^n, p_j^n\right\} \tag{5.86}$$

where n stands for particle indices. By following Bradlyn's approach [176] in zero magnetic filed case, additional Hamiltonian with the first order in $\xi_{\mu\nu}(t)$ can be shown to be (for details, see appendix D)

$$H_1 = -\frac{\partial \xi_{ij}}{\partial t}\mathcal{J}_{ij}. \tag{5.87}$$

As the next step, we have to relate the total strain generator $\mathcal{J}_{ij}$ to the energy-stress tensor $\langle\tau_{ij}\rangle$. The continuity equation of the momentum density in the absence of strain $g_i(\mathbf{x},t) = \frac{1}{2}\sum_n \left\{p_i^{(n)}, \delta\left(x_i - x_i^{(n)}\right)\right\}$ is

$$\partial_t g_i(\mathbf{x},t) = -\partial_j \tau_{ij}(\mathbf{x},t). \tag{5.88}$$

where $\tau_{ij}(\mathbf{x},t)$ is a stress tensor. In Fourier space,

$$\partial_t g_i(\mathbf{q},t) = -iq_j \tau_{ij}(\mathbf{q},t). \tag{5.89}$$

Upon expanding the momentum density for small momentum $\mathbf{q}$, we find $g_i(\mathbf{q},t)$ as

$$\begin{aligned} g_i(\mathbf{q},t) &= \int_{\mathbf{x}} e^{i\mathbf{q}\cdot\mathbf{x}} g_i(\mathbf{x},t) \\ &= g_i(0,t) + iq_j\frac{1}{2}\sum_n \left\{p_i^{(n)}, x_j^{(n)}\right\} + \cdots \end{aligned} \tag{5.90}$$

where $g_i(0,t)$ is the direct momentum. The additional term is given by

$$-\partial_t\left[iq_j\frac{1}{2}\left\{x_j, p_i\right\}\right] = \partial_t iq_j\mathcal{J}_{ij}. \tag{5.91}$$

To leading order in wave vector $\mathbf{q}$, the stress tensor is $\tau_{ij} = -P_i\delta_{ij} + \tau'_{ij}$ where $\mathbf{P}$ is pressure, and

τ'_{ij} is viscous stress tensor. Thus, absorbing $g_i(0,t)$ to the pressure, we find

$$\tau'_{ij}(\mathbf{q},t) = -\frac{\partial \mathcal{J}_{ij}}{\partial t}. \tag{5.92}$$

With the Hamiltonian of quasiparticle,

$$\begin{aligned}\tau'_{ij}(\mathbf{q},t) &= \sum_{\lambda,a}\int_{\mathbf{k}} \gamma^{\dagger}_{\lambda,a}(\mathbf{q})\,\lambda\frac{\partial}{\partial t}\left(-\mathcal{J}_{ij}\right)\gamma_{\lambda,a}(\mathbf{q}) \\ &= \sum_{\lambda,a}\int_{\mathbf{k}} \gamma^{\dagger}_{\lambda,a}(\mathbf{q})\,\frac{\lambda}{2}\frac{\partial}{\partial t}\left(x_\mu q_\nu + q_\nu x_\mu\right)\gamma_{\lambda,a}(\mathbf{q})\end{aligned} \tag{5.93}$$

and taking expectation, then

$$\langle \tau_{\mu\nu}\rangle = \sum_{\lambda,a}\int_{\mathbf{k}} \lambda v_\mu q_\nu \left\langle \gamma^{\dagger}_{\lambda,a}\gamma_{\lambda,a}\right\rangle = N\sum_{\lambda}\int_{\mathbf{k}} v_\mu q_\nu f_\lambda(k,t). \tag{5.94}$$

To determine the viscous tensor $\left\langle \tau'_{ij}\right\rangle$, we find an inhomogeneous flow field driving term derived from Boltzmann equation in which close to equilibrium.

$$\begin{aligned}\mathbf{v}_{\lambda,\mathbf{k}}\cdot\nabla_{\mathbf{x}} f_\lambda &= \beta f_\lambda(1-f_\lambda)\left(\mathbf{v}_{\lambda,\mathbf{k}}\right)_i k_j \frac{\partial u_j}{\partial x_i} \\ &= \beta f_\lambda(1-f_\lambda)\frac{\varepsilon_{\lambda,k}}{2\sqrt{2}} I_{ij}(\mathbf{k})\,X_{ij}\end{aligned} \tag{5.95}$$

where the second line of the equation above is written with the rotationally invariant spacial tensor and momentum tensor:

$$X_{ij} = \frac{\partial u_j}{\partial x_i} + \frac{\partial u_i}{\partial x_j} - \delta_{ij}\nabla\cdot\mathbf{u} \tag{5.96}$$

$$I_{ij}(\mathbf{k}) = \sqrt{2}\left(\frac{k_i k_j}{k^2} - \frac{1}{2}\delta_{ij}\right). \tag{5.97}$$

From the equation above, we employ an ansatz for the correction to the fermi distribution function in linear response as

$$\varepsilon_{\lambda,k} = \varepsilon^{(0)}_{\lambda,k} + \sum_{ij}\beta X_{ij}\chi_{ij}(\lambda,k,t) \tag{5.98}$$

Thus, the distribution function in linear response has the general form

$$f_\lambda(k,t) = f^0_\lambda + \beta f^0_\lambda\left(1-f^0_\lambda\right)X_{ij}\chi_{ij}(\lambda,k,t). \tag{5.99}$$

With the equation above, we can conduct a similar process with conductivity for the solution of linearized Boltzmann equation including variational method. Müller conducted a similar process and found the viscosity of the quasiparticle fluid in graphene with leading logarithmic approximation

[187],

$$\eta = C_\eta \frac{N\left(k_B T\right)^2}{4\hbar v^2 \alpha^2}\left[1 + \mathcal{O}\left(\frac{1}{\log \alpha}\right)\right] \tag{5.100}$$

where $C_\eta \approx 0.449$. Müller referred to the entropy density of noninteracting graphene, including renormalization effects [188] and found the ratio

$$\frac{\eta}{s} = \frac{\hbar}{k_B}\frac{C_\eta \pi}{9\zeta\left(3\right)\alpha^2\left(T\right)} \approx 0.00815 \times \left(\log \frac{T_\Lambda}{T}\right)^2. \tag{5.101}$$

This ratio grows when $T \to 0$ but only logarithmically grows since α is marginally irrelevant. The numerical prefactor make the value of the ratio small, and it approaches to the boundary. Low viscosity in graphene suggests the possibility of electronic turbulence and exhibit nearly perfect fluid.

5.4 Transport coefficients in NLSMs

In the wide class of three dimensional (3D) topological semimetals (TSMs), three possible states of matter, namely Dirac semimetal (DSM), Weyl semimetal (WSM) and nodeline semimetal (NLSM), have been widely studied recently. They are distinguished from each other by the degeneracy and dispersion of the nodal points (or line). The theoretical and experimental approach of those TSMs are well reviewed in [189]. Among them, NLSM has a distinct characteristic of nodes because the vanishing fermi surface forms a line, and if the line is circular and large enough, the system can be viewed as the extension of 2D nodal material with the larger momentum degree of freedom. In symmetric point of view, nodeline preserve both time reversal symmetry and inversion symmetry when spin-orbit coupling is neglected, thus, it is hard to observe topologically nontrivial phase. However, the transport properties in hydrodynamic regime has not been studied yet. The low-energy excitation of NLSM has an analogous dispersion with graphene but the Coulomb interaction and corresponding collision process are expected to convey the different behavior of hydrodynamic fluids from 2D graphene and 3D fermi liquid. In this chapter, we find transport coefficients, mainly, electrical conductivity and shear viscosity of 3D nodeline semimetals in hydrodynamic regime.

5.4.1 Boltzmann equation in NLSMs

We adopt the low energy Hamiltonian of a NLSM that is described by a circular nodal line in the $k_z = 0$ plane. The low energy quasiparticles are Dirac fermions located in the vicinity of the nodal line,

$$\begin{aligned}\mathcal{H}_0(\mathbf{k}) &= \frac{k_x^2 + k_y^2 - k_F^2}{2m}\sigma_x + v_z k_z \sigma_y \approx v_r \delta k_r \sigma_x + v_z k_z \sigma_y \\ &\equiv v_r\left(h_x \sigma_x + h_y \sigma_y\right)\end{aligned} \tag{5.102}$$

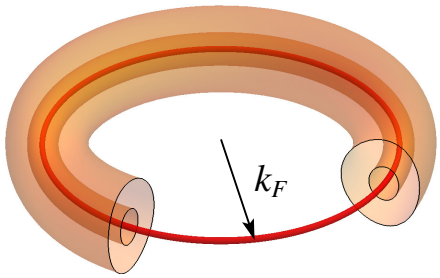

Figure 5.2: Fermi surface of a NLSM, with relativistic quasiparticles dispersing linearly away from a nodal line (red) with radius k_F. The toruses enclosing the nodal line are finite energy surfaces. The outer shell with energy Λ_T sets the untraviolet temperature cut-off of the theory.

where $\delta k_r = k_r - k_F$ is the in-plane momentum away from the nodal line, $v_F = k_F/m$ is the Fermi velocity in the radial direction and v_z along the the z direction. The quasiparticles interact through the 3D Coulomb potential $V(q) = 4\pi e^2/q^2$ and have a linear dispersion around the nodal line, up to logarithmic self-energy corrections [166]. We assumed $k_r \approx k_F >> q_r$, q_z when k_F indicates the radius of node ring on $k_z = 0$ plane. The energy of quasiparticle is

$$\varepsilon^{(0)}_{\lambda,k} = \lambda v_r \sqrt{(h_x)^2 + (h_y)^2} = \lambda v_r \left|\mathbf{h}\right|$$

where $\lambda = +1$ corresponds to a excited particle and $\lambda = -1$ to a excited hole.

The unitary transformation of low-energy basis which is analogous to (5.57) is defined as

$$U_{\mathbf{k}} = \frac{1}{\sqrt{2}} \begin{pmatrix} 1 & 1 \\ \mathsf{H}/h & -\mathsf{H}/h \end{pmatrix} \tag{5.103}$$

where $\mathsf{H} = h_x + ih_y$, $|\mathbf{h}| = |\mathsf{H}| = \sqrt{(h_x)^2 + (h_y)^2} = h$. Thus, the original low energy Hamiltonian in pseudospin basis

$$\mathcal{H}_0 = v_r \begin{pmatrix} 0 & \mathsf{H} \\ \mathsf{H}^* & 0 \end{pmatrix} \tag{5.104}$$

can be transformed to low-energy basis (right hand side), and the green's function $g_k^{>,<}$ should be also transformed as

$$U_k^{-1} \mathcal{H}_0 U_k = v_r \begin{pmatrix} h & 0 \\ 0 & -h \end{pmatrix} = \lambda v_r h. \tag{5.105}$$

Similar to the equation (5.45) and (5.46), we can derive the quantum Boltzmann equations,

$$\begin{aligned} &\left(\frac{\partial}{\partial t} + \mathbf{v}_{\lambda,\mathbf{k}} \cdot \nabla_R - \nabla_R U_{\text{eff}} \cdot \nabla_{\mathbf{k}}\right) f_\lambda(k,t) \\ &= -f_\lambda(k,t) \left(\bar{\Sigma}^{>}_{\lambda,\lambda}(k,t)\right)_{\omega=\varepsilon_\lambda} + (1 - f_\lambda(k,t)) \left(\bar{\Sigma}^{<}_{\lambda,\lambda}(k,t)\right)_{\omega=\varepsilon_\lambda} \end{aligned} \tag{5.106}$$

$$\left(\bar{\Sigma}^{>}_{\lambda,\lambda}\right)_{\omega=\varepsilon_\lambda} = \int_{\mathbf{k}_1}\int_{\mathbf{k}_2}\int_{\mathbf{k}_3} (2\pi)^4\,\delta\left(\mathbf{p}+\mathbf{p}_1-\mathbf{p}_2-\mathbf{p}_3\right)\delta\left(\varepsilon_{\lambda,k}+\varepsilon_{\lambda_1,k_1}-\varepsilon_{\lambda_2,k_2}-\varepsilon_{\lambda_3,k_3}\right)$$
$$\times\left[NV\left(\mathbf{k}-\mathbf{k}_2\right)V\left(\mathbf{k}-\mathbf{k}_2\right)M_{\lambda_3\lambda_1}M_{\lambda_1\lambda_3}M_{\lambda\lambda_2}M_{\lambda_2\lambda}f_{\lambda_1}\left(1-f_{\lambda_2}\right)\left(1-f_{\lambda_3}\right)\right.$$
$$\left.-V\left(\mathbf{k}-\mathbf{k_2}\right)V\left(\mathbf{k}-\mathbf{k_3}\right)M_{\lambda\lambda_2}M_{\lambda_2\lambda_1}M_{\lambda_1\lambda_3}M_{\lambda_3\lambda}f_{\lambda_1}\left(1-f_{\lambda_2}\right)\left(1-f_{\lambda_3}\right)\right] \tag{5.107}$$

$$\left(\bar{\Sigma}^{>}_{\lambda,\lambda}\right)_{\omega=\varepsilon_\lambda} = \{f\leftrightarrow 1-f\} \tag{5.108}$$

with

$$\mathcal{M}_{\lambda\lambda_1}\left(\mathbf{h},\mathbf{h}_1\right)\equiv\left[U_{\mathbf{h}}^{-1}U_{\mathbf{h}_1}\right]_{\lambda\lambda_1}=\frac{1}{2}\left(1+\lambda\lambda_1\frac{\mathsf{H}^*\mathsf{H}_1}{hh_1}\right), \tag{5.109}$$

It is convenient to use λ indices as ±1 for new basis. The velocity of quasiparticles in the Boltzmann equation is, by definition,

$$\begin{aligned}\mathbf{v}_{\lambda,\mathbf{k}} &= \frac{\partial\varepsilon_{\lambda,k}}{\partial k_i}\\ &= \frac{\lambda v_r}{|\mathbf{h}|}\left(h_x\frac{\partial h_x}{\partial k_x},h_x\frac{\partial h_x}{\partial k_y},h_y\frac{\partial h_y}{\partial k_z}\right).\end{aligned} \tag{5.110}$$

In the hydrodynamic regime, the particles interact with each other faster than they lose energy to the lattice. The electronic relaxation is driven by the collision between particles, leading to local thermalization. The out of equilibrium distribution function of the quasiparticles $f_\lambda(\mathbf{k},\mathbf{x},t)$ satisfies the Boltzmann equation

$$\left(\frac{\partial}{\partial t}+\mathbf{v}_{\lambda,\mathbf{k}}\cdot\nabla_{\mathbf{x}}+e\mathbf{E}\cdot\nabla_{\mathbf{k}}\right)f_\lambda=\mathcal{I}_{\mathrm{col}}[f_\lambda], \tag{5.111}$$

where $f^0_\lambda=[e^{\varepsilon^0_\lambda\beta}+1]^{-1}$ is the equilibrium Fermi distribution, which solves the Boltzmann equation in the absence of interactions ($I_{\mathrm{col}}=0$), $\beta=1/k_BT$ and $\delta f_\lambda\left(\mathbf{k},\mathbf{x},t\right)$ the non-equilibrium correction in linear response to an external perturbation such as electric field and strain. In general, $\mathcal{I}_{\mathrm{col}}\approx\delta f/\tau$, where τ is the scattering time between collisions.

5.4.2 Conductivity

If the system is spatially homogenous, the non-equilibrium current carried by the quasiparticles due to the presence of an external electric field is $\mathbf{J}=e\sum_{\lambda,a}\int_{\mathbf{k}}\mathbf{v}_{\lambda,\mathbf{k}}f_\lambda(\mathbf{k},\omega)$, with $\int_{\mathbf{k}}\equiv(2\pi)^{-3}\int\mathrm{d}^3k$. In linear response, where $J_i=\sigma_{ij}E_j$, the conductivity is

$$\sigma_{ij}(\omega,T)=e\sum_\lambda\int_{\mathbf{k}}(v_{\lambda,\mathbf{k}})_i\frac{\partial}{\partial E_j}\delta f_\lambda(\mathbf{k},\omega). \tag{5.112}$$

In leading order and close to equilibrium, the driving force term on the left hand side of (5.111) is $e\mathbf{E}\cdot\nabla_{\mathbf{k}}f_\lambda=e\mathbf{E}\cdot\boldsymbol{\phi}_\lambda(k)$, with $\phi_{\lambda,i}(k)\equiv\beta f^0_\lambda(1-f^0_\lambda)(v_{\lambda,\mathbf{k}})_i$. The non-equilibrium dispersion can be

written in the form

$$\varepsilon_{\lambda,k} = \varepsilon^0_{\lambda,k} + \frac{\partial \mathbf{k}}{\partial t} \cdot (\nabla_{\mathbf{k}} \varepsilon^0_{\lambda,k}) g_\lambda(\mathbf{k}, \omega),$$

with $g_\lambda(\mathbf{k}, \omega)$ some unknown function. With this Ansatz, the non-equilibrium correction of the distribution function assumes the form

$$\delta f_\lambda(\mathbf{k}) = \beta f^0_\lambda \left(1 - f^0_\lambda\right) e\mathbf{E}(\omega) \cdot \mathbf{v}_{\lambda,\mathbf{k}} g_\lambda(\mathbf{k}, \omega). \tag{5.113}$$

For convenience, we define $\chi_{\lambda,i} \equiv (v_{\lambda,\mathbf{k}})_i g_\lambda$. In the collision dominated regime $\omega \ll \tau^{-1}$, the linearized kinetic equation can be approximately expressed in terms of the collision operator as $\phi_{\lambda,i} = \mathcal{C}\chi_{\lambda,i}$, where

$$\begin{aligned}\mathcal{C}\chi_{\lambda,i} = \frac{1}{8} \sum_{\lambda_1\lambda_2\lambda_3} \int_{\mathbf{k}_1} \int_{\mathbf{k}_2} \int_{\mathbf{k}_3} (2\pi)^4 \delta^3(\mathbf{k} + \mathbf{k}_1 - \mathbf{k}_2 - \mathbf{k}_3) \delta\left(\varepsilon^0_{\lambda,k} + \varepsilon^0_{\lambda_1,k_1} - \varepsilon^0_{\lambda_2,k_2} - \varepsilon^0_{\lambda_3,k_3}\right) \\ \times \mathcal{M}^{\text{Col}}_{\lambda\lambda_1\lambda_2\lambda_3} f^0_\lambda f^0_{\lambda_1} f^0_{-\lambda_2} f^0_{-\lambda_3} \\ \times \left[\chi_{\lambda,i}(k) + \chi_{\lambda_1,i}(k_1) - \chi_{\lambda_2,i}(k_2) - \chi_{\lambda_3,i}(k_3)\right],\end{aligned} \tag{5.114}$$

with

$$\mathcal{M}^{\text{Col}}_{\lambda\lambda_1\lambda_2\lambda_3} = \left[NV(\mathbf{k} - \mathbf{k}_2)^2 W_{\lambda\lambda_1\lambda_2\lambda_3} - V(\mathbf{k} - \mathbf{k_2}) V(\mathbf{k} - \mathbf{k_3}) Q_{\lambda\lambda_1\lambda_2\lambda_3}\right],$$

and

$$\begin{aligned} W_{\lambda\lambda_1\lambda_2\lambda_3} &= M_{\lambda\lambda_2} M_{\lambda_2\lambda} M_{\lambda_3\lambda_1} M_{\lambda_1\lambda_3} \\ Q_{\lambda\lambda_1\lambda_2\lambda_3} &= M_{\lambda\lambda_2} M_{\lambda_1\lambda_3} M_{\lambda_3\lambda} M_{\lambda_2\lambda_1} \end{aligned}$$

the collision matrix element.

The solution of the Boltzmann equation requires inverting the collision operator $\mathcal{C}$, what is usually a challenging problem. The dominant contribution to the conductivity follows from the eigenfunctions of the collision operator with the lowest eigenvalues. In the collinear approximation, where the momenta of the quasiparticles point in the same direction, the momenta embedded in the definition of the velocities factor out in the integrand of $\mathcal{C}$, which is proportional to $\lambda g_\lambda(k) + \lambda_1 g_{\lambda_1}(k_1) - \lambda_2 g_{\lambda_2}(k_2) - \lambda_3 g_{\lambda_3}(k_3)$. The zero modes of the collision operator $\mathcal{C}\chi_{\lambda,i} = 0$ in this restricted phase space are $g_{1,\lambda}(k) = a^{(e)}(\omega)$, $g_{2,\lambda}(k) = a^{(\chi)}(\omega)\lambda$ and $g_{3,\lambda}(k) = a^{(p)}(\omega)\lambda|\mathbf{h}|$, corresponding to conservation of charge, chirality and momentum, respectively.

As pointed out before, in the absence of non-collinear processes, those zero modes would produce infinite conductivity. To account for non-collinear processes, we express the eigenfunctions of $\mathcal{C}$ with the lowest eigenvalues in a basis of zero modes of the collinear regime. We note that due to translational symmetry, the momentum zero mode is an exact eigenfunction of (5.114), as can be readily checked. It does not however contribute to the conductivity (5.112) due to particle-hole symmetry at the nodal line. For the same reason, the chiral modes do not contribute the the charge transport either. We are then left with the charge zero mode, $\chi_{\lambda,i}(k) = a^{(e)}(\omega)(\mathbf{v}_{\lambda,\mathbf{k}})_i$, which

provides the only contribution to the conductivity.

We next restore the frequency dependence of the Boltzmann equation, $\phi_{\lambda,i} = \mathcal{C}\chi_{\lambda,i} - i\omega g_\lambda \phi_{\lambda,i}$. In order to calculate the function $a^{(e)}(\omega)$, we define the inner product $(a_{\lambda,i}, b_{\lambda,i}) = \frac{1}{2}\sum_{\lambda,i}\int_{\mathbf{k}} a_{\lambda,i}(\mathbf{k}) b_{\lambda,i}(\mathbf{k})$ and set the variational functional

$$Q\left[a^{(e)}\right] \equiv (\chi_{\lambda,i}, \phi_{\lambda,i}) - \frac{1}{2}\left(\chi_{\lambda,i}, C\chi_{\lambda,i} - i\omega a^{(e)}\phi_{\lambda,i}\right), \tag{5.115}$$

which is to be minimized, $\partial Q/\partial a^{(e)} = 0$. The momentum integral is performed in the scattering channels that conserve the number of particles and holes, which are dominant processes. Those processes are indicated in tables 5.1 and 5.2. Combining this result with Eq. (5.111) and (5.113), we obtain the frequency dependent conductivity in the collision dominated regime

$$\sigma(\omega, T) = \frac{e^2}{h} k_F \frac{k_B T}{i\omega + v_r(T) k_F \alpha^2(T) c\,(\gamma, \alpha)}, \tag{5.116}$$

where $c\,(\gamma, \alpha)$ is a numerical factor, $\gamma = v_z/v_r$ and $\alpha = e^2/v_F$ is the bare fine structure constant. $c\,(\gamma, \alpha)$ can be derived from inverting the linearized Boltzmann equation and has a logarithmic divergence due to the phase space of the nodal line in the collinear regime. As in graphene, this divergence follows from the linearity of the electronic spectrum and can be regularized by self-energy corrections of the order of $\alpha\Lambda$,where Λ is some ultraviolet cut-off of the hydrodynamic regime, typically τ^{-1}. In that approximation, where all momenta are *nearly* collinear to each other, the coefficient that follows from inverting the collision operator is

$$c\,(\gamma = 1, \alpha) \approx 0.2\,\ln^3\left(\frac{1}{\alpha}\right). \tag{5.117}$$

This approximation overestimates this transport coefficient. Non-collinear processes are expected to smooth out the singular dependence of the coefficient with α.

In addition, as in graphene, the self-energy renormalizes the velocity of the quasiparticles, which diverges at low temperature, $v_r(T) = v_r[1 + C_1\alpha\ln(\Lambda_T/T)]$, with $\Lambda_T \ll v_F k_F$ the bare ultraviolet cutoff. The renormalization group (RG) also renormalizes the fine structure constant in the perturbative regime, $\alpha(T) = \alpha/[1 + (C_1 + C_2 v_F k_F/k_B\Lambda_T)\ln(\Lambda_T/T)]$, which flows logarithmically to zero at $T \to 0$ [166]. The constants $C_1 \approx 0.049$ and $C_2 \approx 1.3 \times 10^{-3}$ are defined by elliptic functions calculated at the fixed point $\alpha^* = 0$ and $\Lambda_T^* = 0$ [166]. Unlike in conventional relativistic theories, in NLSMs the scaling in the renormalization group (RG) flow is fixed by the radius of the Fermi surface k_F, rather than by the ultraviolet cut-off Λ_T, which flows towards zero. The combination $[\alpha v_F](T)$ therefore renormalizes towards a constant, whereas the ratio $\gamma \equiv v_z/v_F$ does not run. Hence, in the collison dominated regime $\omega \ll \tau^{-1}$, $\sigma(0, T) \propto T\ln(\Lambda_T/T)$ goes to zero in the $T \to 0$ limit, suggesting that the system behaves as an insulator. This result contrasts with the case of relativistic systems lacking a Fermi surface, such as graphene, where the collision dominated conductivity diverges logarithmically at zero temperature.

In the DC limit ($\omega \to 0$), the scattering time between collisions scales logarithmically with

	λ	λ_1	λ_2	λ_3	$W_{\lambda\lambda_1\lambda_2\lambda_3}$
#1	λ	λ	λ	λ	$\cos^2\left(\frac{\Theta-\Theta_2}{2}\right)\cos^2\left(\frac{\Theta_1-\Theta_3}{2}\right)$
#2	λ	$-\lambda$	λ	$-\lambda$	$\cos^2\left(\frac{\Theta-\Theta_2}{2}\right)\cos^2\left(\frac{\Theta_1-\Theta_3}{2}\right)$
#3	λ	$-\lambda$	$-\lambda$	λ	$\sin^2\left(\frac{\Theta-\Theta_2}{2}\right)\sin^2\left(\frac{\Theta_1-\Theta_3}{2}\right)$

Table 5.1: W tensors

	λ	λ_1	λ_2	λ_3	$Q_{\lambda\lambda_1\lambda_2\lambda_3}$
#1	λ	λ	λ	λ	$\cos\left(\frac{\Theta-\Theta_2}{2}\right)\cos\left(\frac{\Theta_1-\Theta_2}{2}\right)\cos\left(\frac{\Theta-\Theta_3}{2}\right)\cos\left(\frac{\Theta_1-\Theta_3}{2}\right)$
#2	λ	$-\lambda$	λ	$-\lambda$	$-\cos\left(\frac{\Theta-\Theta_2}{2}\right)\cos\left(\frac{\Theta_1-\Theta_2}{2}\right)\sin\left(\frac{\Theta-\Theta_3}{2}\right)\sin\left(\frac{\Theta_1-\Theta_3}{2}\right)$
#3	λ	$-\lambda$	$-\lambda$	λ	$-\cos\left(\frac{\Theta-\Theta_2}{2}\right)\cos\left(\frac{\Theta_1-\Theta_2}{2}\right)\sin\left(\frac{\Theta-\Theta_3}{2}\right)\sin\left(\frac{\Theta_1-\Theta_3}{2}\right)$

Table 5.2: Q tensors

temperature in the hydrodynamic regime,

$$\tau(T) = c\,(1,\alpha)\,\frac{\hbar}{\alpha^2(T)v_r(T)k_F} \propto \ln\left(\frac{\Lambda_T}{T}\right) \tag{5.118}$$

in the $T \to 0$ limit. This result indicates that the relaxation time increases (logarithmically) at low temperature. In Fermi liquids, the scattering time diverges as $\tau \propto \hbar\varepsilon_F/(k_BT)^2$ at $T \to 0$, with ε_F the Fermi energy. Relativistic systems have a parametrically shorter scattering time ($\tau \sim \hbar/k_BT$), reflecting the absence of screening effects. Compared to graphene, the nodal line significantly enlarges the phase space for collisions of thermally activated quasiparticles, which remain unscreened. That results in a further reduced scattering time, which is controlled by the dominant energy scale set by the radius of the nodal line.

5.4.3 Shear viscosity

In this section, we will find shear viscosity of nodeline semimetal. The concept of viscosity was explained in section 5.3.2. The Boltzmann equation for viscosity should be

$$\left(\frac{\partial}{\partial t} + \mathbf{v}_{\lambda,\mathbf{k}} \cdot \nabla_{\mathbf{x}}\right) f = (I)_{\text{col}}\,. \tag{5.119}$$

Unlike conductivity analysis, we don't take Fourier transform to the frequency domain. Also, the time derivative term on the left-hand side may be dropped in the linearized equation because its contribution is actually second order in spatial gradients [151].

Going back to the kinetic equation (5.111), the second term on the left gives

$$\mathbf{v}_{\lambda,\mathbf{k}} \cdot \nabla_{\mathbf{x}} f^{(0)}(k) = \sqrt{\frac{2}{3}}\beta f^0_\lambda\left(1 - f^0_\lambda\right)\varepsilon_{\lambda,\mathbf{k}} I_{ij} u_{ij} \equiv \Phi_{\lambda,ij} I_{ij}, \tag{5.120}$$

with

$$I_{ij} = \sqrt{\frac{3}{2}} \left[(\mathbf{v}_{\lambda,\mathbf{k}})_i k_j / \varepsilon_{\lambda,\mathbf{k}} - (\delta_{ij}/3) \right].$$

Setting the electric field to zero, the change in the energy spectrum can be parametrized with the Ansatz $\varepsilon_{\lambda,k} = \varepsilon^{(0)}_{\lambda,k} + I_{ij} u_{ij} g_\lambda(\mathbf{k}, t)$, where $g_\lambda(\mathbf{k}, t)$ is to be determined by solving the kinetic equation. The non-equilibrium correction to the distribution function due to strain has the form

$$\delta f_\lambda(\mathbf{k}, t) = \beta f^0_\lambda \left(1 - f^0_\lambda\right) u_{ij} I_{ij} g_\lambda(\mathbf{k}, t). \tag{5.121}$$

Defining $\chi_{\lambda,ij} \equiv I_{ij} g_\lambda$, the kinetic equation in the stationary regime ($\omega \to 0$) is

$$\Phi_{\lambda,ij} = \mathcal{C}\chi_{\lambda,ij}. \tag{5.122}$$

The definition of the collision operator for strain is

$$\begin{aligned} \mathcal{C}\chi_{\lambda,ij} = \frac{1}{8} \sum_{\lambda_1\lambda_2\lambda_3} \int_{\mathbf{k}_1} \int_{\mathbf{k}_2} \int_{\mathbf{k}_3} (2\pi)^4 \delta^3(\mathbf{k} + \mathbf{k}_1 - \mathbf{k}_2 - \mathbf{k}_3) \, \delta\left(\varepsilon^0_{\lambda,k} + \varepsilon^0_{\lambda_1,k_1} - \varepsilon^0_{\lambda_2,k_2} - \varepsilon^0_{\lambda_3,k_3}\right) \\ \times \mathcal{M}^{\mathrm{Col}}_{\lambda\lambda_1\lambda_2\lambda_3} f^0_\lambda f^0_{\lambda_1} f^0_{-\lambda_2} f^0_{-\lambda_3} \\ \times \left[\chi_{\lambda,ij}(k) + \chi_{\lambda_1,ij}(k_1) - \chi_{\lambda_2,ij}(k_2) - \chi_{\lambda_3,ij}(k_3)\right], \end{aligned} \tag{5.123}$$

and follows directly from Eq. (5.114) under the substitution $\chi_{\lambda,i} \to \chi_{\lambda,ij}$.

In the collinear regime, there are three zero modes that are three eigenfunctions of the collision operator, $\mathcal{C}\chi_{\lambda,ij} = 0$, namely $\chi^{(1)}_{\lambda,ij}(\mathbf{k}) = \lambda I_{ij}$, $\chi^{(2)}_{\lambda,ij}(\mathbf{k}) = \lambda|\mathbf{h}|I_{ij}$ and $\chi^{(3)}_{\lambda,ij}(\mathbf{k}) = I_{ij}$. Those modes correspond to conservation charge, energy and number of particles respectively. The particle number zero mode, however, does not contribute to the shear viscosity due to particle-hole symmetry. This mode is orthogonal to the other two and can be completely decoupled.

Setting a basis with the charge and energy modes, one can express $\chi_{\lambda,ij}$ as a linear combination in that basis. Projecting $b^\alpha = (\chi^{(\alpha)}_{\lambda,ij}, \Phi_{\lambda,ij})$ and $\mathcal{C}_{\alpha\beta} = (\chi^{(\alpha)}_{\lambda,ij}, \mathcal{C}\chi^{(\beta)}_{\lambda,ij})$, then the solution of the kinetic equation is

$$\chi_{\lambda,ij}(\mathbf{k}) = b^\alpha \mathcal{C}^{-1}_{\alpha\beta} \chi^{(\beta)}_{\lambda,ij}(\mathbf{k}), \tag{5.124}$$

where $\mathcal{C}^{-1}_{\alpha\beta}$ is the inverse of a 2×2 matrix. Calculating this matrix numerically in the near collinear approximation, we find

$$b^\alpha \mathcal{C}^{-1}_{\alpha\beta} = (c^{\eta_1}, c^{\eta_2}) \approx (1.478, 3.585) \ln^2\left(\frac{1}{\alpha}\right). \tag{5.125}$$

As discussed before, non-collinear processes are expected to smooth out the logarithmic divergence in the $\alpha \to 0$ limit, which is expected when $T \to 0$. In any case, this is a double log divergence, as explained in the case of the conductivity. This factor changes very slowly and is subdominant compared to all other temperature effects. The incorporation of non-collinear processes in the

matrix elements of the collision operator is only accessible through a high dimensional integral, as will be addressed in a future publication.

As we discussed in section 5.3.2, we can derive the shear viscosity tensor from Eq (5.94) and (5.99). The shear viscosity tensor is

$$\begin{aligned}\eta_{xyxy} &= \sum_{\lambda}\int \frac{d^3k}{(2\pi)^3}\lambda^2\frac{(v_r\lambda h_x)^2}{|\mathbf{h}|^2}\frac{(q_y)^2}{\varepsilon_{\mathbf{k}}}\beta f^0_\lambda\left(1-f^0_\lambda\right)\left[a_2+v_r\beta\,|\mathbf{h}|\,a_3\right]\\ &= \frac{N}{\gamma\alpha^2}\left(\frac{1}{v_r\beta}\right)^3\frac{3}{16\pi}\left[c^{\eta_2}\frac{\pi^2}{6}+c^{\eta_3}\frac{9}{2}\zeta\left[3\right]\right]\\ &\approx 1.302\frac{N}{\alpha^2}\left(\frac{1}{v_r\beta}\right)^3\left(\frac{1}{\ln\left(1/\alpha\right)}\right)^2,\ \text{for } \gamma=1. \end{aligned} \tag{5.126}$$

and

$$\begin{aligned}\eta_{xzxz} &= \sum_{\lambda}\int \frac{d^3k}{(2\pi)^3}\lambda^2\frac{(v_r\lambda h_x)^2}{|\mathbf{h}|^2}\frac{(q_z)^2}{\varepsilon_{\mathbf{k}}}\beta f^0_\lambda\left(1-f^0_\lambda\right)\left[a_2+v_r\beta\,|\mathbf{h}|\,a_3\right]\\ &= \frac{1}{\gamma^3\alpha^2}\left(\frac{1}{v_r\beta}\right)^3\frac{1}{16\pi}\left[c^{\eta_2}\frac{\pi^2}{6}+c^{\eta_3}\frac{9}{2}\zeta\left[3\right]\right]\\ &\approx 0.434\frac{N}{\alpha^2}\left(\frac{1}{v_r\beta}\right)^3\frac{1}{\ln^2\left(1/\alpha\right)},\ \text{for } \gamma=1. \end{aligned} \tag{5.127}$$

From the results above, the viscosity is proportional to $\eta\propto(k_BT)^3/\left(\alpha^2v_r\right)$.

5.4.4 Ratio η/s

To calculate the ratio between the shear viscosity and the entropy, we now calculate the entropy term. The unperturbed entropy density of a NLSM can be found from the entropy of a non interacting system, and allow all velocities be renormalized according to the RG flow prescription,

$$\begin{aligned} s &= -k_BN\int d^3k\left\{f^0\ln f^0+\left(1-f^0\right)\ln\left(1-f^0\right)\right\}\\ &= \frac{k_Bk_F}{\gamma v_r^2\beta^2}\frac{9}{4}\zeta\left[3\right]. \end{aligned} \tag{5.128}$$

The ratio between shear viscosity and entropy density is

$$\frac{\eta_{xixi}}{s}\propto\frac{\hbar}{k_B}c_i\frac{Nk_BT}{\alpha^2v_rk_F}\ln^2\left(\frac{1}{\alpha}\right), \tag{5.129}$$

with $c_y=0.482$ and $c_z=0.161$ ($\gamma=1$). Since the quantity αv_r flows to a constant in the RG, and $\ln^2(1/\alpha)=\ln^2\left(\frac{v_r(T)}{\alpha v_r}\right)$ is a double log, which is an extremely slow function, then

$$\frac{\eta}{s}\propto\frac{\hbar}{k_B}\frac{k_BT}{\alpha^2(T)v_r(T)k_F}\overset{T\ll\Lambda_T}{\longrightarrow}\frac{\hbar}{k_B}\frac{k_BT}{\alpha^2v_rk_F}\log\left(\frac{\Lambda_T}{T}\right). \tag{5.130}$$

Therefore this ratio $\eta/s\to0$ in the limit where $T\to0$.

This result does not imply necessarily that NLSMs are close to become a perfect fluid, however. The RG analysis of this problem has shown that Coulomb interactions lead to weak logarithmic corrections to the various physical observables in the perturbative regime, as in graphene, and the system essentially remains a semimetal. The most sensible conclusion is that the rationale behind the conjecture that relativistic systems in general have a lower bound at $\eta/s = (1/4\pi)\hbar/k_B$, as originally derived for infinitely strongly coupled conformal field theory [181], needs to be revised to account for unscreened relativistic systems with Fermi surfaces. In that sense, the criterion for a perfect fluid − or a quantum fluid with the lowest possible viscosity− need to be corrected to incorporate the energy scale set by the Fermi surface. The important distinction with Fermi liquids in that regard is that this energy scale is not the Fermi energy, and therefore does not introduce screening, but is related to the radius of the nodal line. It would be interesting to verify how this ratio relates to the Raynolds number, and how susceptible NLSMs are to exhibit quantum turbulence.

Chapter 6

Conclusion

In this thesis we have addressed a variety of interesting quantum effects, from novel topologically protected bulk and surface states, the 3D quantum anomalous Hall (QAH) effect, the elastic quantum Hall effect and the associated elastic Hall viscosity, and hydrodynamic transports in 3D NLSMs.

We introduced the concept of NLSMs after reviewing the literature for materials realizations, briefly analyzing the symmetries which protect the nodal lines, and placing those systems in the context of Dirac and Weyl systems in general. The surface state of NLSMs exhibit surface bands embedded inside of a projected node-line. Those are called 'drumhead' surface states. By preserving mirror or rotational symmetry and breaking at least one of time reversal (TR) and inversion symmetry, node lines are gapped out generating one or more pairs of Weyl nodes. The surface state of Weyl semimetals is described by discontinuous line connecting projected Weyl nodes, which is known as 'Fermi arc'.

Inspired by two areas of research in quantum Hall physics, we proposed a possible 3D QAH state transition in a lattice realization of NLSMs called hyperhoneycomb lattices. We show that 3D anomalous Hall conductivity σ_{ij} is $e^2/\left(\sqrt{3}ha\right)$ for (i,j)=(y,z) or (x,z), with a a lattice constant. Because of the mass gap which breaks time reversal (TR) symmetry, the nodal line is gapped out while topologically protected six Weyl points emerges in the bulk and generate Fermi arc as a surface state. In the 3D QAH phase, we calculate dissipationless elastic Hall viscosity tensor, which is either $\eta_H = \beta^2\sqrt{3}/\left(16\pi a^3\right)$ or $2\eta_H$ for the antisymmetric components where β is an elastic parameter and a is the lattice constant. We also address elastic gauge fields in the hyperhoneycomb lattice that result in nearly flat Landau levels in 3D. We propose a possible physical implementation, through a family of strain deformations that can be implemented with temperature gradients.

Finally, we introduce the concept hydrodynamic behavior for quasiparticles in a quantum fluid. We derive transport coefficients, electrical conductivity and shear viscosity in hydrodynamic regime for a NLSM. The transport coefficients can be effectively derived from the eigenfunctions of collision operator of linearized Boltzmann equation, which are extracted by physical conservation laws in collinear regime. We showed that both the longitudinal conductivity in the collision dominated regime and the viscosity-entropy ratio η/s scale linearly with temperature, in contrast with relativistic systems in general where both saturate to a constant at low temperature. The ratio between

the shear viscosity and the entropy also departs from Fermi liquid behavior, where it diverges at low T. This fact violates the conjectured universal lower bound for the ratio proposed by Kovton et al. [181], which has been attributed to perfect fluids, quantum systems with the lowest possible viscosity per entropy production, and which were speculated to lead to quantum turbulence.

The scaling in NLSMs can be physically explained by T dependence of momentum relaxation time τ. The scale of the free energy density is entirely entropic $f = sT$, but the enlarged phase space for scattering along the continuous large nodal line allows for faster relaxation of the quasiparticles compared to the case of the discrete nodal points at temperature $T \ll v_F k_F$. Unlike usual momentum relaxation time which is $\tau_\hbar \propto 1/k_B T$ in graphene and Plankian dissipation, this system has a transport momentum relaxation time $\tau_K \propto \hbar/v_F k_F$ that is temperature independent, up to weak logarithmic corrections. As a result, the viscosity follows $\eta \simeq f \cdot \tau \simeq sT$. It would be interesting to relate this ratio with the Reynolds number and assess how close NLSMs are to show quantum turbulence.

Observing hydrodynamic behavior of electrons in 3D material is typically challenging because one key requirement of hydrodynamic behavior is that transport is dominated by unscreened quasiparticles, with a relatively short scattering time. That requires the Fermi level to be close to the nodal line, where the system exhibits particle hole symmetry. Unlike in 2D materials, one cannot tune the chemical potential inside a 3D bulk material, therefore one is limited to materials where the Fermi levels happens to be sufficiently close to the nodal line. The physics outlined in chapter 5 would be valid in the hydrodynamic regime $\omega \lesssim \tau^{-1}$, provided that $k_B T > \varepsilon_F$, with ε_F the energy of the toroidal Fermi surface enclosing the nodal line. We expect that the change in conductivity with temperature will be an indicator of hydrodynamic behavior, which can be accomplished with transport measurements. Some of the predictions of hydrodynamic behavior in systems like graphene include the presence of quantum turbulence and negative resistivity in four terminal measurements, which emerge due to the spontaneous formation of vortices in the electronic flow. The observation of quantum turbulence in a 3D material, however, is significantly more involved than in 2D systems, where the geometry of constrictions is simpler. Our results suggest that NLSMs are very strongly interacting systems, and may be amenable to quantum turbulence. The absence of a lower bound for the shear viscosity and the entropy challenges the existence of a lower bound to begin with and possibly suggests that this quantity needs to be reinterpreted to account for relativistic systems with unscreened Fermi surfaces. On the experimental front, one can hope that the discovery of clean NLSM materials with large nodal lines sitting near the Fermi level will permit exploration of the quantum transport in these materials in the near future.

Appendix A

2D Hall Conductance

The generic Hamiltonian involving two bands can be written as

$$H = \mathbf{d}(\mathbf{k}) \cdot \boldsymbol{\sigma}, \tag{A.1}$$

where

$$|\mathbf{d}| = \sqrt{d_1^2 + d_2^2 + d_3^2}, \quad \hat{\mathbf{d}}(\mathbf{k}) = \frac{\mathbf{d}(\mathbf{k})}{|\mathbf{d}|}. \tag{A.2}$$

One can define a winding number n_W by mapping $\mathbf{k} \to \hat{\mathbf{d}}(\mathbf{k})$:

$$n_W = \frac{1}{4\pi} \int d^2k \left(\frac{\partial \hat{\mathbf{d}}(\mathbf{k})}{\partial k_x} \times \frac{\partial \hat{\mathbf{d}}(\mathbf{k})}{\partial k_y} \right) \cdot \hat{\mathbf{d}}(\mathbf{k}). \tag{A.3}$$

Employing the parametrization for $\hat{\mathbf{d}}(\mathbf{k})$:

$$\hat{\mathbf{d}}(\mathbf{k}) = \begin{pmatrix} \cos\phi_k \sin\theta_k \\ \sin\phi_k \sin\theta_k \\ \cos\theta_k \end{pmatrix}, \tag{A.4}$$

the eigenvector of the lower band is

$$\phi_- = \begin{pmatrix} \sin\frac{\theta_k}{2} e^{-i\phi_k} \\ \cos\frac{\theta_k}{2} \end{pmatrix}. \tag{A.5}$$

The Berry curvature is:

$$(\Omega_-)_{xy} = \frac{\partial}{\partial k_x}(A_-)_y - \frac{\partial}{\partial k_y}(A_-)_x \tag{A.6}$$

$$= i\frac{\partial}{\partial k_x}\sum_{\alpha=x,y}\left(\phi_-^\dagger\right)_\alpha \frac{\partial}{\partial k_y}(\phi_-)_\alpha - i\frac{\partial}{\partial k_y}\sum_{\alpha=x,y}\left(\phi_-^\dagger\right)_\alpha \frac{\partial}{\partial k_x}(\phi_-)_\alpha \tag{A.7}$$

$$= \frac{\partial}{\partial k_x}\sin^2\frac{\theta_k}{2}\frac{\partial\phi_k}{\partial k_y} - \frac{\partial}{\partial k_y}\sin^2\frac{\theta_k}{2}\frac{\partial\phi_k}{\partial k_x} \tag{A.8}$$

$$= \frac{1}{2}\sin\theta_k\left(\frac{\partial\theta_k}{\partial k_x}\frac{\partial\phi_k}{\partial k_y} - \frac{\partial\phi_k}{\partial k_x}\frac{\partial\theta_k}{\partial k_y}\right). \tag{A.9}$$

In the same way, one ca derive the Chern number:

$$C_{2D} = \frac{1}{2\pi}\int_{BZ} d\mathbf{k}\,(\Omega_-)_{xy} = \frac{1}{4\pi}\int d^2k\,\sin\theta_k\left(\frac{\partial\theta_k}{\partial k_x}\frac{\partial\phi_k}{\partial k_y} - \frac{\partial\phi_k}{\partial k_x}\frac{\partial\theta_k}{\partial k_y}\right) \tag{A.10}$$

$$= \frac{1}{4\pi}\int d^2k\left(\frac{\partial\hat{\mathbf{d}}(\mathbf{k})}{\partial k_x}\times\frac{\partial\hat{\mathbf{d}}(\mathbf{k})}{\partial k_y}\right)\cdot\hat{\mathbf{d}}(\mathbf{k}) = n_W. \tag{A.11}$$

Hence, the Winding number for the simple model of massive Dirac fermions is the same with the total Chern number [13].

The 2D Hall conductance can be expressed in terms of the Kubo formula [100]:

$$\sigma_{xy} = \frac{e^2}{4\pi h}\int d^2k\,\left(f_+(\mathbf{k}) - f_-(\mathbf{k})\right)\left(\frac{\partial\hat{\mathbf{d}}(\mathbf{k})}{\partial k_x}\times\frac{\partial\hat{\mathbf{d}}(\mathbf{k})}{\partial k_y}\right)\cdot\hat{\mathbf{d}}(\mathbf{k}). \tag{A.12}$$

Thus,

$$\sigma_{xy} = \frac{e^2}{h}n_W = \frac{e^2}{h}C_{2D}. \tag{A.13}$$

Appendix B

Mean-field Hamiltonian of HHC lattice

We find 6 NN hopping vectors δ_n as

$$\begin{aligned}
\mathbf{a}_{AB1} &= \left(\frac{\sqrt{3}}{2}a,\ 0,\ \frac{a}{2}\right) \\
\mathbf{a}_{AB2} &= \left(-\frac{\sqrt{3}}{2}a,\ 0,\ \frac{a}{2}\right) \\
\mathbf{a}_{CD1} &= \left(0,\ \frac{\sqrt{3}}{2}a,\ \frac{a}{2}\right) \\
\mathbf{a}_{CD2} &= \left(0,\ -\frac{\sqrt{3}}{2}a,\ \frac{a}{2}\right) \\
\mathbf{a}_{AD} &= (0,\ 0,\ -a) \\
\mathbf{a}_{BC} &= (0,\ 0,\ a)
\end{aligned}$$

Also, we find six vectors in NNN loop $\mathbf{b}_{xi}$ and $\mathbf{b}_{yi}$ $(i = 1, 2, 3)$. We can express all NNN sites with the vectors.

$$\mathbf{b}_{x1} = (a\sqrt{3}, 0, 0), \quad \mathbf{b}_{x2} = (-\frac{\sqrt{3}}{2}a, 0, -\frac{3}{2}a), \quad \mathbf{b}_{x3} = (-\frac{\sqrt{3}}{2}a, 0, \frac{3}{2}a) \tag{B.1}$$

$$\mathbf{b}_{y1} = (0, a\sqrt{3}, 0), \quad \mathbf{b}_{y2} = (0, -\frac{\sqrt{3}}{2}a, \frac{3}{2}a), \quad \mathbf{b}_{y3} = (0, -\frac{\sqrt{3}}{2}a, -\frac{3}{2}a) \tag{B.2}$$

We can build tight-binding hamiltonian

$$H = \sum_{\langle i,j\rangle} t(C_i^\dagger C_j) + \sum_{\langle i,j\rangle} V_1(C_i^\dagger C_i - 1)(C_j^\dagger C_j - 1) + \sum_{\langle\langle i,j\rangle\rangle} V_2(C_i^\dagger C_i - 1)(C_j^\dagger C_j - 1) \tag{B.3}$$

where $\langle i,j\rangle$ and $\langle\langle i,j\rangle\rangle$ denotes NN sites and NNN sites respectively. Define the creation, annihilation operators $A^\dagger$ and A for A sublattice, and so as B, C, and D. The first term of the Hamiltonian

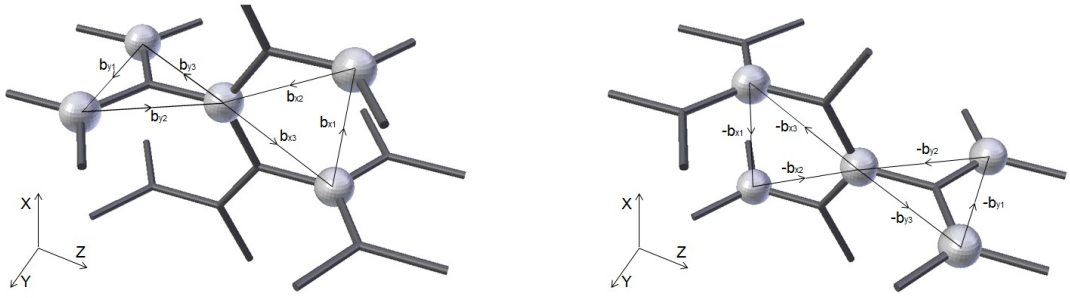

(a) (b)

Figure B.1: (a) The first set of sublattices (A and C) and two NNN loop. (b) The second set of sublattices (B and D) and two NNN loop.

(B.3) is easily calculated by a Fourier transformation:

$$H_0(\mathbf{k}) = \sum_{\mathbf{k}} t \left[\Theta_x A^\dagger B + \Theta_y C^\dagger D + e^{-ik_z a} A^\dagger D + e^{-ik_z a} B^\dagger C + \text{h.c.}\right] \tag{B.4}$$

where $\Theta_i = 2e^{ik_z a/2} cos(\sqrt{3}k_i a/2)$ with $i = x, y$ and a is interatomic distance. "h.c." implies the Hermitian conjugation of prior terms.

For the second term of (B.3), using a mean field approximation:

$$\begin{aligned} H_1 &= V_1 \sum_{\langle i,j \rangle} \left(A^\dagger A D^\dagger D + A^\dagger A B^\dagger B + B^\dagger B C^\dagger C + C^\dagger C D^\dagger D\right) \\ &= V_1 \Big[\left\langle A^\dagger A \right\rangle \left(D^\dagger D + B_1^\dagger B_1 + B_2^\dagger B_2\right) - \left\langle A^\dagger A \right\rangle \left\langle D^\dagger D \right\rangle \\ &\quad + \left\langle B^\dagger B \right\rangle \left(A_1^\dagger A_1 + A_1^\dagger A_1 + C^\dagger C\right) - 2 \left\langle A^\dagger A \right\rangle \left\langle B^\dagger B \right\rangle \\ &\quad + \left\langle C^\dagger C \right\rangle \left(B^\dagger B + D_1^\dagger D_1 + D_1^\dagger D_1\right) - \left\langle B^\dagger B \right\rangle \left\langle C^\dagger C \right\rangle \\ &\quad + \left\langle D^\dagger D \right\rangle \left(A^\dagger A + C_1^\dagger C_1 + C_1^\dagger C_1\right) - 2 \left\langle C^\dagger C \right\rangle \left\langle D^\dagger D \right\rangle\Big] \end{aligned} \tag{B.5}$$

We take Fourier transformation and use order parameter defined in chapter 3.2:

$$H_1(\mathbf{k}) = 3V_1 \rho \sum_{\mathbf{k}} \left(-A^\dagger A + B^\dagger B - C^\dagger C + D^\dagger D\right) + 6\rho^2 V_1 N \tag{B.6}$$

For the third term of (B.3), using a mean field approximation and assuming $\chi_{\mathbf{r}}(\mathbf{b})$ is independent

of $\mathbf{r}$ and have a same modulus with$|\chi|$,

$$\begin{aligned} H_2 &= -\frac{V_2}{2}\sum_{\mathbf{r}\in A}\left(\sum_{\mathbf{b}\in NNN}\chi_{AA}(\mathbf{b})A^\dagger_{\mathbf{r}+\mathbf{b}}A_{\mathbf{r}}+\sum_{\mathbf{b}\in NNN}\chi_{AC}(\mathbf{b})C^\dagger_{\mathbf{r}+\mathbf{b}}A_{\mathbf{r}}\right) \\ &\quad -\frac{V_2}{2}\sum_{\mathbf{r}\in B}\left(\sum_{\mathbf{b}\in NNN}\chi_{BB}(\mathbf{b})B^\dagger_{\mathbf{r}+\mathbf{b}}B_{\mathbf{r}}+\sum_{\mathbf{b}\in NNN}\chi_{BD}(\mathbf{b})D^\dagger_{\mathbf{r}+\mathbf{b}}B_{\mathbf{r}}\right) \\ &\quad -\frac{V_2}{2}\sum_{\mathbf{r}\in C}\left(\sum_{\mathbf{b}\in NNN}\chi_{CC}(\mathbf{b})C^\dagger_{\mathbf{r}+\mathbf{b}}C_{\mathbf{r}}+\sum_{\mathbf{b}\in NNN}\chi_{CA}(\mathbf{b})A^\dagger_{\mathbf{r}+\mathbf{b}}C_{\mathbf{r}}\right) \\ &\quad -\frac{V_2}{2}\sum_{\mathbf{r}\in D}\left(\sum_{\mathbf{b}\in NNN}\chi_{DD}(\mathbf{b})D^\dagger_{\mathbf{r}+\mathbf{b}}D_{\mathbf{r}}+\sum_{\mathbf{b}\in NNN}\chi_{DB}(\mathbf{b})B^\dagger_{\mathbf{r}+\mathbf{b}}D_{\mathbf{r}}\right) \\ &\quad +\text{h.c.}+16V_2\left|\chi\right|^2 \end{aligned} \tag{B.7}$$

Take Fourier transformation.

$$\begin{aligned} H_2 &= -\frac{V_2}{2}\sum_{\mathbf{r}}\left(\sum_{\mathbf{b}\in NNN}\chi_{AA}(\mathbf{b})\sum_{\mathbf{k},\mathbf{k}'}A^\dagger_{\mathbf{k}}A_{\mathbf{k}'}e^{i(\mathbf{k}-\mathbf{k}')\cdot\mathbf{r}}e^{i\mathbf{k}\cdot\mathbf{b}}\right) \\ &\quad -\frac{V_2}{2}\sum_{\mathbf{r}}\left(\sum_{\mathbf{b}\in NNN}\chi_{AC}(\mathbf{b})\sum_{\mathbf{k},\mathbf{k}'}C^\dagger_{\mathbf{k}}A_{\mathbf{k}'}e^{i(\mathbf{k}-\mathbf{k}')\cdot\mathbf{r}}e^{i\mathbf{k}\cdot\mathbf{b}}\right) \\ &\quad +(AA\to BB)+(AC\to BD) \\ &\quad +(AA\to CC)+(AC\to CA) \\ &\quad +(AA\to DD)+(AC\to DB) \\ &\quad +\text{h.c.}+16V_2\left|\chi\right|^2 \end{aligned} \tag{B.8}$$

$$\begin{aligned} H_2(\mathbf{k}) &= -\frac{V_2}{2}\sum_{\mathbf{k}}\left(\sum_{\mathbf{b}\in NNN}e^{i\mathbf{k}\cdot\mathbf{b}}\chi_{AA}(\mathbf{b})\right)A^\dagger_{\mathbf{k}}A_{\mathbf{k}}+\dots \\ &= -\frac{V_2}{2}\sum_{\mathbf{k}}\chi_{AA}(\mathbf{k})A^\dagger_{\mathbf{k}}A_{\mathbf{k}}+\dots \end{aligned} \tag{B.9}$$

where $\chi_{ij}(\mathbf{k})$ is defined as

$$\chi_{ij}(\mathbf{k})=\sum_{\mathbf{b}\in NNN}e^{i\mathbf{k}\cdot\mathbf{b}}\chi_{ij}(\mathbf{b}),\quad i,j=A,B,C,D. \tag{B.10}$$

Then, Hamiltonian matrix is,

$$H_2(\mathbf{k}) = -\frac{V_2}{2}\begin{pmatrix} (\chi_{AA}+\chi^*_{AA}) & 0 & (\chi_{CA}+\chi^*_{AC}) & 0 \\ 0 & (\chi_{BB}+\chi^*_{BB}) & 0 & (\chi_{DB}+\chi^*_{BD}) \\ (\chi_{AC}+\chi^*_{CA}) & 0 & (\chi_{CC}+\chi^*_{CC}) & 0 \\ 0 & (\chi_{BD}+\chi^*_{DB}) & 0 & (\chi_{DD}+\chi^*_{DD}) \end{pmatrix} \tag{B.11}$$

Note that diagonal components are real value and the Hamiltonian is hermitian. Also, $\chi_{AC} = \chi^*_{CA}$, $\chi_{BD} = \chi^*_{DB}$ So, total Hamiltonian is below.

$$H(\mathbf{k}) = \begin{pmatrix} -3\rho V_1 - V_2\mathrm{Re}\left(\chi_{AA}\right) & t\cdot\Theta_x & -V_2\left(\chi^*_{AC}\right) & t\cdot e^{-ik_z a} \\ (t\cdot\Theta_x)^\star & 3\rho V_1 - V_2\mathrm{Re}\left(\chi_{BB}\right) & t\cdot e^{ik_z a} & -V_2\left(\chi^*_{BD}\right) \\ -V_2\left(\chi_{AC}\right) & t\cdot e^{-ik_z a} & -3\rho V_1 - V_2\mathrm{Re}\left(\chi_{CC}\right) & t\cdot\Theta_y \\ t\cdot e^{ik_z a} & -V_2\left(\chi_{BD}\right) & (t\cdot\Theta_y)^\star & 3\rho V_1 - V_2\mathrm{Re}\left(\chi_{DD}\right) \end{pmatrix} \tag{B.12}$$

For each $\chi_{ij}(\mathbf{k})$, we can calculate with $\mathbf{b}$ vectors above and the argument about $\phi_{\alpha=A,C} = \frac{\pi}{2}$ and $\phi_{\alpha=B,D} = -\frac{\pi}{2}$. As a result,

$$\mathrm{Re}\left(\chi_{AA}\right) = \mathrm{Re}\left(\chi_{CC}\right) = 2\left|\chi\right|\left[\sin\left(\sqrt{3}k_x/2\right) + \sin\left(\sqrt{3}k_y/2\right)\right] \tag{B.13}$$

$$\mathrm{Re}\left(\chi_{BB}\right) = \mathrm{Re}\left(\chi_{DD}\right) = -2\left|\chi\right|\left[\sin\left(\sqrt{3}k_x/2\right) + \sin\left(\sqrt{3}k_y/2\right)\right] \tag{B.14}$$

$$\chi_{AC} = 2\left|\chi\right|\left[e^{-3ik_z/2}\sin\left(\sqrt{3}k_x/2\right) + e^{3ik_z/2}\sin\left(\sqrt{3}k_y/2\right)\right] \tag{B.15}$$

$$\chi_{BD} = -2\left|\chi\right|\left[e^{3ik_z/2}\sin\left(\sqrt{3}k_x/2\right) + e^{-3ik_z/2}\sin\left(\sqrt{3}k_y/2\right)\right] \tag{B.16}$$

Appendix C

Linearized Boltzmann Equation

We derive in detail the linearized Boltzmann equation for the conductivity Ansatz of the Fermi distribution f described in the main text, in linear response with the electrical field $\mathbf{E}$. The left-hand side can be readily obtained,

$$LHS = \left(-i\omega\chi_\lambda\left(k,\omega\right)-1\right)\beta e E_i\left(\omega\right)\left(\mathbf{v_k}\right)_i f_\lambda^{(0)}\left(1-f_\lambda^{(0)}\right). \tag{C.1}$$

The right-hand side should be $[\varepsilon_{\lambda_i}\equiv\varepsilon_{\lambda_i}\left(k_i\right)\,]$,

$$\begin{aligned} RHS = & \int_{\mathbf{k}_1}\int_{\mathbf{k}_2}\int_{\mathbf{k}_3}\left(2\pi\right)^4\delta^3\left(\mathbf{k}+\mathbf{k}_1-\mathbf{k}_2-\mathbf{k}_3\right)\delta\left(\varepsilon_\lambda+\varepsilon_{\lambda_1}-\varepsilon_{\lambda_2}-\varepsilon_{\lambda_3}\right) \\ & \times\left[NV\left(\mathbf{k}-\mathbf{k}_2\right)V\left(\mathbf{k}-\mathbf{k}_2\right)M_{\lambda_3\lambda_1}M_{\lambda_1\lambda_3}M_{\lambda\lambda_2}M_{\lambda_2\lambda}\right. \\ & \left.-V\left(\mathbf{k}-\mathbf{k_2}\right)V\left(\mathbf{k}-\mathbf{k_3}\right)M_{\lambda\lambda_2}M_{\lambda_2\lambda_1}M_{\lambda_1\lambda_3}M_{\lambda_3\lambda}\right] \\ & \times\left\{\left[\left(1-f_\lambda\right)\left(1-f_{\lambda_1}\right)f_{\lambda_2}f_{\lambda_3}\right]^{(1)}-\left[f_\lambda f_{\lambda_1}\left(1-f_{\lambda_2}\right)\left(1-f_{\lambda_3}\right)\right]^{(1)}\right\}, \end{aligned} \tag{C.2}$$

or equivalently,

$$\begin{aligned} RHS = & \int_{\mathbf{k}_1}\int_{\mathbf{k}_2}\int_{\mathbf{k}_3}\left(2\pi\right)^4\delta^3\left(\mathbf{k}+\mathbf{k}_1-\mathbf{k}_2-\mathbf{k}_3\right)\delta\left(\varepsilon_\lambda+\varepsilon_{\lambda_1}-\varepsilon_{\lambda_2}-\varepsilon_{\lambda_3}\right) \\ & \times\left[NV\left(\mathbf{k}-\mathbf{k}_2\right)^2W_{\lambda\lambda_1\lambda_2\lambda_3}-V\left(\mathbf{k}-\mathbf{k_2}\right)V\left(\mathbf{k}-\mathbf{k_3}\right)Q_{\lambda\lambda_1\lambda_2\lambda_3}\right] \\ & \times\left[\left(1-f_\lambda\right)\left(1-f_{\lambda_1}\right)f_{\lambda_2}f_{\lambda_3}-f_\lambda f_{\lambda_1}\left(1-f_{\lambda_2}\right)\left(1-f_{\lambda_3}\right)\right]^{(1)}, \end{aligned} \tag{C.3}$$

with

$$\begin{aligned} W_{\lambda\lambda_1\lambda_2\lambda_3} &= M_{\lambda\lambda_2}M_{\lambda_2\lambda}M_{\lambda_3\lambda_1}M_{\lambda_1\lambda_3} \\ Q_{\lambda\lambda_1\lambda_2\lambda_3} &= M_{\lambda\lambda_2}M_{\lambda_1\lambda_3}M_{\lambda_3\lambda}M_{\lambda_2\lambda_1}. \end{aligned}$$

The third line has two terms with four f functions. One should expand it as eight terms which have three $f^{(0)}$ and one δf. We can simplify them using $f_{-\lambda}^{(0)}f_{-\lambda_1}^{(0)}f_{\lambda_2}^{(0)}f_{\lambda_3}^{(0)}=f_\lambda^{(0)}f_{\lambda_1}^{(0)}f_{-\lambda_2}^{(0)}f_{-\lambda_3}^{(0)}$, which is

restricted by the energy conservation:

$$\begin{aligned} f_{-\lambda}^{(0)} f_{-\lambda_1}^{(0)} f_{\lambda_2}^{(0)} f_{\lambda_3}^{(0)} &= e^{\left(\lambda v_r k' + \lambda v_r k_1'\right)\beta} f_{\lambda}^{(0)} f_{\lambda_1}^{(0)} f_{\lambda_2}^{(0)} f_{\lambda_3}^{(0)} \\ &= e^{\left(\lambda v_r k_2' + \lambda v_r k_3'\right)\beta} f_{\lambda}^{(0)} f_{\lambda_1}^{(0)} f_{\lambda_2}^{(0)} f_{\lambda_3}^{(0)} \\ &= f_{\lambda}^{(0)} f_{\lambda_1}^{(0)} f_{-\lambda_2}^{(0)} f_{-\lambda_3}^{(0)}. \end{aligned} \tag{C.4}$$

Then,

$$\begin{aligned} RHS = & \int_{\mathbf{k}_1}\int_{\mathbf{k}_2}\int_{\mathbf{k}_3} (2\pi)^4 \delta^3\left(\mathbf{k}+\mathbf{k}_1-\mathbf{k}_2-\mathbf{k}_3\right)\delta\left(\varepsilon_\lambda+\varepsilon_{\lambda_1}-\varepsilon_{\lambda_2}-\varepsilon_{\lambda_3}\right) \\ & \times\left[NV\left(\mathbf{k}-\mathbf{k}_2\right)^2 W_{\lambda\lambda_1\lambda_2\lambda_3} - V\left(\mathbf{k}-\mathbf{k_2}\right)V\left(\mathbf{k}-\mathbf{k_3}\right)Q_{\lambda\lambda_1\lambda_2\lambda_3}\right]\beta e E_i(\omega) \\ & \times\Big[f_{\lambda}^{(0)} f_{-\lambda}^{(0)}\chi_i(\lambda,k)\left(-\left(1-f_{\lambda_1}^{(0)}\right)f_{\lambda_2}^{(0)}f_{\lambda_3}^{(0)}\right) - f_{\lambda_1}^{(0)}\left(1-f_{\lambda_2}^{(0)}\right)\left(1-f_{\lambda_3}^{(0)}\right) \\ & + f_{\lambda_1}^{(0)} f_{-\lambda_1}^{(0)}\chi_i(\lambda_1,k_1)\left(-\left(1-f_{\lambda}^{(0)}\right)f_{\lambda_2}^{(0)}f_{\lambda_3}^{(0)}\right) - f_{\lambda}^{(0)}\left(1-f_{\lambda_2}^{(0)}\right)\left(1-f_{\lambda_3}^{(0)}\right) \\ & + f_{\lambda_2}^{(0)} f_{-\lambda_2}^{(0)}\chi_i(\lambda_2,k_2)\left(\left(1-f_{\lambda}^{(0)}\right)\left(1-f_{\lambda_1}^{(0)}\right)f_{\lambda_3}^{(0)} + f_{\lambda}^{(0)}f_{\lambda_1}^{(0)}\left(1-f_{\lambda_3}^{(0)}\right)\right) \\ & + f_{\lambda_3}^{(0)} f_{-\lambda_3}^{(0)}\chi_i(\lambda_3,k_3)\left(\left(1-f_{\lambda}^{(0)}\right)\left(1-f_{\lambda_1}^{(0)}\right)f_{\lambda_2}^{(0)} + f_{\lambda}^{(0)}f_{\lambda_1}^{(0)}\left(1-f_{\lambda_2}^{(0)}\right)\right)\Big] \end{aligned}$$

$$\begin{aligned} = & \int_{\mathbf{k}_1}\int_{\mathbf{k}_2}\int_{\mathbf{k}_3} (2\pi)^4 \delta^3\left(\mathbf{k}+\mathbf{k}_1-\mathbf{k}_2-\mathbf{k}_3\right)\delta\left(\varepsilon_\lambda+\varepsilon_{\lambda_1}-\varepsilon_{\lambda_2}-\varepsilon_{\lambda_3}\right) \\ & \times\left[NV\left(\mathbf{k}-\mathbf{k}_2\right)^2 W_{\lambda\lambda_1\lambda_2\lambda_3} - V\left(\mathbf{k}-\mathbf{k_2}\right)V\left(\mathbf{k}-\mathbf{k_3}\right)Q_{\lambda\lambda_1\lambda_2\lambda_3}\right] \\ & \times \beta e E_i(\omega)\, v_i\Big[f_{\lambda}^{(0)} f_{-\lambda}^{(0)}\chi_i(\lambda,k)\left(-f_{-\lambda_1}^{(0)}f_{\lambda_2}^{(0)}f_{\lambda_3}^{(0)}\right) - f_{\lambda_1}^{(0)} f_{-\lambda_2}^{(0)} f_{-\lambda_3}^{(0)} \\ & + f_{\lambda_1}^{(0)} f_{-\lambda_1}^{(0)}\chi_i(\lambda_1,k_1)\left(-f_{-\lambda}^{(0)}f_{\lambda_2}^{(0)}f_{\lambda_3}^{(0)}\right) - f_{\lambda}^{(0)} f_{-\lambda_2}^{(0)} f_{-\lambda_3}^{(0)} \\ & + f_{\lambda_2}^{(0)} f_{-\lambda_2}^{(0)}\chi_i(\lambda_2,k_2)\left(f_{-\lambda}^{(0)}f_{-\lambda_1}^{(0)}f_{\lambda_3}^{(0)} + f_{\lambda}^{(0)}f_{\lambda_1}^{(0)}f_{-\lambda_3}^{(0)}\right) \\ & + f_{\lambda_3}^{(0)} f_{-\lambda_3}^{(0)}\chi_i(\lambda_3,k_3)\left(f_{-\lambda}^{(0)}f_{-\lambda_1}^{(0)}f_{\lambda_2}^{(0)} + f_{\lambda}^{(0)}f_{\lambda_1}^{(0)}f_{-\lambda_2}^{(0)}\right)\Big] \end{aligned}$$

$$\begin{aligned} = & \int_{\mathbf{k}_1}\int_{\mathbf{k}_2}\int_{\mathbf{k}_3} (2\pi)^4 \delta^3\left(\mathbf{k}+\mathbf{k}_1-\mathbf{k}_2-\mathbf{k}_3\right)\delta\left(\varepsilon_\lambda+\varepsilon_{\lambda_1}-\varepsilon_{\lambda_2}-\varepsilon_{\lambda_3}\right) \\ & \times\left[NV\left(\mathbf{k}-\mathbf{k}_2\right)^2 W_{\lambda\lambda_1\lambda_2\lambda_3} - V\left(\mathbf{k}-\mathbf{k_2}\right)V\left(\mathbf{k}-\mathbf{k_3}\right)Q_{\lambda\lambda_1\lambda_2\lambda_3}\right] \\ & \times \beta e E_i(\omega)\, f_{\lambda}^{(0)} f_{\lambda_1}^{(0)} f_{-\lambda_2}^{(0)} f_{-\lambda_3}^{(0)} \\ & \times\Big[-\left(f_{\lambda}^{(0)}+f_{-\lambda}^{(0)}\right)\chi_i(\lambda,k) - \left(f_{\lambda_1}^{(0)}+f_{-\lambda_1}^{(0)}\right)\chi_i(\lambda_1,k_1) \\ & \quad + \left(f_{-\lambda_2}^{(0)}+f_{\lambda_2}^{(0)}\right)\chi_i(\lambda_2,k_2) + \left(f_{-\lambda_3}^{(0)}+f_{\lambda_3}^{(0)}\right)\chi_i(\lambda_3,k_3)\Big], \end{aligned}$$

where $\chi_i(\lambda,k) = (\mathbf{v_k})_i\,\chi_{\lambda,k}$. Since $f_{\lambda}^{(0)} + f_{-\lambda}^{(0)} = 1$,

$$
\begin{aligned}
RHS = & -\int_{\mathbf{k}_1}\int_{\mathbf{k}_2}\int_{\mathbf{k}_3}(2\pi)^4\,\delta^3\left(\mathbf{k}+\mathbf{k}_1-\mathbf{k}_2-\mathbf{k}_3\right)\delta\left(\varepsilon_\lambda+\varepsilon_{\lambda_1}-\varepsilon_{\lambda_2}-\varepsilon_{\lambda_3}\right) \\
& \times\left[NV\left(\mathbf{k}-\mathbf{k}_2\right)^2 W_{\lambda\lambda_1\lambda_2\lambda_3}-V\left(\mathbf{k}-\mathbf{k_2}\right)V\left(\mathbf{k}-\mathbf{k_3}\right)Q_{\lambda\lambda_1\lambda_2\lambda_3}\right] \\
& \times\beta e E_i\left(\omega\right)f_\lambda^{(0)}f_{\lambda_1}^{(0)}f_{-\lambda_2}^{(0)}f_{-\lambda_3}^{(0)} \\
& \left[\chi_i\left(\lambda,k\right)+\chi_i\left(\lambda_1,k_1\right)-\chi_i\left(\lambda_2,k_2\right)-\chi_i\left(\lambda_3,k_3\right)\right].
\end{aligned}
\tag{C.5}
$$

As a result, the linearized Boltzmann equation is

$$
\begin{aligned}
\left(-i\omega\chi_\lambda\left(\beta,\varepsilon_k,\omega\right)-1\right)\left(\mathbf{v}_{\lambda,\mathbf{k}}\right)_i f_\lambda^{(0)}\left(1-f_\lambda^{(0)}\right) = & -\int_{\mathbf{k}_1}\int_{\mathbf{k}_2}\int_{\mathbf{k}_3}(2\pi)^4\,\delta^3\left(\mathbf{k}+\mathbf{k}_1-\mathbf{k}_2-\mathbf{k}_3\right) \\
& \times\delta\left(\varepsilon_\lambda+\varepsilon_{\lambda_1}-\varepsilon_{\lambda_2}-\varepsilon_{\lambda_3}\right)\mathcal{M}^{\mathrm{Col}}_{\lambda\lambda_1\lambda_2\lambda_3}f_\lambda^{(0)}f_{\lambda_1}^{(0)}f_{-\lambda_2}^{(0)}f_{-\lambda_3}^{(0)} \\
& \times\left[\chi_i\left(\lambda,k\right)+\chi_i\left(\lambda_1,k_1\right)-\chi_i\left(\lambda_2,k_2\right)-\chi_i\left(\lambda_3,k_3\right)\right],
\end{aligned}
\tag{C.6}
$$

where

$$
\mathcal{M}^{\mathrm{Col}}_{\lambda\lambda_1\lambda_2\lambda_3}=\left[NV\left(\mathbf{k}-\mathbf{k}_2\right)^2 W_{\lambda\lambda_1\lambda_2\lambda_3}-V\left(\mathbf{k}-\mathbf{k_2}\right)V\left(\mathbf{k}-\mathbf{k_3}\right)Q_{\lambda\lambda_1\lambda_2\lambda_3}\right].
\tag{C.7}
$$

Appendix D

Derivation of time dependent strain in a generic Hamiltonian

The derivation below can be found in Ref. [176], and we include the steps here for completeness. We start from the equation of motion in the $\mathbf{x}$ variables. In the Heisenberg picture, the time dependence of the arbitrary operator A is determined by

$$i\left(\frac{dA}{dt}\right)_x = [A, H_\Lambda]_x + i\left(\frac{\partial A}{\partial t}\right)_x. \tag{D.1}$$

Substitute A by the strain transformation operator $S(t) = \exp\left[-i\xi_{\mu\nu}(t)\,\mathcal{J}_{\mu\nu}\right]$ as

$$i\left(\frac{dS}{dt}\right)_{\mathbf{x}} = [S, H_\Lambda]_{\mathbf{x}} + i\left(\frac{\partial S}{\partial t}\right)_{\mathbf{x}}. \tag{D.2}$$

Hence,

$$i\left(\frac{dS}{dt}\right)_{\mathbf{x}} = SH_\Lambda - H_\Lambda S + i\left(\frac{\partial S}{\partial t}\right)_{\mathbf{x}}, \tag{D.3}$$

or equivalently

$$i\left(\frac{dS}{dt}\right)_{\mathbf{x}} S^{-1} = SH_\Lambda S^{-1} - H_\Lambda + i\left(\frac{\partial S}{\partial t}\right)_{\mathbf{x}} S^{-1}. \tag{D.4}$$

We rewrite the equation above in $\mathbf{X}, \mathbf{P}$ coordinates in the reference frame of the fluid through a canonical transformation implemented by the $S(t)$. $H_\Lambda(t) = H_0^{(\mathbf{X})}$ is viewed as a function of $\mathbf{X}, \mathbf{P}$, which has the same form as H_0. Define $SH_\Lambda S^{-1} = H^{(\mathbf{X})} = H_0^{(\mathbf{X})} + H_1^{(\mathbf{X})}$ as the full Hamiltonian viewed in $\mathbf{X}, \mathbf{P}$.

$$iS^{-1}\left(\frac{dS}{dt}\right)_{\mathbf{X}} = H^{(\mathbf{X})} - H_0^{(\mathbf{X})} + iS^{-1}\left(\frac{\partial S}{\partial t}\right)_{\mathbf{X}} \tag{D.5}$$

The total derivative of S in $\mathbf{X}$ should be zero since it's strain oriented coordinate. By definition, $H^{(\mathbf{X})} = H_0^{(\mathbf{X})} + H_1$. Thus,

$$H_1 = -iS^{-1}\left(\frac{\partial S}{\partial t}\right)_{\mathbf{X}} \tag{D.6}$$

Expand the perturbation H_1 to first order in $\xi_{\mu\nu}$. Since only $\xi_{\mu\nu}$ depends on time,

$$H_1 = -\frac{\partial \xi_{\mu\nu}}{\partial t} \mathcal{J}_{\mu\nu}, \tag{D.7}$$

which corresponds to Eq. (5.87).

Appendix E

Collinear Regime Analysis

E.1 Conductivity

From the functional

$$Q\left[a^{(e)}\right] \equiv \left(\chi_{\lambda,i}, \phi_{\lambda,i}\right) - \frac{1}{2}\left(\chi_{\lambda,i}, C\chi_{\lambda,i} - i\omega a^{(e)}\phi_{\lambda,i}\right), \tag{E.1}$$

and with the subspace of the zero modes, we find the coefficient $a^{(e)}$ of the charge mode. Since the charge mode only carries a electrical current and is orthogonal to the other modes, we may invert $\partial Q/\partial g_{1,\lambda} = 0$ to get the coefficient. The first term is

$$\begin{aligned}
&\partial_g\left(\chi_{\lambda,i}, \phi_{\lambda,i}\right) \\
&= -v_r\beta^3 \sum_{\lambda} \int_{\mathbf{k}} \lambda^2 \chi\left(\omega\right) v_r^2 \frac{1}{\left(e^{\lambda v_r h\beta}+1\right)\left(e^{-\lambda v_r h\beta}+1\right)} \\
&= -\chi\left(\omega\right) v_r^3\beta^3 k_F \int \frac{dq_r}{2\pi}\frac{dq_z}{\pi} \frac{1}{\left(e^{v_r h\beta}+1\right)\left(e^{-v_r h\beta}+1\right)} \\
&= -\chi\left(\omega\right) \frac{v_r^3\beta^3 k_F}{\gamma v_r^2\beta^2} \int \frac{dx}{2\pi}\frac{dy}{\pi} \frac{1}{\left(e^{\sqrt{x^2+y^2}}+1\right)\left(e^{-\sqrt{x^2+y^2}}+1\right)} \\
&= -\chi\left(\omega\right) \frac{\kappa_0}{\gamma}\frac{\ln\left(2\right)}{\pi}.
\end{aligned} \tag{E.2}$$

For the second term, we define dimensionless variables as

$$\begin{aligned}
v_r\beta q_r &\equiv x \\
v_z\beta\gamma q_z &\equiv y \\
v_r k_F\beta &\equiv \kappa_0 \\
x^2+y^2 &\equiv \rho^2
\end{aligned} \tag{E.3}$$

$$\begin{aligned} v_r\beta q_{1r} &\equiv x_1 \\ \gamma v_r\beta q_{1z} &\equiv y_1 \\ v_r\beta k_{1\perp} &\equiv \xi_1 \\ x_1^2+y_1^2 &\equiv \rho_1^2 \end{aligned} \tag{E.4}$$

$$\begin{aligned} v_r\beta\left(q_{2r}-q_r\right) &\equiv x_2 \\ \gamma v_r\beta\left(q_{2z}-q_z\right) &\equiv y_2 \\ v_r\beta k_{2\perp} &\equiv \xi_2 \\ x_2^2+y_2^2 &\equiv \rho_2^2. \end{aligned} \tag{E.5}$$

Then, the second term becomes

$$\begin{aligned} &-\frac{\kappa_0}{4\gamma^3\beta}\left(4\pi\alpha\right)^2\int\frac{dx}{2\pi}\frac{dy}{2\pi}\frac{dx_1dy_1d\xi_1}{\left(2\pi\right)^3}\frac{dx_2dy_2d\xi_2}{\left(2\pi\right)^3}2\pi\ \delta\left(\bar{D}\right)f_\lambda^{(0)}f_{\lambda_1}^{(0)}f_{-\lambda_2}^{(0)}f_{-\lambda_3}^{(0)} \\ &\times\left(\bar{V}_1^2W_{\lambda\lambda_1\lambda_2\lambda_3}-\bar{V}_1\bar{V}_2Q_{\lambda\lambda_1\lambda_2\lambda_3}\right)\chi\left(\omega\right)^2\left[\bar{X}_{\lambda\lambda_1\lambda_2\lambda_3}\right]^2+i\omega\chi\left(\omega\right)^2\frac{\kappa_0}{\gamma}\frac{\ln\left(2\right)}{\pi} \end{aligned} \tag{E.6}$$

where

$$\begin{aligned} \bar{D} = \lambda r &+ \lambda_1\sqrt{\left(x_1+\frac{\xi_1^2}{2\kappa_0}\right)^2+y_1^2}-\lambda_2\sqrt{\left(x+x_2+\frac{\xi_2^2}{2\kappa_0}\right)^2+\left(y+y_2\right)^2} \\ &-\lambda_3\sqrt{\left(x_1-x_2+\frac{\left(\xi_1-\xi_2\right)^2}{2\kappa_0}\right)^2+\left(y_1-y_2\right)} \end{aligned} \tag{E.7}$$

and

$$\bar{V}_1 = \frac{1}{\left(x_2\right)^2+\gamma^{-2}\left(y_2\right)^2+\left(\xi_2\right)^2} \tag{E.8}$$

$$\bar{V}_2 = \left(\frac{1}{\left(x-x_1+x_2\right)^2+\gamma^{-2}\left(y-y+y_2\right)^2+\left(\xi_1-\xi_2\right)^2}\right) \tag{E.9}$$

$$\bar{X}_{\lambda\lambda_1\lambda_2\lambda_3} = \lambda\frac{\mathbf{r}}{r}+\lambda_1\frac{\mathbf{r}_1}{r_1}-\lambda_2\frac{\mathbf{r}-\mathbf{r_2}}{\left|\mathbf{r}-\mathbf{r_2}\right|}-\lambda_3\frac{\mathbf{r_1}+\mathbf{r_2}}{\left|\mathbf{r_1}+\mathbf{r_2}\right|}. \tag{E.10}$$

If we look at the delta function $\delta\left(\bar{D}\right)$, since ξ_1 and ξ_2 are much smaller than κ_0, we can express $\bar{D}$ as

$$\begin{aligned}\bar{D} &\approx \bar{A} + \lambda_1 \frac{x_1 \xi_1^2}{2 r_1 \kappa_0} - \lambda_2 \frac{(x + x_2)\,\xi_2^2}{2\,|\mathbf{r} + \mathbf{r_2}|\,\kappa_0} - \lambda_3 \frac{(x_1 - x_2)\,(\xi_1 - \xi_2)^2}{2\,|\mathbf{r_1} - \mathbf{r_2}|\,\kappa_0} \\ &= -\left(\frac{\lambda_3\,(x_1 - x_2)}{2\,|\mathbf{r_1} - \mathbf{r_2}|\,\kappa_0} + \frac{\lambda_2\,(x + x_2)}{2\,|\mathbf{r} + \mathbf{r_2}|\,\kappa_0}\right)\xi_2^2 + \frac{\lambda_3\,(x_1 - x_2)}{|\mathbf{r_1} - \mathbf{r_2}|\,\kappa_0}\xi_1\xi_2 \\ &\quad - \left(\frac{\lambda_3\,(x_1 - x_2)}{2\,|\mathbf{r_1} - \mathbf{r_2}|\,\kappa_0} - \frac{\lambda_1 x_1}{2 r_1 \kappa_0}\right)\xi_1^2 + \bar{A} \\ &= -\frac{w_1}{2\kappa_0}\left(\xi_1^2 - 2\frac{w_2}{w_1}\xi_2\xi_1 + \frac{w_3}{w_1}\xi_2^2 - \frac{\bar{A}}{w_1}\right) \end{aligned} \tag{E.11}$$

where

$$\bar{A} \equiv \lambda r + \lambda_1 r_1 - \lambda_2\,|\mathbf{r} + \mathbf{r_2}| - \lambda_3\,|\mathbf{r_1} - \mathbf{r_2}| \tag{E.12}$$

$$|\mathbf{r} + \mathbf{r_2}| \equiv \sqrt{(x + x_2)^2 + (y + y_2)^2} \tag{E.13}$$

$$|\mathbf{r_1} - \mathbf{r_2}| \equiv \sqrt{(x_1 - x_2)^2 + (y_1 - y_2)^2} \tag{E.14}$$

$\bar{D}$ is a quadratic function of ξ_1. Then, we can express the delta function as

$$\delta\left(\bar{D}\,(\xi_1)\right) = \sum_i \frac{\delta\,(\xi_1 - \xi_i)}{\left|\bar{D}'\,(\xi_i)\right|} \tag{E.15}$$

where $\bar{D}'$ is the first derivative of ξ_1 and $\xi_{i=\pm}$ are the two roots of the quadratic function

$$\bar{D} = \frac{w_1}{2\kappa_0}\,(\xi_1 - \xi_+)\,(\xi_1 - \xi_-) \tag{E.16}$$

By a quadratic formula,

$$\xi_\pm = \frac{w_2}{w_1}\xi_2 \pm \sqrt{\left(\frac{w_2}{w_1}\xi_2\right)^2 - \left(\frac{w_3}{w_1}\xi_2^2 - \frac{\bar{A}}{w_1}\right)} \tag{E.17}$$

Thus,

$$\delta\left(\bar{D}\,(\xi_2)\right) = 2\kappa_0 \left|\frac{1}{\sqrt{(w_1 w_2 \xi_2)^2 - \left(w_1 w_3 \xi_2^2 - w_1 \bar{A}\right)}}\right| \left(\delta\,(\xi_1 - \xi_{1+}) + \delta\,(\xi_1 - \xi_{1-})\right) \tag{E.18}$$

When we set $\bar{A} \to 0$, the logarithmic divergence as $\xi_2 \to 0$ is clear. Thus, there are two important regions of the integrand in phase space: $\bar{A} \to 0$ and $\xi_2 \to 0$. As the other problems in other Dirac system, we expect this divergence is cutoff by higher-order self-energy corrections to the fermions, which are of the order of $\alpha\Lambda$, with Λ is set by the ultraviolet cutoff of hydrodynamic regime. Hence,

the range of the integration is from $\alpha\Lambda$ to Λ. So we may approximate

$$\int d\xi_2 \left| \frac{1}{\sqrt{\left(w_1 w_2 \xi_2\right)^2 - \left(w_1 w_3 \xi_2^2 - w_1 \bar{A}\right)}} \right| \approx \frac{\ln\left(1/\alpha\right)}{\sqrt{\left(w_1 w_2\right)^2 - w_1 w_2}}, \tag{E.19}$$

and set $\xi_1 = \xi_2 = 0$ elsewhere to obtain the leading contribution to the collision integral in the limit $\alpha \to 0$. One can notice the integration is independent from the value of $\bar{A}$ in the leading order. We can now find

$$C_{22} = -\frac{\kappa_0^2 \alpha^2}{\gamma^3 \beta} \chi\left(\omega\right)^2 c_{22}\left(\gamma\right) + i\omega\chi\left(\omega\right)^2 \frac{\kappa_0}{\gamma} \frac{\ln\left(2\right)}{\pi}, \tag{E.20}$$

where

$$\begin{aligned} c_{22} = \frac{1}{2}\left(4\pi\alpha\right)^2 \int \frac{dxdy}{\left(2\pi\right)^2} \frac{dx_1 dy_1}{\left(2\pi\right)^2} \frac{dx_2 dy_2 d\xi_2}{\left(2\pi\right)^3} \frac{1}{\left|\xi_2\right| \sqrt{\left(w_1 w_2\right)^2 - w_1 w_2}} f_{\lambda}^{(0)} f_{\lambda_1}^{(0)} f_{-\lambda_2}^{(0)} f_{-\lambda_3}^{(0)} \\ \times \left(\bar{V}_1^2 W_{\lambda\lambda_1\lambda_2\lambda_3} - \bar{V}_1 \bar{V}_2 Q_{\lambda\lambda_1\lambda_2\lambda_3}\right)_{\xi_1=\xi_2=0} \left[\bar{X}_{\lambda\lambda_1\lambda_2\lambda_3}\right]^2_{\xi_1=\xi_2=0}. \end{aligned} \tag{E.21}$$

E.2 Shear Viscosity

For shear viscosity, there are two subspace of zero modes which are relevant. We get two equations $\partial Q/\partial\chi_1 = 0$, $\partial Q/\partial\chi_2 = 0$ can represent them as a matrix form. The two left-hand side components are

$$\begin{aligned} b^1 &= v_r^3 \beta^3 \sum_{\lambda} \int_{\mathbf{k}} \lambda^2 I'_{ij} I_{ij} \frac{\beta\varepsilon_{\mathbf{k}}}{\left(e^{\lambda v_r h\beta} + 1\right)\left(e^{-\lambda v_r h\beta} + 1\right)} \\ &= \frac{\kappa_0}{\gamma} \int \frac{dx}{2\pi} \frac{dy}{\pi} \frac{\left[\frac{2}{3}x^2 + \left(1 - \frac{2}{3}\gamma^{-2} + \frac{1}{3}\gamma^2\right) y^2\right]}{\sqrt{x^2+y^2}\left(e^{\sqrt{x^2+y^2}} + 1\right)\left(e^{-\sqrt{x^2+y^2}} + 1\right)} \\ &= \frac{\kappa_0}{\gamma}\left(\frac{5 - 2\gamma^{-2} + \gamma^2}{3}\right)\frac{\pi}{12} \end{aligned} \tag{E.22}$$

$$\begin{aligned} b^2 &= v_r^3 \beta^3 \sum_{\lambda} \int_{\mathbf{k}} \lambda^2 I'_{ij} I_{ij} \frac{\left(v_r \beta \left|\mathbf{h}\right|\right)^2}{\left(e^{\lambda v_r h\beta} + 1\right)\left(e^{-\lambda v_r h\beta} + 1\right)} \\ &= \frac{\kappa_0}{\gamma} \int \frac{dx}{2\pi} \frac{dy}{\pi} \frac{\left[\frac{2}{3}x^2 + \left(1 - \frac{2}{3}\gamma^{-2} + \frac{1}{3}\gamma^2\right) y^2\right]}{\left(e^{\sqrt{x^2+y^2}} + 1\right)\left(e^{-\sqrt{x^2+y^2}} + 1\right)} \\ &= \frac{\kappa_0}{\gamma}\left(\frac{5 - 2\gamma^{-2} + \gamma^2}{3}\right)\frac{9}{4\pi}\zeta\left[3\right] \end{aligned} \tag{E.23}$$

since $\int_0^{2\pi}\cos^2\theta d\theta = \int_0^{2\pi}\sin^2\theta d\theta = \pi$, where we used the same change of variables with the calculation in the conductivity. Two right hand side in a matrix form is

$$\frac{\kappa_0^2\alpha^2}{\gamma^3}\begin{pmatrix} c_{11}^{\eta}(\gamma) & c_{12}^{\eta}(\gamma) \\ c_{21}^{\eta}(\gamma) & c_{22}^{\eta}(\gamma) \end{pmatrix}\begin{pmatrix} a_1 \\ a_2 \end{pmatrix} \tag{E.24}$$

where $c_{\mu\nu}^{\eta}(\gamma)$ corresponds to the eq (E.21) with

$$\begin{aligned} \bar{X}^2_{\lambda\lambda_1\lambda_2\lambda_3} &\to \bar{X}_{ij}^{(\mu)}\bar{X}_{ij}^{(\nu)} \\ &= \left(\chi_{ij}^{\mu}(\mathbf{r}) + \chi_{ij}^{\mu}(\mathbf{r_1}) - \chi_{ij}^{\mu}(\mathbf{r}+\mathbf{r_2}) - \chi_{ij}^{\mu}(\mathbf{r_1}-\mathbf{r_2})\right) \\ &\quad\times\left(\chi_{ij}^{\nu}(\mathbf{r}) + \chi_{ij}^{\nu}(\mathbf{r_1}) - \chi_{ij}^{\nu}(\mathbf{r}+\mathbf{r_2}) - \chi_{ij}^{\nu}(\mathbf{r_1}-\mathbf{r_2})\right) \end{aligned} \tag{E.25}$$

As a result, we get

$$\frac{\kappa_0}{\gamma}\left(\frac{5-2\gamma^{-2}+\gamma^2}{3}\right)\begin{pmatrix} \frac{\pi}{12} \\ \frac{9}{8\pi}\zeta[3] \end{pmatrix} = \frac{\kappa_0^2\alpha^2}{\gamma^3}\begin{pmatrix} c_{22}^{\eta}(\gamma) & c_{23}^{\eta}(\gamma) \\ c_{32}^{\eta}(\gamma) & c_{33}^{\eta}(\gamma) \end{pmatrix}\begin{pmatrix} a_1 \\ a_2 \end{pmatrix} \tag{E.26}$$

and may invert to get the coefficients.

Bibliography

[1] S. Tomonaga, Prog. Theor. Phys. **5**, 544 (1950)

[2] J. M. Luttinger , J. Math. Phys. **4**, 1154 (1963)

[3] D. C. Mattis and E. H. Lieb, J. Math. Phys. **6**, 304 (1965)

[4] I. E. Dzyaloshinskii and A. Larkin, Sov. Phys. JETP **38**, 202 (1974)

[5] F. D. M. Haldane, Phys. Rev. Lett. **47**, 1840 (1981)

[6] L. D. Landau, Sov. Phys. JETP **3**(6), 920 (1957)

[7] A. A. Abrikosov and S. D. Beneslavskii, J. Low. Temp. Phys. **5**(2), 141-154 (1971)

[8] A. H. Castro Neto, F. Guinea, N. M. R. Peres, K. S. Novoselov, and A. K. Geim, Rev. Mod. Phys., vol. **81**, 109-162 (2009)

[9] A. Lucas and K. C. Fong, J. Phys.: Condens. Matter **30**, 053001 (44pp) (2018)

[10] E. V. Gorbar, V. A. Miransky, I. A. Shovkovy, and P. O. Sukhachov, Phys. Rev. B **98**, 035121 (2018)

[11] M. V. Berry, Proc. R. Soc. Lond. A392, 45–57 (1984)

[12] Daniel Rohrlich, *Berry phase*, Compendium of Quantum Physics, Pages 31-36 (2009)

[13] Cayssol, Jérôme, Comptes rendus - Physique, Vol.**14**(9-10), pp.760-778 (2013)

[14] F. D. M. Haldane, Phys. Rev. Lett. **61**, 2015 (1988)

[15] S. Raghu, X.-L. Qi, C. Honerkamp, and S.-C. Zhang, Phys. Rev. Lett. **100**, 156401 (2008)

[16] C.L. Kane, E.J. Mele, Phys. Rev. Lett. **95**, 226801 (2005)

[17] C.L. Kane, E.J. Mele, Phys. Rev. Lett. **95**, 146802 (2005)

[18] M.Z. Hasan and C.L. Kane, Rev. Mod. Phys. **82** p.3045 (2010)

[19] X.-L. Qi and S.-C. Zhang, Rev. Mod. Phys **83** p.1057 (2011)

[20] N. Armitage, E. Mele and A. Vishwanath, preprint arXiv:1705.01111 (2017)

[21] Z. Wang, Y. Sun, X.-Q. Chen, C. Franchini, G. Xu, H. Weng, X. Dai and Z. Fang, Phys. Rev. B **85** p.195320 (2012)

[22] Z. Liu, B. Zhou, Y. Zhang, Z. Wang, H. Weng, D. Prabhakaran, S.-K. Mo, Z. Shen, Z. Fang, X. Dai, et al., Science **343** p.864 (2014)

[23] M. Neupane, S. Xu, R. Sankar, N. Alidoust, G. Bian, C. Liu, I. Belopolski, T. Chang, H. Jeng, H. Lin, et al., Nat. Commun. 5 p.3786 (2014)

[24] Z. Liu, J. Jiang, B. Zhou, Z. Wang, Y. Zhang, H. Weng, D. Prabhakaran, S. Mo, H. Peng, P. Dudin, et al., Nat. Mater. **13** p.677 (2014)

[25] S. Borisenko, Q. Gibson, D. Evtushinsky and V. Zabolotnyy, B. B ü chner, and R: J. Cava Phys. Rev. Lett. **113** p.027603 (2014)

[26] W. Hermann, Zeitschrift für Physik **56**.5-6: 330-352 (1929)

[27] H.B. Nielsen and M. Ninomiya, Nucl. Phys. B **185** p.20 (1981)

[28] H.B. Nielsen and M. Ninomiya, Nucl. Phys. B **193** p.173 (1981)

[29] Z. Fang, N. Nagaosa, K.S. Takahashi, A. Asamitsu, R. Mathieu, T. Ogasawara, H.Yamada, M. Kawasaki, Y. Tokura, and K. Terakura Science. **302**, p. 92 (2003)

[30] X. Wan, A.M. Turner, A. Vishwanath and S.Y. Savrasov, Phys. Rev. B **83** p.205101 (2011)

[31] L. Balents, Physics **4** p.36 (2011)

[32] G. Xu, H. Weng, Z. Wang, X. Dai and Z. Fang, Phys. Rev. Lett. **107** p.186806 (2011)

[33] P. B. Pal, arXiv:physcis/0703214 (2015)

[34] S.M. Huang et al., Nat. Commun. **6**:7373 (2015)

[35] S. Y. Xu, I. Belopolski, N. Alidoust and M.Z. Neupane, Science **349** p.613. (2015)

[36] B. Q. Lv, H. M. Weng, B. B. Fu, X. P. Wang, H. Miao, J. Ma, P. Richard, X. C. Huang, L. X. Zhao, G. F. Chen, Z. Fang, X. Dai, T. Qian, and H. Ding, Phys. Rev. X **5**, 031013 (2015)

[37] S.-Y. Xu, N. Alidoust, I. Belopolski, Z. Yuan, G. Bian, T.-R. Chang, H. Zheng, V.N. Strocov, D.S. Sanchez, G. Chang and C. Zhang, Nat. Phys. **11**, p. 748 (2015)

[38] S. Souma, Z. Wang, H. Kotaka, T. Sato, K. Nakayama, Y. Tanaka, H. Kimizuka, T. Takahashi, K. Yamauchi, T. Oguchi and K. Segawa, Phys. Rev. B **93** p.161112 (2016).

[39] Z. Liu, L. Yang, Y. Sun, T. Zhang, H. Peng, H. Yang, C. Chen, Y. Zhang, Y. Guo, D. Prabhakaran and M. Schmidt, Nat. Mater. **15** p.27 (2016).

[40] L. Lu, Z. Wang, D. Ye, L. Ran, L. Fu and J.D. Joannopoulos, and M. Soljačić, Science **349** p.622 (2015)

[41] K. Deng, et al, Nat. Phys. **12** p.1105 (2016)

[42] Huang L, McCormick TM, Ochi M, Zhao Z, Suzuki M-T, et al, Nat. Mater. **15**:1155–60 (2016)

[43] A. Liang, et al, arXiv preprint arXiv:1604.01706 (2016)

[44] J. Jiang, et al, arXiv preprint arXiv:1604.00139 (2016)

[45] Y. Wu, et al, Phys. Rev. B **94** p.121113 (2016)

[46] I. Belopolski, et al, arXiv preprint arXiv:1512.09099 (2015)

[47] I. Belopolski, et al, Phys. Rev. B **94**, 085127 (2016)

[48] I. Belopolski, et al, Nat. Commun. **7** 13643 (2016)

[49] H. Weng, Y. Liang, Q. Xu, R. Yu, Z. Fang, X. Dai and Y. Kawazoe, Phys. Rev. B **92** p.045108 (2015)

[50] A. Burkov, M. Hook and L. Balents, Phys. Rev. B **84**.235126 (2011)

[51] T.T. Heikkilä and G.E. Volovik, JETP Lett. **93**.59 (2011)

[52] N. Kopnin,T. Heikkil ä and G. Volovik, Phys. Rev. B **83**.220503 (2011)

[53] T.T. Heikkilä, N.B. Kopnin, and G.E. Volovik, JETP Lett. **94**.233 (2011)

[54] Y. Kim, B.J. Wieder, C. Kane and A.M. Rappe, Phys. Rev. Lett. **115**.036806 (2015)

[55] Q. Gibson, L. Schoop, L. Muechler, L. Xie, M. Hirschberger, N. Ong, R. Car and R. Cava, Phys. Rev. B **91**, 205128 (2015)

[56] S.-Y. Yang, H. Yang, E. Derunova, S. S. P. Parkin,B. Yan, and M. N. AliMax, Adv. Phys. X **3:1**, 1414631 (2018)

[57] R. Hoffmann, Angew. Chem. Int. Ed. English. **26**.846 (1987)

[58] S.M. Young and C.L. Kane, Phys. Rev. Lett. **115**.126803 (2015)

[59] Y. Du, F. Tang, D. Wang, L. Sheng, E.-J. Kan, C.-G. Duan, S.Y. Savrasov and X. Wan, npj Quant. Mater. **2**.3 (2017)

[60] M. Zeng, C. Fang, G. Chang, Y.-A. Chen, T. Hsieh, A. Bansil, H. Lin and L. Fu, preprint arXiv:1504.03492 (2015)

[61] J. Nayak, S.-C. Wu, N. Kumar, C. Shekhar, S. Singh, J. Fink, E.E. Rienks, G.H. Fecher, S.S. Parkin, B. Yan, et al. Nat. Commun. **8** (2017)

[62] F.F. Tafti, Q. Gibson, S. Kushwaha, J.W. Krizan, N. Haldolaarachchige and R.J. Cava, Proc. Nat. Acad. Sci. **113**.E3475 (2016)

[63] F. Tafti, Q. Gibson, S. Kushwaha, N. Haldolaarachchige and R. Cava, Nat. Phys. **12**.272 (2016)

[64] N. Kumar, C. Shekhar, S.-C. Wu, I. Leermakers, O. Young, U. Zeitler, B. Yan and C. Felser, Phys. Rev. B. **93**.241106 (2016)

[65] L.-K. Zeng, R. Lou, D.-S. Wu, Q. Xu, P.-J. Guo, L.-Y. Kong, Y.-G. Zhong, J.-Z. Ma, B.-B. Fu, P. Richard and P. Wang, Phys. Rev. Lett. **117**.127204 (2016)

[66] Y.-H. Chan, C.-K. Chiu, M. Chou and A.P. Schnyder, Phys. Rev. B **93**.205132 (2016)

[67] L.S. Xie, L.M. Schoop, E.M. Seibel, Q.D. Gibson, W. Xie and R.J. Cava, APL Mater. **3**.083602 (2015)

[68] Q. Xu, R. Yu, Z. Fang, X. Dai and H. Weng, Phys. Rev. B **95** p.045136 (2017)

[69] H. Huang, J. Liu, D. Vanderbilt and W. Duan, Phys. Rev. B **93**.201114 (2016)

[70] X. Feng,, C. Yue, Z. Song, Q. Wu and B. Wen, preprint arXiv:1705.00511 (2017)

[71] B. Feng, B. Fu, S. Kasamatsu, S. Ito, P. Cheng, C.-C. Liu, S.K. Mahatha, P. Sheverdyaeva, P. Moras, M. Arita and O. Sugino, preprint arXiv:1611.09578 (2016)

[72] J. Lu, W. Luo, X. Li, S. Yang, J. Cao, X. Gong and H. Xiang, preprint arXiv:1603.04596 (2016)

[73] L. S. Xie , L. M. Schoop , E. M. Seibel , Q. D. Gibson, W. Xie, and R. J. Cava, APL Mater. **3**, 083602 (2015)

[74] M.N. Ali, Q.D. Gibson, T. Klimczuk and R. Cava, Phys. Rev. B **89**.020505 (2014)

[75] S.-Y. Guan, P.-J. Chen, M.-W. Chu, R. Sankar, F. Chou, H.-T. Jeng, C.-S. Chang and T.-M. Chaung Sci. Adv. 2.e1600894 (2016)

[76] H. Inoue, A. Gyenis, Z. Wang, J. Li, S.W. Oh, S. Jiang, N. Ni, B.A. Bernevig and A. Yazdani, Science **351**.1184 (2016).

[77] R. Batabyal, N. Morali, N. Avraham, Y. Sun, M. Schmidt, C. Felser, A. Stern, B. Yan and H. Beidenkopf, Sci. Adv. 2. e1600709 (2016)

[78] R. Yu, Q. Wu, Z. Fang and H. Weng, Phys. Rev. Lett. **119**.036401 (2017)

[79] A. Yamakage, Y. Yamakawa, Y. Tanaka and Y. Okamoto, J. Phys. Soc. Jpn **85**.013708 (2015)

[80] Y. Sun, Y. Zhang, C. Felser, and B. Yan, Phys. Rev. Lett. **117**, 146403 (2016)

[81] R. Lou, J.-Z. Ma, Q.-N. Xu, B.-B. Fu, L.-Y. Kong, Y.-G. Shi, P. Richard, H.-M. Weng, Z. Fang, S.-S. Sun and Q. Wang, Phys. Rev. B **93**.241104 (2016)

[82] J. Hu, Z. Tang, J. Liu, X. Liu, Y. Zhu, D. Graf, K. Myhro, S. Tran, C.N. Lau, J. Wei and Z. Mao, Phys. Rev. Lett. **117**.016602 (2016)

[83] Q. Xu, Z. Song, S. Nie, H. Weng, Z. Fang and X. Dai, Phys. Rev. B. **92**.205310 (2015)

[84] B. Yan and C. Felser, Ann. Rev. of Con. Mat. Phys. Vol. **8**:337-354 (2017)

[85] C. Chen, *et al.*, Phys. Rev. B **95**, 125126 (2017)

[86] G. B. Hala´sz and L. Balents, Phys. Rev. B **85**, 035103 (2012)

[87] A. A. Burkov and L. Balents, Phys. Rev. Lett. **107**, 127205 (2011)

[88] S. M. Young, S. Zaheer, J. C. Y. Teo, C. L. Kane, E. J. Mele, and A. M. Rappe Phys. Rev. Lett. **108**, 140405 (2012)

[89] Z. Wang, Y. Sun, X.-Q. Chen, C. Franchini, G. Xu, H. Weng, X. Dai, and Z. Fang Phys. Rev. B **85**, 195320 (2012)

[90] Z. Wang, H. Weng, Q. Wu, X. Dai, and Z. Fang Phys. Rev. B **88**, 125427 (2012)

[91] D. J. Thouless, M. Kohmoto, M. P. Nightingale, and M. Den Nijs, Phys. Rev. Lett. **49**, 405 (1982)

[92] L.-K. Lim and R. Moessner, Phys. Rev. Lett. **118**, 016401 (2017)

[93] A. A. Burkov, M. D. Hook and L. Balents, Phys. Rev. B **84**, 235126 (2011)

[94] S. A. Yang, H. Pan, and F. Zhang, Phys. Rev. Lett. **113**, 046401 (2014)

[95] M. Ezawa, Phys. Rev. Lett. **116**, 127202 (2016)

[96] J.-T. Wang, H. Weng, S. Nie, Z. Fang, Y. Kawazoe, and C. Chen, Phys. Rev. Lett. **116**, 195501 (2016)

[97] G. Bian *et.al.*, Nat. Commun. **7**, 10556 (2016)

[98] G. Bian *et al.*, Phys. Rev. B **93**, 121113(R) (2016)

[99] R. Li, H. Ma, X. Cheng, S. Wang, D. Li, Z. Zhang, Y. Li, and X.-Q. Chen, Phys. Rev. Lett. **117**, 096401 (2016)

[100] X.-L. Qi, Y.-S. Wu, and S.-C. Zhang Phys. Rev. B **74**, 085308 (2006)

[101] A. Burkov, Phys. Rev. Lett. **113**, 187202 (2014)

[102] G. Xu, J. Wang, C. Felser, X.-L. Q, and S.-C. Zhang, Nano Lett. **15**, 2019 (2015)

[103] H. Weng, R. Yu, X. Hu, X. Dai, and Z. Fang, Adv. Phys. **64**, 227 (2015)

[104] R. Okugawa and S. Murakami, Phys. Rev. B **96**, 115201 (2017)

[105] S. W. Kim, K. Seo, B. Uchoa, Phys. Rev. B **97**, 201101(R) (2018)

[106] S. W. Kim and B. Uchoa, Phys. Rev. B **99**, 201301(R) (2019)

[107] A. G. Grushin, E. V. Castro, A. Cortijo, F. de Juan, M. A. H. Vozmediano, B. Valenzuela, Phys. Rev. B **87**, 085136 (2013)

[108] J. Motruk, A. G. Grushin, F. de Juan, and F. Pollmann Phys. Rev. B **92**, 085147 (2015)

[109] D.D. Scherer, M.M. Scherer, C. Honerkamp, Phys. Rev. B **92**, 155137 (2015)

[110] B. I. Halperin, Jpn. J. of Appl. Phys. **26**, 1913 (1987)

[111] R. D. Cowley, Adv. Phys. **29**, 1 (1980)

[112] F. Guinea, M. I. Katsnelson, and A. K. Geim, Nat. Phys. **6**, 30 (2010)

[113] N. Levy, S. A. Burke, K. L. Meaker, M. Panlasigui, A. Zettl, F. Guinea, A. H. Castro Neto, M. F. Crommie, Science **329**, 544 (2010)

[114] A. H. Castro Neto, N. M. R. Peres, F. Guinea, A. Geim, K. Novoselov, Rev. Mod. Phys. **81**, 109 (2009)

[115] M. C. Rechtsman, J. M. Zeuner, A. Tu¨nnermann, S. Nolte, M. Segev and A. Szameit, Nat. Photonics **7**, 153 (2013)

[116] L. Balicas, G. Kriza, and F. I. B. Williams, Phys. Rev. Lett. **75**, 2000 (1995)

[117] S. M. McKernan, S. T. Hannahs, U. M. Scheven, G. M. Danner, and P. M. Chaikin, Phys. Rev. Lett. **75**, 1630 (1995)

[118] B. A. Bernevig, T. L. Hughes, S. Raghu, and D. P. Arovas, Phys. Rev. Lett. **99**, 146804 (2007)

[119] D. Arovas and F. Guinea, Phys. Rev. B **78**, 245416 (2008)

[120] K. Mullen, B. Uchoa, and D. T. Glatzhofer, Phys. Rev. Lett. **115**, 026403 (2015)

[121] L.-K. Lim and R. Moessner, Phys. Rev. Lett. **118**, 016401 (2017)

[122] J.-W. Rhim and Y. B. Kim, Phys. Rev. B **92**, 045126 (2015)

[123] R. Yu, H. Weng, Z. Fang, X. Dai, and X. Hu, Phys. Rev. Lett. **115**, 036807 (2015)

[124] T. T. Heikkila and G. E. Volovik, JETP Lett. **93**, 59 (2011)

[125] Y. Chen, Y. Xie, S. A. Yang, H. Pan, F. Zhang, M. L. Cohen, and S. Zhang, Nano Lett. **15**, 6974 (2015)

[126] L. S. Xie, L. M. Schoop, E. M. Seibel, Q. D. Gibson, W. Xie, and R. J. Cava, APL Mater. **3**, 083602 (2015)

[127] K. K. Gomes, W. Mar, Wonhee Ko, F. Guinea, and H. C. Manoharan, Nature **483**, 306 (2012)

[128] Y. Zhu, Y. Peng, X. Fan, J. Yang, B. Liang, X. Zhu, and J. Cheng, arXiv:1801.07942 (2018)

[129] Frame effects can be accounted in higher order corrections in the derivative expansion. Those terms give geometrical corrections to the Hamiltonian, but do not affect the elastic gauge fields. See F. de Juan, J. L. Mañes, and M. A. H. Vozmediano, Phys. Rev. B **87**, 165131 (2013)

[130] M. Barkeshli, S. Bum Chung, and X.-L. Qi, Phys. Rev. B **85**, 245107 (2012)

[131] H. Shapourian, T. L. Hughes, and S. Ryu, Phys. Rev. B **92**, 165131 (2015)

[132] N. Read and E. Rezayi, Phys. Rev. B **84**, 085316 (2011)

[133] J. E. Avron, R. Seiler, and P. G. Zograf, Phys. Rev. Lett. **75**, 697 (1995)

[134] J. E. Avron, J. Stat. Phys. **92**, 543 (1998)

[135] T. Scaffidi, N. Nandi, B. Schmidt, A. P. Mackenzie, and J. E. Moore, Phys. Rev. Lett. **118**, 226601 (2017)

[136] L. V. Delacretaz and A. Gromov, Phys. Rev. Lett. **119**, 226602 (2017)

[137] F. M. D. Pellegrino, I. Torre, and M. Polini, Phys. Rev. B **96**, 195401 (2017)

[138] T. L. Hughes, R. G. Leigh, and E. Fradkin, Phys. Rev. Lett. **107**, 075502 (2011)

[139] A. Cortijo, Y. Ferreirós, K. Landsteiner, and M. A. H. Vozmediano, Phys. Rev. Lett. **115**, 177202 (2015)

[140] H. Watanabe, Y. Hatsugai, and H. Aoki, Phys. Rev. B **82**, 241403(R) (2010)

[141] A. Martín-Ruiz and A. Cortijo, Phys. Rev. B **98**, 155125 (2018)

[142] K. A. Modic et al., Nat. Commun. **5**, 4203 (2014)

[143] G. Jotzu, M. Messer, R. Desbuquois, M. Lebrat, T. Uehlinger, D. Greif, and T. Esslinger, Nature (London) **515**, 237 (2014)

[144] L. Lu, L. Fu, J. D. Joannopoulos, and M. Soljačić, Nat. Photonics **7**, 294 (2013)

[145] A. Ramires and J. L. Lado Phys. Rev. Lett. **121**, 146801 (2018)

[146] B. N. Narozhny, I. V. Gornyi, A. D. Mirlin, J. Schmalian, Ann. Phys. (Berlin) Vol.**529**(11), 1700043 (2017)

[147] A. I. Berdyugin, S. G. Xu, F. M. D. Pellegrino, R. Krishna Kumar, A. Principi, I. Torre, M. Ben Shalom, T. Taniguchi, K. Watanabe, I. V. Grigorieva, M. Polini, A. K. Geim, D. A. Bandurin, arXiv:1806.01606 (2018)

[148] C. Hoyos, and D. T. Son, Phys. Rev. Lett. **108**, 066805 (2012)

[149] F. D. M. Haldane, arXiv:0906.1854 (2009)

[150] P. Roushan et al., Nature (London) **515**, 241 (2014)

[151] P. Arnold, *et al,* JHEP 11 Vol. **2000**, 001 (2000)

[152] R. N. Gurzhi, J .Exptl. Theoret. Phys. (U.S.S.R.) **44**, 771-772 (February, 1963)

[153] M. J. M. de Jong and L. W. Molenkamp, Phys. Rev. B **51**, 13389 (1995)

[154] S. Hartnoll, A. Lucas and S. Sachdev, *Holographic quantum matter,* MIT Press (2016)

[155] J. Maldacena, Adv. Theo. Math. Phys. **2**, 231 (1998)

[156] E. Shuryak, Prog. Part. Nucl. Phys. **53**, 273 (2004)

[157] M. Muller, J. Schmalian, and L. Fritz, Phys. Rev. Lett. **103**, 025301 (2009)

[158] D. A. Bandurin *et al.*, Science **351**, 1055 (2016)

[159] J. Crossno *et al.*, Science, **351**, 1058 (2016)

[160] P. K. Kovtun, D. T. Son, and A. O. Starinets, Phys. Rev. Lett. **94**, 111601 (2005)

[161] M. Shavit, A. Shytov, and Gregory Falkovich, Phys. Rev. Lett. **123**, 026801 (2019)

[162] A.A. Patel and S. Sachdev, Phys. Rev. Lett. **123**, 066601 (2019)

[163] J. Zaanen, SciPost Phys. **6**, 061 (2019)

[164] P. Adroguer, D. Carpentier, G. Montambaux, and E. Orignac, Phys. Rev. B **93**, 125113 (2016)

[165] J. Link, Boris N. Narozhny, Egor I. Kiselev, and Jörg Schmalian, Phys. Rev. Lett. **120**, 196801 (2018)

[166] Y. Huh,1 E.-G. Moon, and Y. B. Kim, Phys. Rev. B **93**, 035138 (2016)

[167] L. P. Kadanoff, G. Baym, and D. Pines, *Quantum statistical mechanics*, Originally published in 1962

[168] L. Fritz, J. Schmalian, M. Müller, and S. Sachdev, Phys. Rev. B **78**, 085416 (2008)

[169] A. B. Kashuba, Phys. Rev. B **78**, 085415 (2008)

[170] S. Sachdev, Phys. Rev. B **57**, 7157 (1998)

[171] S. Sachdev, *Quantum Phase Transitions* (Cambridge University Press, Cambridge, 1999), p. 185

[172] P. R. Wallace, Phys. Rev. **71**, 622 (1947)

[173] G. D. Mahan, Condensed Matter in a Nutshell (Princeton University Press, 2010), p.325

[174] H. Guo, E. Ilseven, G. Falkovich, and L. S. Levitov, Proceedings of the National Academy of Sciences of the United States of America Vol. **114**, No. 12, pp. 3068-3073 (2017)

[175] L. D. Landau and E. M. Lifshitz, *Fluid Mechanics* - 2nd Edition (Pergamon Press, 1987)

[176] B. Bradlyn, M. Goldstein, and N. Read, Phys. Rev. B **86**, 245309 (2012)

[177] J. M. Maldacena, Adv. Theor. Math. Phys. **2**, 231 (1998)

[178] S. S. Gubser, I. R. Klebanov, and A. M. Polyakov, Phys. Lett. B **428**, 105 (1998)

[179] E. Witten, Adv. Theor. Math. Phys. **2**, 253 (1998)

[180] O. Aharony, S. S. Gubser, J. M. Maldacena, H. Ooguri, and Y. Oz, Phys. Rep. **323**, 183 (2000)

[181] P. K. Kovtun, D. T. Son, and A. O. Starinets, Phys. Rev. Lett. **94**, 111601 (2005)

[182] D. T. Son and A. O. Starinets, Annual Review of Nuclear and Particle Science Vol. **57**:95-118 (2007)

[183] M. Brigante, H. Liu, R. C. Myers, S. Shenker, and S. Yaida, Phys. Rev. D **77**, 126006 (2008)

[184] M. Brigante, H. Liu, R. C. Myers, S. Shenker, and S. Yaida, Phys. Rev. Lett. **100**, 191601 (2008)

[185] Y. Kats and P. Petrov, Journal of High Energy Physics, vol. **2009**, no. 01, p. 044 (2009)

[186] J. M. Link, B. N. Narozhny, E. I. Kiselev, and J. Schmalian, Phys. Rev. Lett. **120**, 196801 (2018)

[187] M. Müller, J. Schmalian, and L. Fritz, Phys. Rev. Lett. **103**, 025301 (2009)

[188] D. E. Sheehy and J. Schmalian, Phys. Rev. Lett. **99**, 226803 (2007)

[189] H. Weng, X. Dai, and Z. Fang, J. Phys.: Condens. Matter **28** 303001 (2016)